

**ELECTROLYSIS OF CRYOLITE-ALUMINA MELTS
AND SUSPENSIONS WITH OXYGEN EVOLVING
ELECTRODES**

Sai Krishna Padamata



Siberian Federal University

Krasnoyarsk, Russia 2020

Abstract

The development of inert anodes for aluminium reduction cell has been a challenging issue for industries. The inert anodes use can be environmentally friendly, energy-efficient and economic. It has been previously discussed by the researchers that the inert anodes can only be fully efficient when used in vertical electrode cell along with a wettable cathode in low-temperature melts. Currently, Cu-based alloys have been considered as promising candidates (along with the Fe-Ni alloys) as the inert anodes material in aluminium reduction cells with low-temperature electrolytes. When it comes to the wettable cathode, TiB₂ is widely considered as promising materials although other materials such as carbon, tungsten, graphite are tested to analyse the cathode behaviour of the material in various conditions. The low-temperature alumina suspension electrolytes are considered to reduce the impurities in aluminium produced, so it is important to examine the behaviour of alumina in the melts. Metallic anodes tend to contaminate the produced aluminium with their corrosion products and introducing alumina suspension particles in the electrolyte could resolve this problem by suppressing the convective transfer of corrosion products. In this thesis, the anode behaviour of Cu-Al based electrodes, cathode behaviour of tungsten electrode in low-temperature KF-AlF₃ melts are tested. Along with that, the alumina dissolution and sedimentation rate in KF-AlF₃ melts at different conditions are tested.

In the first stage, the tests were conducted to characterize the electrochemical behaviour of CuAl-based anodes (Cu-9Al-5Fe (A1), Cu-10Al (A2), and Cu-10Al-1.7Be (A3)) in KF-AlF₃-Al₂O₃ melts ($CR \left(\frac{\text{Mole \% KF}}{\text{Mole \% AlF}_3} \right) = 1.3$) and suspensions have been made and presented. The effects of the suspension (or melt) properties, the anode composition and the temperature on the electrochemical behaviour of the anode and the kinetics of the oxide layer formation during polarization are studied. Increase in volume fraction led to an appreciable decrease in apparent limiting current density of the oxygen evolution and the metal oxidation. The results obtained suggested the further study shall be conducted on A2 anode. In the second stage, anodic processes on A2 electrode in molten KF-AlF₃-Al₂O₃ (5 wt. %) and suspensions were characterized. Effects of cryolite ratio CR (1.2-1.5), temperature and particle volume fraction ($\phi = 0 - 0.15$) on the electrochemical behaviour of the anode were demonstrated. The cathode process on tungsten (W) has been examined in melts with CR's (1.3-1.5), The diffusion and mass transfer coefficients for the cathode process (W electrode) were determined. The findings suggest that the melt with CR 1.4 at 800 °C and the particle volume fraction around 0.09 are better parameters to use Cu- 10Al anode.

The effects of the temperature, the particle size and the phase composition of the dispersed material and its volume fraction in the suspension on the dissolution kinetics and the sedimentation velocity are studied. The experiments were carried out over the melts with cryolite ratios 1.3 and 1.5 in the range of 750-850 °C. Three different types of aluminium oxide were used. The Reynolds numbers for sedimentation have indicated the Stokesian regime. Typical alumina dissolution rates were in the range of 0.028-0.167 g·kg⁻¹·s⁻¹, which is close to the values reported previously. Sedimentation velocities were in the range of (0.05-3.61)·10⁻² m/s, which is several times higher than those obtained previously for $\phi = 0.24-0.32$ at 700 °C.

Based on the obtained results, the electrolysis of 1.4KF-AlF₃-Al₂O_{3(sat)} with Cu-Al anode and W cathode was performed. The purity of the aluminium using optical emission spectrometer was determined. The XRD, SEM-EDX methods were used to study the phases formed on the anode surface. The current efficiency of about 84.41% was attained and produced aluminium had a purity of 99.40%.

List of Publications

1. Padamata S.K., Yasinskiy A.S., Polyakov P.V. (2020). Anodic process on Cu-Al alloy in KF-AlF₃-Al₂O₃ melts and suspensions, *Transactions of Nonferrous Metals Society of China*, 2020, 30, 1419-1428.
2. Padamata S.K., Yasinskiy A.S., Polyakov P.V. (2020). Electrode processes in KF-AlF₃-Al₂O₃ melts, *New Journal of Chemistry*, 2020, 44, 5152-5164.
3. Yasinskiy A.S., Suzdaltsev A.V., Polyakov P.V., Padamata S.K., Yushkova O.V. (2020). Behaviour of aluminium oxide in KF-AlF₃-Al₂O₃ melts and suspensions, *Ceramics International*, 2020, 46, 11539-11548.
4. Yasinskiy A.S., Padamata S.K., Polyakov P.V., Samoilo A.S., Suzdaltsev A.V., Nikolaev A.Y. (2020). Electrochemical Behaviour of Cu-Al Oxygen-Evolving Anodes in Low- Temperature Fluoride Melts and Suspensions, *Minerals, Metals and Materials Series*, 2020, 591-599.
5. Padamata S.K., Yasinskiy A.S., Polyakov P.V. (2019). Electrolytes and its additives used in aluminum reduction cell: A review, *Metallurgical Research & Technology*, 2019, 116(4), 410.

Acknowledgements

The work was carried out at the Department of Non-ferrous Metals at *Siberian Federal University* under the supervision of Professor *Dr Petr Vasilievich Polyakov*. I am grateful for his advice and support.

I would like to especially thank Dr Andrey S. Yasinskiy for his support and involvement in the experiments and article writing.

Thanks to all the excellent staff at the Department of Non-ferrous Metals and especially Professor Dr Natalia V. Belousova for her help in strengthening my fundamentals in electrochemistry.

I am grateful to the Russian Fund for Basic Research for providing me with an adequate fund to conduct research.

Finally, I would like to thank my family and friends for their support at all the stages.

Sai Krishna Padamata

Krasnoyarsk, 2020

Table of content

Abstract	2
List of Publications	4
Acknowledgements	5
List of symbols	7
1. Introduction	9
1.1. Aluminium production: Importance and present problems	9
1.2. Hall-Heroult cell	9
1.3. An alternative technology	11
1.4. Purpose of this present studies	12
2. Literature Review	13
2.1. Inert anodes	13
2.2. Wettable cathode	27
2.3. Low-temperature melts	29
2.4. Sedimentation and dissolution of the alumina in melts	33
3. Electrode process in KF-AlF₃-Al₂O₃ melts	37
3.1. Experimental	37
3.2. Anodic behaviour of aluminium bronze electrode	41
3.3. Cathode process in the KF-AlF₃-Al₂O₃ system	63
4. Alumina behaviour in KF-AlF₃-Al₂O₃ melts and suspension	71
4.1. Experimental	71
4.2. The dissolution rate of alumina in KF-AlF₃ melts	74
4.3. Sedimentation of alumina in KF-AlF₃ melts and suspension	83
5. Current efficiency test	89
5.1. Experimental	89
5.2. Parameters and conditions	89
5.3. Oxide layer characterization	91
5.4. Aluminium purity	95
Summary	97
References	100

List of symbols

The following table only includes the most important symbols, unlisted symbols are included in the text when appeared in the beginning

Symbol	Meaning	Unit
a	activity	-
A	area	cm ²
CE	current efficiency	%
CR	cryolite ratio	-
c*	concentration in the bulk solution	mol cm ⁻³
C	concentration of electroactive ions	mol cm ⁻³
D	diffusion coefficient	cm ² s ⁻¹
d	diameter	cm
d _p	particle diameter	m
E	potential	V
E ^o	standard potential	V
E _p	peak potentials in voltammogram	V
E _{p/2}	half-peak potentials in voltammogram	V
E _{rev}	reversible potential	V
E _{i=0}	potential at i=0 in voltammogram	V
F	Faraday constant (96487)	C mol ⁻¹
g	Gravitational force	m s ⁻²
G	Gibbs free energy	J mol ⁻¹
G ^o	standard Gibbs free energy	J mol ⁻¹
H ^o	standard enthalpy	J mol ⁻¹
I	current	A
i	current density	A cm ⁻²
i _l	limiting current density	A cm ⁻²
i _p	peak current density	A cm ⁻²
k _s	mass transfer coefficient	cm s ⁻¹
M	molecular mass	g mol ⁻¹
p	reaction order	-
R	universal gas constant (8.314)	J K ⁻¹ mol ⁻¹
R	resistance	Ω
Re	Reynolds number	-

S°	standard entropy	$\text{J K}^{-1} \text{mol}^{-1}$
T	temperature	$^\circ\text{C}$
t	time	s
U_c	sedimentation velocity	m s^{-1}
V	volume	cm^3
WR	wear rate	cm year^{-1}
Q	Volumetric flow rate	$\text{m}^3 \text{s}^{-1}$
z	number of electrons	-
Δ	diffusion layer thickness	cm
ϕ	volume fraction	%
v	sweep rate	V s^{-1}

1. Introduction

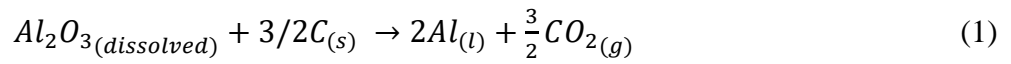
1.1. Aluminium production: Importance and present problems

Aluminium is the third most abundant element in our planet following oxygen and silicon, representing about 8% of the earth's crust [1]. The primary production of aluminium was almost 64.33 million tonnes in the year 2018 [2]. The demand for aluminium has only grown with time due to the growth of the infrastructure industry. Other than in infrastructure, aluminium is extensively used in the aerospace industry, automobile industry, electronics and household purposes due to its low density, durability, corrosion resistance as well as good electrical and thermal conductivity. Thus, aluminium is the second most used metal in the world only outranked by steel. Increasing aluminium production results in greenhouse gases emission and high-energy consumption. The main by-products of the electrolysis process are CO_2 , CO , CF_4 , SO_2 , C_2H_6 and HF . Primary aluminium production accounts approximately 2.5% of the world's anthropogenic CO_2 -equivalent emissions [3].

Currently, primary aluminium production is one of the largest energy consumers in the world with an approximate energy cost of 30% of entire aluminium production cost [4]. The aluminium industry should be committed to reducing the emission of primary CO_2 gas and greenhouse gases and be more energy-efficient. Many changes in the aluminium reduction cell have been made to reduce the energy consumption from time to time and many efforts are still required to reduce the specific energy consumption. Many strategic methods are already implemented at the government level in many countries. However, major technological changes need to be carried out for better outcomes.

1.2. Hall-Heroult cell

Hall-Heroult cell has been in use for more than a century for aluminium production. Charles Martin Hall [5] and Paul Héroult [6] developed and patented Hall- Héroult process independently in the late nineteenth century. The process is performed at around 960°C with the dissolution of Al_2O_3 in Na_3AlF_6 molten cryolite. A pre-baked carbon anode is used in this process, where the anode is consumed regularly by oxidation leading to the CO_2 formation. High purity liquid aluminium is produced at the cathode. The following reaction (1) takes place in general:



with $E^0 = 1.17 \text{ V}$ at 960°C

At industries, usually an anodic density of $0.8\text{-}1.0 \text{ A/cm}^2$ is used and the cell voltage is around 4.3V .

A schematic diagram of the Hall-Heroult cell is presented in figure 1. The prebaked carbon anodes are supported by the metal rods, where the transverse beam is connected to all the anodes in the cell. The carbon lining and the pool of liquid aluminium act as a cathode. The sideledge (frozen cryolite) acts as an insulator, preventing drastic fluctuation of temperature. The arrows represent the current direction are shown. The anode-cathode distance (ACD) is $4\text{-}5 \text{ cm}$. As the anode is consumed from the bottom regularly, the anodes should be lowered accordingly to maintain a constant ACD. The anode is usually replaced every three weeks. The replacement is time consuming, costly and hazardous process.

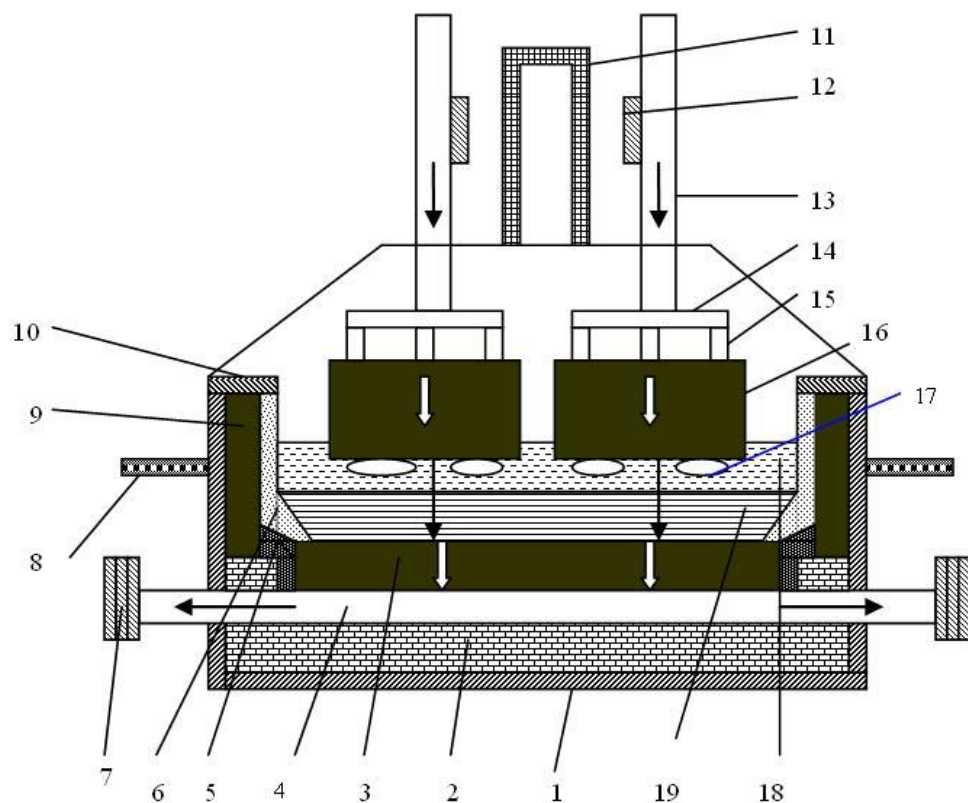
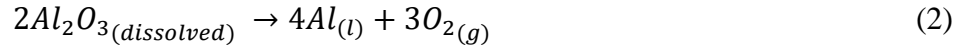


Figure 1. A schematic diagram of Hall-Heroult cell 1. casing, 2. lining, 3. hearth blocks (bottom), 4. cathode rods, 5. a peripheral seam, 6. frozen sideledge, 7. cathode bus, 8. grooved floor, 9. onboard block, 10. flange sheet, 11. gas collecting box, 12. anode bus, 13. anode rod, 14. traverse, 15. steel spider, 16. anode blocks, 17-gas bubbles, 18. electrolyte, 19. Liquid aluminium cathode.

1.3. An alternative technology

The use of inert anodes instead of carbon anodes can reduce rather eliminate the emission of CO₂ and other greenhouse gases. The below reaction (2) takes place by using oxygen-evolving inert anode:



with $E^0 = 2.2$ V at 960°C

Using inert anodes can reduce the CO₂ emission up to 80% assuming no change in the cell voltage and heat requirements [7]. The anode replacement process can be completely avoided which is economical and eliminates the process inefficiency and safety risks.

Many researchers have come up with different material types and investigated their properties at different conditions, although none of the materials could fit as an anode at an industrial scale. The anode should possess stability towards the molten salts at working temperature and have an adequate electrical conductivity. It is known that the oxide scales formed on the anode can protect it from the corrosion in the melts [8-10]. Using inert anodes can increase the specific energy consumption of the cell. The replacement of dimensionless liquid aluminium pool by vertical wettable cathodes can reduce the ACD between the electrodes and reduce the specific energy consumption, making the process energy efficient. Using low-temperature melts along with alumina suspension particles can improve the performance of the electrodes. Also, KF-AlF₃ based melts possess high alumina solubility. Using suspension electrolytes can reduce the contamination of produced aluminium from anode oxidation products. The schematic representation of the suspension electrolysis technology is shown in figure 2.

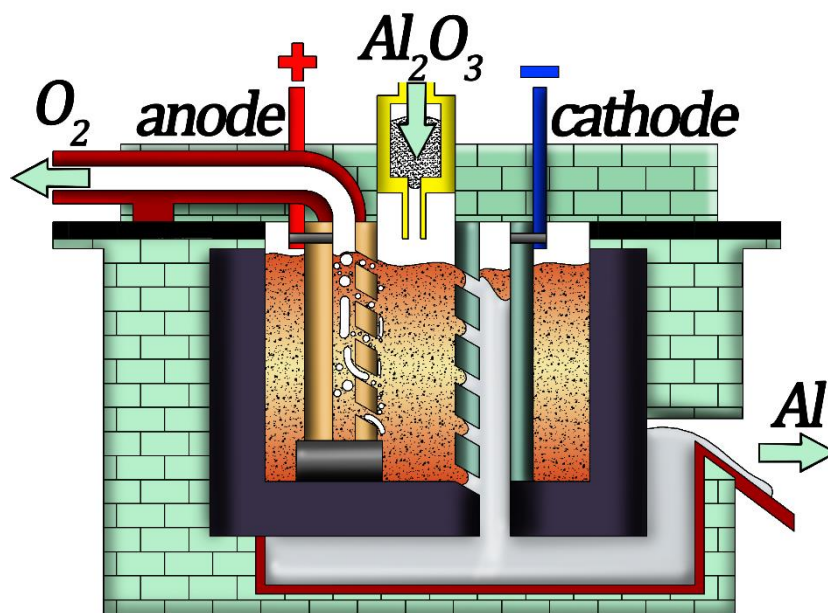


Figure 2. The scheme of suspension electrolysis apparatus

Most of the research on the inert anodes were tested in melts with high temperature. No literature can be found related to the testing of inert anode material in suspension. This thesis will give addresses the behaviour of aluminium bronze alloy in melts and suspension. The cathode process on tungsten electrode in low-temperature melts and most importantly the dissolution kinetics of alumina in melts and suspension.

1.4. Purpose of this present studies

The purpose of this thesis is to give a detailed assessment of the electrode processes in the low-temperature electrolytes and to determine the behaviour of aluminium oxide in low-temperature melts and suspension. The main aims are presented below:

- To determine the influence of alloy composition on the anodic process of Cu-Al based alloys in $\text{KF-AlF}_3\text{-Al}_2\text{O}_3$ electrolyte
- To understand the influence of alumina volume fraction in suspension on the behaviour of Cu-Al based alloy.
- To assess the influence of cryolite ratio (CR) $\left(\frac{\text{moles of KF}}{\text{moles of AlF}_3}\right)$, the temperature on the anodic process of the Cu-Al anode in suspensions
- To determine the cathode process on tungsten in KF-AlF_3 melts at different CR (1.2-1.5)
- To determine the sedimentation and dissolution rates of aluminium oxide in $\text{KF-AlF}_3\text{-Al}_2\text{O}_3$ electrolyte at different CR's (1.3-1.5) and temperatures (750-850°C)

2. Literature Review

This chapter gives an insight into the previously established facts about the metallic inert anodes, wettable cathodes, low-temperature electrolytes and suspension and solubility of alumina in cryolite melts.

2.1. Inert anodes

Replacing carbon anode with inert anode will eradicate the production of greenhouse gases through the process. De Nora [11] has suggested that the inert anodes should possess the following properties:

- Overtoltage less than 0.5 V at 0.8 A/cm² for oxygen evolution
- Anode current density, not more than 0.8 A/cm²
- High electrical conductivity
- Resistance towards fluoridation
- High chemical stability towards oxygen at 1050 °C
- Low cost and easy fabrication
- Ability to form protective oxide scale on the anode (cermets and metals)
- High mechanical strength
- Easy and stable electrical setup.
- High resistance towards thermal shock
- Easy maintenance
- Retrofittable in the present cell design

The properties described by de Nora are difficult to achieve all at the same time but recent advancements ensure the possibilities of achieving an inert anode. Nevertheless, by using inert anodes, greenhouse gases can be eliminated and it's economically beneficial to use inert anodes as the manufacture of consumable carbon anodes are expensive.

2.1.1. The necessity of inert anodes

Environmental consideration

The main reason that made industries to pursue inert anodes is because of their environmental benefits. Using oxygen-evolving anode for aluminium electrowinning can reduce the emission of greenhouse gases. Kvande and Haupin [7] estimated the CO₂ emissions thought aluminium electrolysis using inert anodes and is represented in table 1. Comparisons were made on the emission of CO₂ using different power sources.

Table 1. Specific CO₂-equivalent emissions from processes related to the aluminium production depending on the energy source [7]

CO ₂ emissions (tonne of CO ₂ /tonne Al)	Coal-fired power plant		Natural gas-fired power plant		Hydroelectric & Nuclear power plant		Average	
	Carbon	Inert	Carbon	Inert	Carbon	Inert	Carbon	Inert
Emission from electric power production	13.5	13.5	6.0	6.0	0	0	5.1	5.1
from bauxite mining and alumina production	2.0	2.0	2.0	2.0	2.0	2.0	2.0	2.0
from anode fabrication	0.2	0.2-0.3	0.2	0.2-0.3	0.2	0.2-0.3	0.2	0.2-0.3
from the electrolysis cell	1.5	0	1.5	0	1.5	0	1.5	0
CO ₂ equivalent from CF ₄ emission	2.0	0	2.0	0	2.0	0	2.0	0
Total emission	19.2	15.8	11.7	8.3	5.7	2.3	10.8	7.4
Reduction of CO₂ emission using inert anodes	-	18%	-	29%	-	60%	-	31%

Note: Equivalent cell voltage and heating requirements for the electrolysis cells with carbon and inert anode are considered

The estimations shown in table 1 predict the reduction of greenhouse emissions while inert anode technology for aluminium reduction. When the industries are committed to using nuclear or hydroelectric sources to power smelters, emission reduction up to 79% can be expected. Although this situation seems to be unreal as countries like China, India and South-East Asian countries highly rely on coal and gas-fired power. Inert anode technology also improves the working conditions of smelter workers. The use of inert anode can avoid the scenario of replacing the consumable carbon anode on a timely basis.

Energy considerations

Currently, the average energy consumption required to produce one kilogram of aluminium is around 15.1 kWh/kg of Al [12]. There has been a debate among the researchers regarding the real energy savings contributed by the inert anode usage [13]. A considerable amount of energy can be saved when the inert anodes are adopted along with the novel cell design [68].

Table 2. Standard reaction potentials and overvoltages using carbon and inert anodes [69]

Anode material	Cell reaction	E ⁰ (V)	Overtoltage (V)	Total
Carbon	$\text{Al}_2\text{O}_3 + 3/2\text{C} \rightarrow 2\text{Al} + 3/2 \text{CO}_2$	1.17	≈0.5-0.8	≈1.7
Inert	$\text{Al}_2\text{O}_3 \rightarrow 2\text{Al} + 3/2 \text{O}_2$	2.19	≈0.1-0.2	≈2.3

Note: The actual overvoltage vary with anodic current density and type of material in the case of inert anodes

Table 2 shows the reaction potential and overvoltages of the reactions for carbon and inert anodes. It is evident that additional 1V is required for the oxygen-evolution with inert anodes. The overvoltage of carbon is 0.4 – 0.5 V higher than on inert anodes.

The cell voltage can be reduced with the decrease in the anode-cathode distance (ACD). The ACD of around 4-5 cm is maintained in conventional Hall-Heroult cell between the carbon anode and pool of cathode aluminium. By using inert anodes, the ACD can be reduced as the geometry of the inert anode remains unchanged with time, unlike carbon anodes. A significantly low ACD can be maintained by using vertical cells with wettable cathode [13].

Electrolysis parameters were calculated by Jarrett for carbon and inert anodes with varying ACDs and the results are presented in table 3. About 31% of the energy can be saved using inert anodes along with suitable wettable cathode at ACD of 0.64 cm.

Table 3. Voltage drop with different materials and ACDs [14]

Anode type		Carbon	Inert	Carbon	Inert
ACD (cm)		4.45	4.45	1.91	0.64
Voltage drop (V)	Anodic	0.32	0.32	0.32	0.32
	Cathodic	0.60	0.60	0.60	0.60
	External	0.16	0.16	0.16	0.16
	Electrolyte	1.76	1.76	0.75	0.26
	Decomposition	1.20	2.20	2.20	2.20
	Overtoltage	0.60	0.15	0.15	0.15
	Total cell voltage		4.64	5.19	4.18
Energy* (kWh/ kg Al)		15.2	17.0	13.7	12.1
Total energy savings		-	5%	23%	32%

Note: Calculated for 91% of current efficiency, Includes 17% of energy-saving related to the carbon anode baking.

Economical benefits

Using inert anode technology is not only has environmental and energy-saving benefits but has economical benefits. Keniry [13] has mentioned the conditions at which the use of inert anode technology is beneficial by compared operating and capital cost for cells with inert and carbon anodes. They are as follows:

- The significant economic benefits can only be achieved when the anode along with wettable cathodes are used in vertical electrode cell.
- The inert anodes should have wear rate of less than 5mm/ year.
- Retrofitting inert anodes in the present cell is not economically benefitted.
- The drained cell can only offer potential with energy-saving if the aluminium production is increased and has the cell lifetime of over three years.

2.1.2. Anode materials

The inert anodes tested till date can be characterised into three different material types, ceramics, metals and cermets and each have its advantages and disadvantages. In this section, more generalised discussion on types of the inert anode which showed promising results will be done.

2.1.2.1.Ceramics

Ceramics were the primary interest of researchers because they believed that this material could be potential ones in fabricating the inert anode. Ceramics were first tested by Belyaev and Studentsov in 1937. Some ceramics (especially SnO₂) have the desirable property of low dissolution rate in the molten electrolyte at 960 °C but also possess poor electrical conductivity and low mechanical strength.

NiFe₂O₄ based anodes

Nickel ferrite was the first ceramic material tested by Alcoa. Du et al. [13] conducted a laboratory-scale experiment to know the anodic overvoltage and bubble behaviour of the anode. They discovered that the anodic overvoltage, cell voltage and back EMF can be reduced by the addition of dopants: 0.5wt. % V₂O₅ or 1wt. % MnO₂ or 2.5 wt. % TiO₂. They determined that the electrolytic bubble evolution on the surface of NiFe₂O₄ inert anodes, including bubble nucleation, growth, coalescence, growth again, migration and escaping, lasts for 79 seconds whereas for carbon anode it takes 102 seconds. Augustin [16] tested the corrosion behaviour of NiFe₂O₄ and stated that the solubility of the NiFe₂O₄ inert anode in molten cryolite electrolyte was less and they are stable towards oxidation, stating that the corrosion resistance of the anode was satisfying.

SnO₂ based anodes

In the patent Adler [17] stated the behaviour of SnO₂ anode, says that the material tends to dissolve slowly in molten cryolite. The solubility of SnO₂ anode was also found by Haarberg [18], which was 0.08 wt.% at 1035°C. The solubility of the anode can be reduced when the cell is operated at temperatures below 780°C. Adler in his experiment found that the SnO₂ shows good chemical stability but has high electrical resistivity and poor mechanical strength. Addition of dopants like Sb₂O₃, CuO, ZnO, Fe₂O₃ etc. improves electrical conductivity and mechanical properties. Experiments were performed by adding different compositions of dopants. SnO₂ + 2 wt.% Fe₂O₃ composition was sintered at 1200 - 1250°C, for 5 h and experiments were conducted and was observed that at low anodic current density the corrosion rate was less and contamination of metal was less. A sample with the composition of SnO₂ + 1 wt.% Sb₂O₃, + 2 wt.% Fe₂O₃ was made, where the density was improved by 50 % and also electrical conductivity of 220 S/cm was obtained compared to that of the SnO₂ + 2 wt.% Fe₂O₃ sample. SnO₂ + 2wt% Sb₂O₃, + 2wt% CuO composition has a better electrical conductivity of 440 S/cm. The main backdrop of the anode when it combines with the dopants is the high solubility of dopants in molten cryolite. Dopants leach from the anode at the time of electrolysis and demands for high cell voltage and cause mechanical damage to the anode. The anode with dopants can still be used at low bath temperatures and can have a longer lifetime.

NiO-Li₂O based anodes

Laboratory tests were performed by Zaikov et al. [19], and the corrosion rate of NiO-(2.5wt.%)Li₂O material was determined by keeping the note of the anode's weight while the electrolysis process was going on. They determined that the corrosion rate of the anode can be reduced by increasing the sintering temperature and sintering time during the anode preparation, which results in the decrease of anode's porosity. The anode was tested with fluoride melt at 700°C for 4.5 hours, and no physical damage to the anode was observed.

2.1.2.2. Metals

For many decades, metals have been regarded as the prominent material for the preparation of inert anodes because of its high mechanical strength and better electrical conductivity than ceramics and cermets. Some of the advantages of metal anodes are good thermal shock resistance, low porosity, easy fabrication into required sizes and shapes, easily electrically connected to the cell. But it also has disadvantages such as poor corrosion resistance,

tendency to dissolve in the electrolyte at higher cell operational temperature, expensive than ceramics and cermets.

Aluminium Bronze

In the laboratory-scale experiment, Glucina et al. [20] have investigated two Cu-Al alloys which they believed to be potential materials to fabricate anodes for aluminium electrolysis. Anode(AB1) was a binary alloy with a composition of 90.25 wt.% Cu, 9.39 wt.% Al and little amounts of 0.02wt.% Ni, 0.10wt.% Fe and impurities of 0.24 wt%. The Second anode(AB2) was alloyed with 77.81wt.% Cu, 10.50 wt.% Al, 5.10 wt.% Ni, 4.95 wt.% Fe and impurities being 1.64 wt%. Experiments were performed on anodes AB1 and AB2 twice, with and without an Al-based oxide scale. It was observed that in AB1(no oxide layer or no pre-treated) two oxide layers were formed, the first layer was alumina with a thickness of 500 μm and the second layer was Copper oxide with a thickness of 200 μm . High polarization voltage was obtained in this case. Unlike AB1(no oxide layer), AB2 (no oxide layer) was stable and had only one layer formed of copper oxide. Both the alloys, AB1 and AB2 performed well as an anode with a steady voltage which was operated at an anode potential of 2.1 V. It was observed that the anodic polarisation was between 0.15 - 0.2V which is lower than the carbon anode. Huge mass loss of the anode at the later stage of electrolysis occurred which led to anode loss and contamination of metal produced.

Cu-Ni-Fe based anodes

Metallic anodes have the disadvantage of being corrosive but the Cu-Ni-Fe alloy has been showing some good results being less corrosive than the rest of the metal anodes [21-23]. When it comes to Cu-Ni-Fe anode, it has the ability to generate a protective surface layer of NiFe_2O_4 . NiFe_2O_4 layer has a tendency of passivating slowly in molten cryolite which reduced the anode's corrosion rate. A Cu-Ni-Fe metallic anode was doped with oxygen [24], with composition of 65 wt.% Cu, 20 wt.% Ni & 15wt.%Fe and tested at a temperature (700°C) with potassium cryolite. High corrosion resistance was obtained with a wear rate of 0.8 cm/year and impurities of 0.2wt% were found in the aluminium metal produced. Cu metal wt.% in the alloy places a vital role in the formation of a NiFe_2O_4 protective layer and a low percentage of Cu results in instability of anode in the electrolysis process. Firstly, CuO layer is formed at the initial stages of electrolysis which acts as a protective layer for NiFe_2O_4 inner protective layer of the anode [25]. In the later stages, the CuO layer dissolves and leads to the contamination of aluminium produced. A study was conducted to overcome these criteria, where 5 wt.% Cu was replaced by (M = Sn, Ag, V, Nb, Ir, Ru) and CuO layer will be

replaced by MO, each sample was tested for their respective oxide scale thickness, homogeneity and solubility. The results obtained showed that Nb was showing promising results with its thick oxide scale and homogeneity [26].

De Nora Metallic inert anode

Nguyen and de Nora [21] introduced metallic anode Nickel-Iron based alloy with semi-conductor Nickel-cobalt mixed oxide as an outer coating. Usually, Ni-Fe based alloy is stable towards oxygen due to the formation of nickel ferrite protective scale as an outer layer but nickel is vulnerable at fluoridation reaction with gaseous aluminium fluoride when it is part of Ni-Fe alloy. In the metal-oxide interface, nickel fluoride layer is formed which is electrically non-conductive. If Fe content is increased to avoid the fluoridation of Ni, the decrease in oxidation resistance occurs. This scenario can be avoided by coating Ni-Fe anode with Ni-Co coating. This coating acts as a barrier between the Ni-Fe anode and the aluminium fluoride gas, which will avoid the formation of nickel fluoride layer from fluoridation of nickel. The cobalt oxide layer is formed on the Ni-Fe anode which is stable towards the fluoridation and protects the Ni from forming nickel fluoride. Coming to the experimental procedure, the anode was tested at 100 – 300 A cell for different durations. At stable conditions, the anode metal core dissolution rate was 2 mm/year and the CoO layer dissolution rate was 3 mm/year. Estimated anodic lifetime was 1 year with less metal contamination rate of 1340 ppm at laboratory scale and 995ppm at an industrial scale. The anode surface factor was 2.3 for an industrial anode which is 0.9 less than laboratory anode. With the presence of Co-Ni coating, a thermodynamic penalty of 620 mV versus the carbon anode was observed, but it can be compensated by increasing the active surface of the anode. Overall, anode possessed promising results with high electrical conductivity and good corrosion resistance.

2.1.2.3. Cermets

Cermets are a combination of two phases: Ceramics and Metals. Cermets have the desirable properties of both the phases: high electrical conductivity of metals and good chemical stability of ceramics. The use of cermet anodes for aluminium electrolysis was proposed by Alcoa in the 1980s as ceramics were showing poor electrical conductivity.

Fe-(NiFe₂O₄ + NiO) based anodes

Ray and Rapp [27,28] patented a cermet anode with a composition of 50 wt.%NiO, 20wt.%Fe and 30 wt.% NiFe₂O₄ . The microstructure of the anode's surface area was recorded and it was seen that there were nickel ferrite matrix and linearly distributed metallic Fe particles on

the anodic surface which resulted in good electrical conductivity of the anode. It was stated that electrical conductivity is varied concerning the type of preparation. The electrical conductivity of 700 S/cm was obtained when hot pressing was performed to prepare the anode. When the concentration of iron was reduced from 20 wt.% to 7 wt.%, the drastically low electrical conductivity of 19 S/cm was observed. Anode possesses good corrosion resistance with mere contamination of metal produced. At higher anodic current densities, higher current efficiency was achieved and contamination of metal was less. This Fe-(NiFe₂O₄ + NiO) anode is the pioneer of the research towards cermet anodes.

Cu-Ni- NiFe₂O₄ –NiO based anodes

Liu et al. [29] conducted experiments on cermet anode of composition 15.3 wt.%Cu, 8.3 wt.% NiO, 1.7 wt.%Ni and 74.7 wt.% NiFe₂O₄. The alloy is prepared in two steps: cold pressing and sintering the powdered form of all the materials. The aluminium electrowinning was performed at 960°C. It was observed that only NiFe₂O₄ layer was formed as the outer scale whereas NiO layer was expected to be formed on the anode. As time progressed, the NiFe₂O₄ layer was becoming thicker resulting in the disappearance of the NiO layer. To find the corrosion behaviour of the anode, the purity of electrolyte and produced aluminium was checked. It was observed that the Cu was dissolved rapidly in the electrolyte whereas no traces of Ni and Fe were observed in it. Reducing the percentage of Cu can reduce the corrosion rate but at the same time decreases the electrical conductivity of the anode. Much research has to be conducted to improve the anodic properties.

NiFe₂O₄ –Cu based anodes

Tian et al. [30] prepared a cermet anode of two phases, NiFe₂O₄ and Cu. The copper metal was added to increase electrical conductivity and maintain mechanical stability. Two anodes with different compositions were made, NiFe₂O₄ –5 wt.% Cu and NiFe₂O₄ –20 wt.% Cu. The effects of preparation method on the physical structure and anodic properties were studied. The desired phase composition on the anodic surface can be obtained by controlling the oxygen's partial pressure between the decomposition oxygen pressures of NiO and Cu₂O. The high relative density of the anode can be obtained by increasing the sintering time and temperature. The preparation process of the anode was difficult due to the low melting point and poor wetting characteristics of copper when it is combined with NiFe₂O₄. The sintering temperature of the anode with 20 wt.% Cu was 1000°C whereas for 5 wt.% Cu in the alloy, sintering can be performed at 1250°C. Decreasing the metal content in the anode increases the sintering temperature, but at the same time reduces the electrical conductivity of the

anode. By adding metals such as Ni and Co which have a higher melting point and good wetting characteristics when alloyed with $\text{NiFe}_2\text{O}_4 - \text{Cu}$ alloy results in a good relative density. Sintering can be performed at high temperatures which helps to reduce the porosity of the anode.

Cu₂O – Cu based anodes

$\text{Cu}_2\text{O} - \text{Cu}$ cermet anode was tested by Feng et al. [31], they stated that the anode is partially inert and can be used to produce Al alloy and Al with little content of Cu. $\text{Cu}_2\text{O} - \text{Cu}$ cermet anode was tested for its thermal corrosive behaviour in $\text{Na}_3\text{AlF}_6 - \text{AlF}_2 - \text{Al}_2\text{O}_3$ electrolyte at 960°C for different geometrical. A passive layer of CuAlO_2 was observed on the anodic surface while performing SEM and the CuAlO_2 layer thickness and density were increased with increasing corrosion time. It was stated that the density and thickness of the layer were increased rapidly in the initial stages of the electrolysis process but was later slowed down as the time progressed. As the Cu content in the anode increased, the thermal corrosion rate also increased i.e. at 10 wt% of Cu in the anode, the thermal corrosion rate was $0.68 \text{ mg/cm}^2\text{h}$, whereas at 35 wt% of Cu in the anode, the thermal corrosion rate was about $2.63 \text{ mg/cm}^2\text{h}$. Also, the grain size of the Cu particles affects the thermal corrosion rate (directly proportional). The researchers stated that the ideal content of Cu would be 25 wt% where the thermal corrosion rate of $1.5- 7.2 \text{ mg/cm}^2\text{h}$ and less than 6.3 wt% of Cu content in the produced aluminium were observed. Researcher's state that this type of anodes will gain demand in the near future as the prominence of aluminium alloy is more than pure aluminium.

Ni(NiFe₂O₄ – 10NiO) based anodes

Corrosion behaviour of $17\text{Ni}(\text{NiFe}_2\text{O}_4 - 10\text{NiO})$ cermet anode was tested by TIAN et al. [32], The anode was prepared at different sintering atmospheric conditions and electrolysis was conducted in $\text{Na}_3\text{AlF}_6 - \text{Al}_2\text{O}_3$ electrolyte melt. The anode prepared in the atmosphere with an oxygen content of $2 * 10^{-3}$ possessed corrosion rate of 2.71 cm/a whereas anode prepared in a vacuum has a corrosion rate of about 6.46 cm/a . A thickness of the layer of $50 \mu\text{m}$ was recorded when the anode was prepared at an atmosphere with the oxygen content of $2 * 10^{-3}$ and in the case of anode prepared in the vacuum, the densification thickness layer of $30\mu\text{m}$ was observed. Also, the decrease of oxygen content in the sintering atmosphere increases NiO and Fe(II) content in $\text{NiFe}_{2x}\text{O}_{4-y-z}$ which leads to the poor corrosion resistance of the material and rapid mass loss in the anode can be observed.

2.1.3. Unconventional Inert Anode

Solid Oxide Fuel Cell

Research on inert anodes was mostly on the conventional type, but there were also attempts made to achieve unconventional anodes. R.A.Rapp [33] designed a non-consumable solid oxide fuel cell-type anode for the aluminium electro-winning process. The anode consists of a nickel tube (conductor), into which the combustible fuel is sent. The bottom surface of the anode is layered with the zirconia-based O^{2-} conducting electrolysis. When power is supplied, oxidation of combustible fuel occurs resulting in the evolution of oxygen as a primary anodic process. Figure 3 shows the working principle of the SOFC type anode.

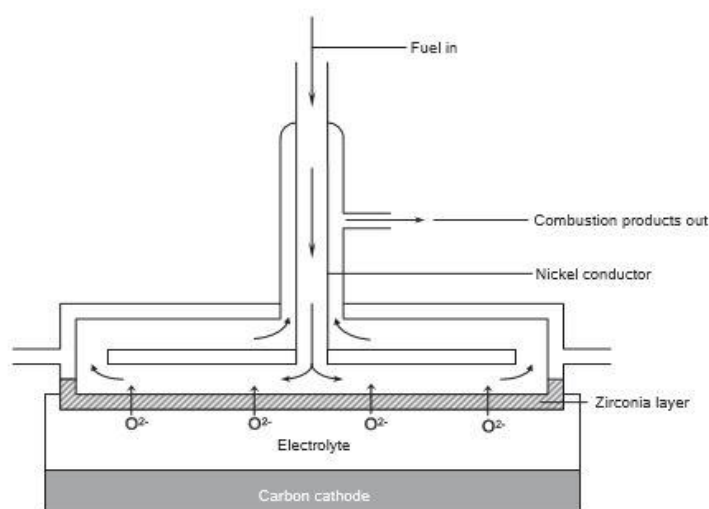


Figure 3. Schematic diagram of Solid Oxide Fuel Cell

R.A.Rapp claimed that the SOFC type anode can be retrofitted in the present Hall Heroult cell without any changes in the cell geometry and claimed that the cell would possess all the mandatory anodic properties. Later stages of research revealed that the zirconia layer in the anode is easily soluble at high-temperature cryolite melt leading to zirconia layer depletion.

Bipolar Electrodes

Making bipolar electrodes for the industrial aluminium reduction cell has been the ultimate goal for the researchers. The bipolar electrode consists of both anode and cathode with an insulator separating them. Few advantages can be acquired by using a bipolar electrode like the geometry of the cell can be reduced, amount of electricity used in electrolysis process can be reduced drastically, and cell maintenance cost can be reduced. Swiss aluminium patented the first bipolar electrode for the Hall Heroult's cell in 1976 [34]. In the patent, they mentioned that the cell would contain two bipolar electrodes consisting of $SnO_2 + Sn_2O_3 +$

CuO anode layer and graphite cathode and an intermediate nickel layer which separates anode and cathode. They are made by pressing the three layers at high temperature.

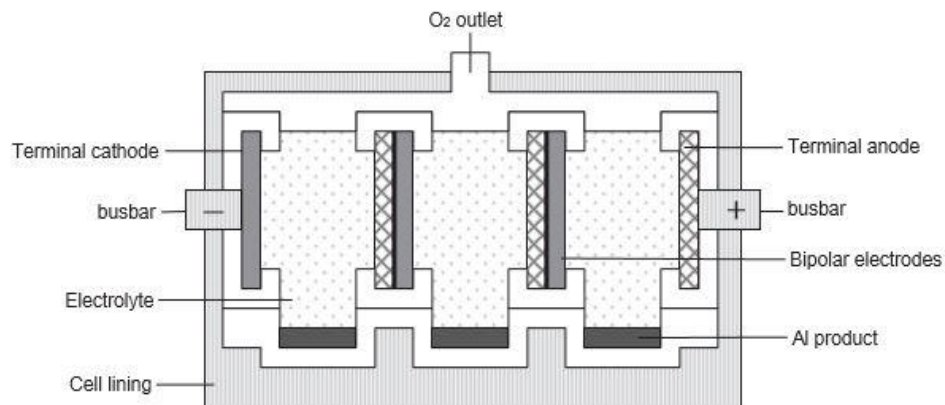


Figure 4. Schematic diagram of the cell containing a bipolar electrode.

Many other bipolar anodes were patented, e.g. cermet anode (tin oxide with additives like zinc oxide, antimony oxide and/or vanadium oxide) and titanium boride cathode. But none of the bipolar anodes has shown an impact on the industrial cell.

Depolarised Gas Anode

Haarberg et al [35] developed a depolarised gas anode. The necessity to use this anode arises due to the fact that when the inert anodes are used in the aluminium electro-winning, reaction (3) takes place with Gibbs energy of 1283.316 kJ/mol at 960°C. The reduction of the ohmic voltage in the electrolyte can be attained by redesigning the cell. The CO₂ produced at the anode can also be reduced by using an oxidizable gas which can depolarise the anodic process. In the laboratory-scale process, the electrolyte used is the molten CaCl₂ with CaO and the AgCl additive to control the cathodic reaction.

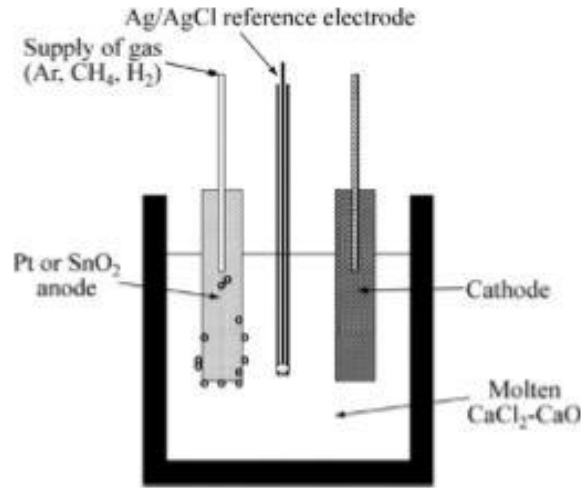
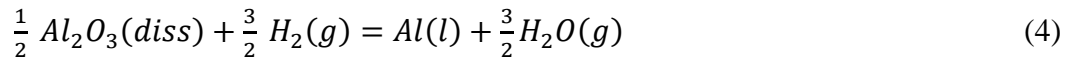
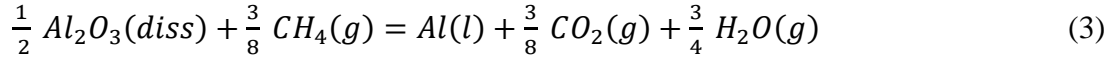


Figure 5. Schematic diagram of the depolarised gas anode

Two different anodes were tested with two different materials, one being a metal Platinum and the other being a ceramic Tin Oxide. The reference electrode was Ag/AgCl to determine the anode overvoltage. An experiment was conducted in an atmosphere of dry argon to avoid and eliminate the contamination of air by moisture and oxygen. The methane and hydrogen gas are supplied into the anode during the electrolysis process and reaction (3) takes place when methane and reaction (4) when hydrogen is supplied.



The behaviour of inert anodes of tin oxide and platinum was studied in separate experiments. The laboratory studies state that when hydrogen is introduced into the anode during the electrolysis process, a significant amount of anodic potential was lowered (0.3-0.5 V) while using platinum anode. While using a Tin oxide, 0.1 V of anodic potential was lowered. Both the anodes showed potential and further improvements should be made.

2.1.4. Anode Design

The geometry of the anode plays a vital role in its performance. Only metallurgical properties of the anode were focused and very less attention was given to the mechanical properties of the anode. Antille et al. [32] discussed the engineering related to the industrial-scale de Nora anodes for a 25kA test cell. Computer modelling was used to simulate the electrical and hydrodynamic behaviour of the anodes with different geometries.

Oxygen Gas Flow

The oxygen gas evolved at the anodic surface has to be removed quickly as soon as it is evolved to reduce the anode corrosion rate. Oxidation on the anodic surface takes place and leads to corrosion if the oxygen produced on the surface of the anode stays in contact with it for a longer time. Slotted anodes containing cylindrical bars are preferred rather than monolithic anode blocks, as the gas escape quickly from the surface of slotted anodes and the statement was supported by Sides and Prentice [36], where they conducted tests and found that approximately 0.4 V of voltage is saved when slotted anodes are used. It is also stated that when anodes are inclined, the gas escapes quickly from the surface of the anode and the bubble size is less.

Current Density Distribution

The anodic life is expected to be less when the anodic current density is higher and the anodes with lower anodic current density are recommended. The anodic current density of circular cross-section anode and triangular cross-section anode were measured and it was found that the current density of circular cross-section was high compared to that of triangular cross-section anode but it was also observed that the edges of the triangular cross-section anode possess higher current density. So, it is advisable to have an anodic geometry somewhere between circular and triangular.

2.1.5. Gas evolution regularities

Oxygen is believed to be the major anodic product during sustainable electrolysis with inert anodes in oxide–fluoride melts and suspensions. Oxygen bubbles are generated from the saturated liquid on the preferable nucleation sites and growth by absorption of dissolved gas and coalescence.

Based on the results of electrolysis tests in suspension [37], gas evolution in an H₂SO₄ suspension with properties close to that of the suspensions studied and model calculations [38], a motion scheme and patterns of anode gas bubbles formed on an oxygen-evolving electrode as a result of suspension electrolysis were demonstrated. The interfacial tension of the melt is almost 2 times higher than that of an aqueous solution, which will affect the interfacial energies at the electrode-gas-electrolyte boundaries. We assume that the presence of alumina solid particles levels the influence of surface energy and the viscosity and density of suspensions become the main criteria for the dynamics of bubble growth. Two different kinds of bubbles could be observed at the same time (figure 6): the slugs (9) and the small bubbles. The slugs move through the channel (2, 5, 6) with less density than that of the other layers. The channel is formed by the slugs itself through the particles transport to the top layer

(1, 2, 3) where the small bubbles and the particles are accumulated. After the bubble is grown in anodic liquid (less dense) layer (4) and detached from the surface it moves down due to the electrolyte backflow till it coalesces with the slug or other small bubbles or enters the interslug three-phase layer (6). Movement of the slugs transmits the motion to the moving two-phase layer (7), which stays bubble-free while another two-phase layer (8) remains motionless. An increase in the alumina fraction in the suspension enhances the hydrodynamic resistance and complicates the convective transfer of anode gases, increases the electrical resistivity due to an increase in the volume of the non-conducting phase (gas bubbles and alumina particles).

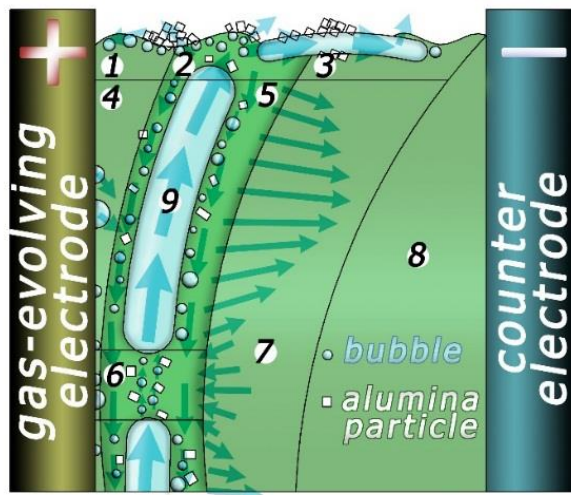


Figure 6. Scheme of movement (arrows) of bubbles, alumina particles and electrolyte volumes in the anodic space of suspension [37]: 1) anode top layer, 2) top part of gas channel, 3) top layer, 4) anodic liquid layer, 5) gas channel, 6) interslug three-phase layer, 7) moving two-phase layer, 8) motionless two-phase layer, 9) slug.

The dependence of the three-phase layer thickness vs. distance from the bottom and the frames on the recorded bubble movement at the gas-evolving electrode obtained on the water model are presented in figure 7. The water model was designed for dimensionless similarity criteria: modified Reynolds number $Re^*=16.24$, Galileo number $Ga = (1.78...2.00) \cdot 10^{10}$, Weber number $We = (5.96...9.8) \cdot 10^{10}$, geometrical simplex $h/l=7.5$ (h and l denote the electrode height and interelectrode distance respectively) and $\phi=0.3$. The alumina suspension based on 20 % H_2SO_4 water solution was used as an electrolyte at 50 °C [37].

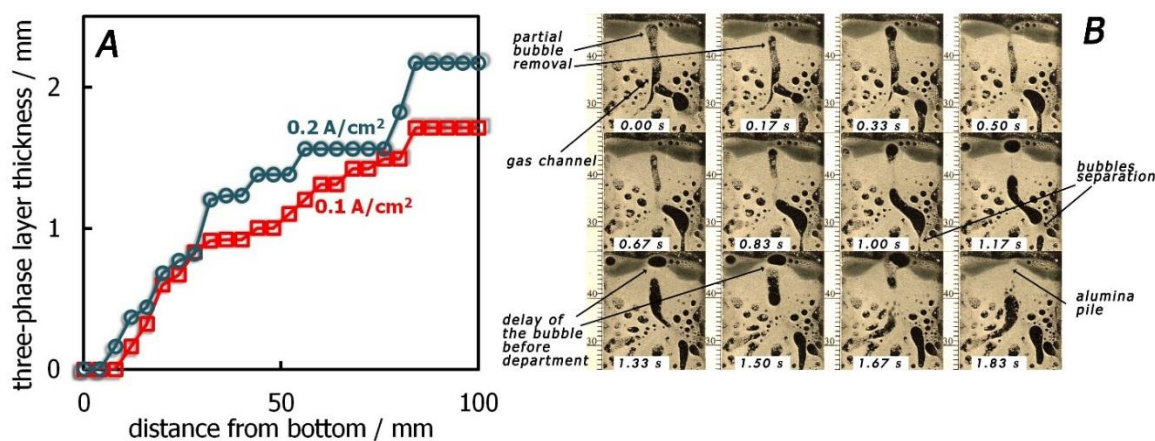


Figure 7. Dependence between the three-phase layer thickness and the distance from the bottom (height) for anodic evolution of oxygen bubbles in H_2SO_4 solution at 0.1 and 0.2 A cm^{-2} (A) and the frames with recorded gas evolution (B) at 0.05 A cm^{-2}

It was shown that due to a decrease in temperature, current density, and the appearance of the hydrodynamic resistance, the velocity of anodic gas bubbles in suspensions decreases by 10 times to be as low as $1.0\text{--}2.3 \text{ cm s}^{-1}$. The width of the bubbles is comparable ($0.8\text{--}2.3 \text{ mm}$) to the one in Hall–Heroult cell [69], however, the length can reach more than 20 mm. Due to the low velocity, increased gas fraction and hydrodynamic resistance, a significant horizontal component of the bubble velocity appears in the direction away from the vertical anode. All this leads to the fact that the main mechanism of the anode gases motion in the suspension becomes to be the slug flow. The observations follow to the conclusion that forced gas removal (through some kind of porous electrode) is highly desirable for the technology.

2.2. Wettable cathode

In the Hall–Heroult cell the carbon lining along with the liquid aluminium act as a cathode. As the carbon lining is not wetted by the liquid metal, the aluminium pad should have a minimum thickness of about 10 mm to work smoothly [40]. When an insufficient amount of liquid metal is present, the molten aluminium forms smaller puddles creating unstable functional conditions. This is hazardous as the magnetic forces will enforce the moment of the liquid puddles at high speed which can be thrown out of the cell. On the other hand, the development of an inert wettable cathode and implementing it at the industrial level can avoid the problems related to unstable ACD and encourage the idea of vertical electrode cell.

Titanium diboride is considered as the most promising material to work as an aluminium wettable cathode. The following properties are possessed by TiB_2 :

- Good electrical conductivity

- The ability to be resistive to corrosion by molten salts
- Very low solubility in aluminium

The cathode processes on materials such as liquid aluminium, carbon, graphite, titanium diboride (TiB_2) and tungsten (W) were studied until date [39-47]. Along with TiB_2 , W is considered as a promising candidate to be used as a wettable cathode. Initially, carbon and graphite cathode processes were examined and the results show the Al_4C_3 formation on the cathode surface leads to the passivation and later corrosion of the cathode [48-50]. Although, W forms an intermetallic compound Al_4W with Al interaction on its surface, no significant effect on the kinetic parameters of the cathode process were observed [52,53]. In addition, W shows relatively good chemical resistance towards the liquid aluminium [51].

Cathode process in low-temperature melts

Much attention was paid to the study of cathode polarization in melts and suspensions [52,53]. The effect of the temperature (670–800 °C), cathode material (tungsten, glassy carbon), ratio $[\text{KF}]/[\text{AlF}_3]$ (1.3 and 1.5 mol mol⁻¹), ϕ (0; 0.18 and 0.30) on the kinetic parameters of the aluminium reduction from the $\text{KF}-\text{AlF}_3-\text{Al}_2\text{O}_3$ melts and suspensions were studied both under stationary and non-stationary conditions. Figure 8 shows the typical stationary and non-stationary polarization curves on tungsten.

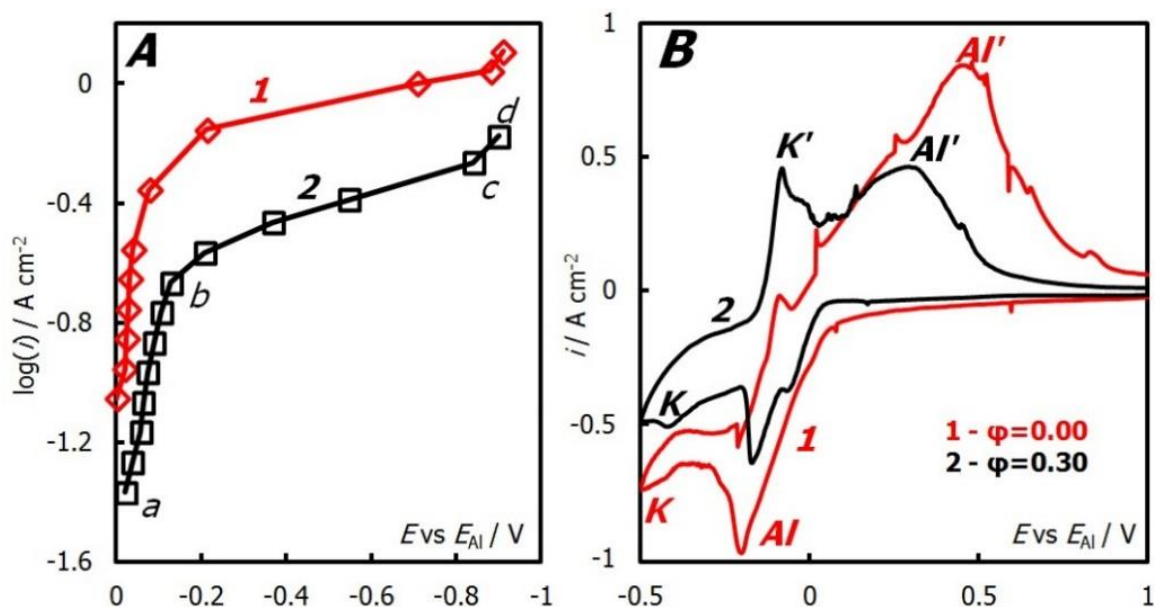


Figure 8. Stationary polarization curves (A) and voltammograms (B) obtained on tungsten in a saturated $(1.3\text{KF}-\text{AlF}_3)-\text{Al}_2\text{O}_3$ melt and suspension at 750 °C [53].

According to non-stationary voltammograms (figure **8B**) aluminium reduction starts at a potential of about 0 V relative to the aluminium electrode potential with the appearance of a cathode peak (*Al*) in the potential region of $-0.3...-0.45$ V. With a further potential shift, the negative current of aluminium reduction persists up to the wave of potassium evolution (*K*) at potentials more negative than -1.1 V. On the anodic part of the curve the peaks of potassium (*K'*) and aluminium (*Al'*) oxidation are observed. Based on these observations, a scheme of the cathodic process in $\text{KF-AlF}_3\text{-Al}_2\text{O}_3$ melts is proposed, which includes parallel electrochemical stages of the discharge of fluoride and oxide-fluoride ions, as well as the probability of partial salt passivation of the cathode and the interaction of reduced aluminium with KF.

Introduction of Al_2O_3 particles and increase in their fraction in suspension increases cathodic overvoltage and decreases the limiting current density of aluminium reduction under stationary conditions for all investigated temperatures and $[\text{KF}]/[\text{AlF}_3]$ ratios. The using KF-AlF_3 systems widen the electrochemical window for the aluminium electrodeposition without an alkali metal reduction. In $(1.3\text{NaF-AlF}_3)\text{-Al}_2\text{O}_3$ melts at 860 °C sodium is reduced at a potential $0.2...0.25$ V more negative than the aluminium reduction potential [54,55]. This can be a significant obstacle to the sustainable electrolysis of the suspension since the recirculation of the cathode layer in suspensions is extremely difficult.

2.3. Low-temperature melts

2.3.1. KF-AlF₃ melts

The low-temperature melts were desirable for the electrolysis for a long time as they reduce the corrosion rate of the cell parts and increase the cell lifetime. Pure potassium cryolite dissolves more alumina than sodium cryolite. But the electrical conductivity of the potassium cryolite is rather low and decreases with the decrease of the temperature ($680\text{-}820^\circ\text{C}$) and increases with the increase in CR between 2.2 and 3.0. The equation (5) was formulated by using the regression modelling from the data acquired by Kryukovsky et al. [56].

$$\kappa = 0.0026 \cdot T - 0.8788 \quad (5)$$

Xu et al. [57] calculated the thermodynamic properties of KF-AlF_3 melts and determined that the complex ions formed are AlF_6^{3-} , AlF_5^{2-} and AlF_4^- similar to that of the NaF-AlF_3 and LiF-AlF_3 systems. The AlF_6^{3-} complex ion tends to be more stable in the KF-AlF_3 system than in the NaF-AlF_3 or LiF-AlF_3 melts due to the weakest action of cation K^+ on the ligand F^- . It makes the electrical conductivity of KF-AlF_3 lower than that of the NaF-AlF_3 system where

AlF_6^{3-} is dissociated into AlF_5^{2-} , AlF_4^- and AlF_3 in steps resulting in the easy charge carriers transportation. The same was stated by Tsirlina et al. [58] and Nazmutdinov et al. [59].

The electrical conductivity of $\text{KF} - \text{NaF} - \text{AlF}_3$ melts were investigated by Yang et al. [60]. The addition of KF in the sodium cryolite results in the decrease in the melting temperature. The continuously varying cell constant technique was used to measure the electrical conductivity of $\text{KF} - \text{NaF} - \text{AlF}_3$ melt with varying parameters like NaF content, alumina content and CR at different temperatures. The effect of the NaF content on the conductivity of $\text{KF} - \text{NaF} - \text{AlF}_3$ melt was examined. The cryolite ratio of this particular melt is the sum of mole fraction of NaF and KF divided by the mole fraction of AlF_3 . At $\text{CR} = 1.3$ the conductivity of the melt was measured with the following contents:

1. KF 57.4 mol%;
2. NaF 15 mol%, KF 42.7 mol%;
3. NaF 30 mol%, KF 27.4 mol%;
4. NaF 45 mol%, KF 12.4 mol% and
5. NaF 57.4 mol%

The temperatures were in the range 750-820°C with 10°C interval. The dependence can be expressed by equation (6).

$$\kappa = 0.002776 \cdot T + 0.001393 \cdot C_{\text{NaF}} - 0.0192 \quad (6)$$

where C_{NaF} is the mole % of NaF in the $\text{NaF} - \text{KF} - \text{AlF}_3$ system.

This is because the radius of Na^+ ($1.02 \times 10^{-10}\text{m}$) is smaller than K^+ ($1.38 \times 10^{-10}\text{m}$) and hence, the Na^+ ion migration speed tends to be higher than that of K^+ , which is the reason why the electrical conductivity of the melts increases with the increase of NaF content. Similarly, the electrical conductivity was calculated by varying the alumina content and changing CR for different temperatures between 750 - 820°C with 10°C interval and the findings show that with an increase in the alumina content, the electrical conductivity decreases and with an increase in CR, the conductivity increases.

Apisarov et al. [61] measured the electrical conductivity of the $\text{KF} - \text{AlF}_3$ system containing LiF and alumina. It was determined that by increasing LiF content, the electrical conductivity of the molten electrolyte increases and by increasing alumina content, the electrical conductivity slightly drops. Equation (7) shows the relation between the conductivity, the temperature and the content of alumina in the electrolyte composition at $\text{CR}=1.3$ (KF mol% / AlF_3 mol%)

$$\kappa = 0.1336 + 0.001547 \cdot T - 2.25 \cdot C_{Al_2O_3} \quad (7)$$

where, $C_{Al_2O_3}$ is the wt.% Al_2O_3 in $KF - AlF_3 - Al_2O_3$ (CR= 1.3) electrolyte. $T = 680-800^\circ C$.

For all compositions (w.r.t. to LiF content) the electrical conductivity of the melt increases with a temperature rise. The equation (8) was derived as below:

$$\kappa = 0.0351 + 0.001692 \cdot T + 1.375 \cdot C_{LiF} \quad (8)$$

where, C_{LiF} is the wt.% LiF in $KF - AlF_3 - LiF$ (CR= 1.3) melt. $T = 680-800^\circ C$

The liquidus temperature and the density of the $KF - AlF_3$ system with the addition of $AlPO_4$ to the melt was determined by Vaskova et al. [62]. The liquidus temperature and the density of the system was determined for $1.5 \leq CR \leq 3$ and at different $AlPO_4$ contents. The liquidus temperature of the system tends to decrease with the increase in the $AlPO_4$ content and as the CR is reduced, the liquidus temperature of $(KF - AlF_3) - AlPO_4$ system falls (figure 9).

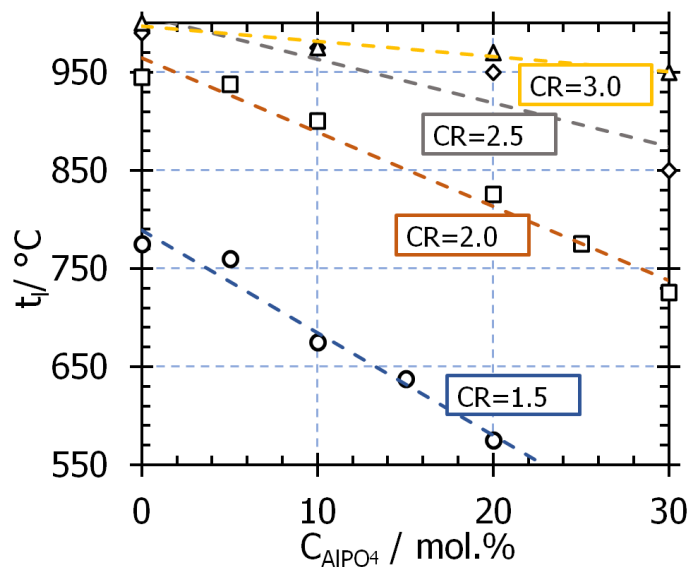


Figure 9. Liquidus temperatures of $(KF - AlF_3) - AlPO_4$ system at different cryolite ratios with increasing $AlPO_4$ content [62]

2.3.2. Suspension electrolyte

The concept of suspension electrolyte was developed by T.R. Beck [63]. The main idea of using suspension electrolyte is to maintain it saturated with alumina, to reduce the solubility of oxides, to minimize the corrosion rate of non-carbon anodes and to increase the cell lifetime. In [63] a eutectic $NaF - AlF_3$ melt with and without the addition of $KF - AlF_3$ and $LiF - AlF_3$ was examined in 1-40 A laboratory cell at around $750^\circ C$. The copper anode and TiB_2 cathode were used and the alumina particles were fed in suspension at the anode-

electrolyte interface to avoid anode effect. The oxygen evolved at the anode keeps the alumina particles suspended, it is important to have a continuous removal of the aluminium from the cell having an auxiliary anode to avoid the stoppage of oxygen evolution from the anode.

The cell would have a thermodynamic potential of 2.35V. The anodic overvoltage of 0.3 V was measured at 0.5 A/cm² current density and the cathodic overvoltage was negligible. The bath's ohmic drop for an anode-cathode distance of 1.3 cm was said to be 0.65 V. The effective bath conductivity was said to be 1.0 S/cm. The current efficiency of the cell was reported to be 50% and it depends on the surface area of the aluminium (*A*) near the anode to the current supplied (*I*). The current efficiency increases with the decrease in (*A/I*) ratio and this can be achieved by consistent removal of aluminium near the anode and if this is implemented accurately, nearly 100% current efficiency can be achieved.

Theodore R. Beck proposed commercial cell design, which uses alumina slurry in the electrolyte, with the conditions mentioned in his patents [64-66]:

- A eutectic NaF – AlF₃ electrolyte with a freezing point of 695 °C with the combination of KF – AlF₃ and LiF – AlF₃ eutectics having a melting temperature of 750°C.
- Alumina slurry content of 5 – 10 wt.% with the particle size of less than 10 µm is added to the electrolyte.
- Vertical copper mono-polar anode and Titanium boride cathode with the minimum anode-cathode distance at around 1.3 cm.
- Continuous removal of aluminium to maintain better current efficiency.
- The horizontal auxiliary oxygen-evolving anode which avoids settling down of alumina particles at the bottom.

Yasinskiy et al. [67], [112] investigated the sedimentation behaviour of alumina suspension based on low-temperature electrolyte system KF-AlF₃-Al₂O₃. The value of maximum packing fraction for smelter grade alumina was estimated to be approximately as high as 0.32 at which the particles have extremely low or zero sedimentation velocity. The main factors determining this value were named to be poly-dispersity (which was calculated to be 0.42), the high porosity and the structural barrier which eliminates sedimentation of the particles.

The physicochemical properties of KF-AlF₃ and NaF-AlF₃ melts are compared in table 4

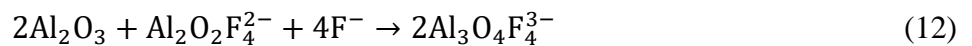
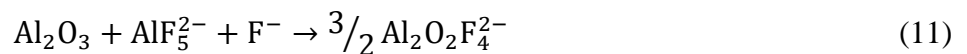
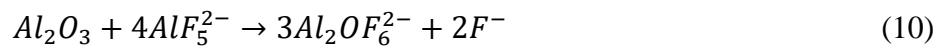
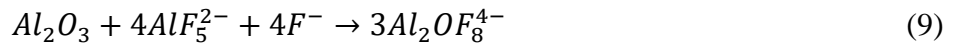
Table 4. Comparison of the basic physicochemical properties of electrolytes for the preparation of alumina suspensions [68-75]

Melt / Property	KF–AlF ₃	NaF–AlF ₃
[MF]/[AlF ₃] ratio, mol mol ⁻¹	1.22	1.3
Liquidus temperature, °C	575	715–720
Al ₂ O ₃ solubility, wt %	4.5 at 700 °C	1.2 at 702 °C
Density at 750°C, kg m ⁻³	1 770	1 910
Kinematic viscosity, m ² s ⁻¹	1.53×10 ⁻⁶	0.72×10 ⁻⁶
Dynamic viscosity, mPa s	2.71	1.38
Surface tension at 750 °C, mN m ⁻¹	138	89
Interfacial tension at 750 °C, mN m ⁻¹	701 ± 10	796 ± 5
Electrical conductivity, Ohm ⁻¹ cm ⁻¹	0.95–1.0 at 700 °C	1.2 at 720 °C

2.4. Sedimentation and dissolution of the alumina in melts

A decrease in the electrolyte temperature increases the corrosion resistance of oxygen-evolving anodes but reduces the alumina solubility and dissolution rate. It makes it more difficult to operate the electrolysis cell. The so-called sludges (undissolved alumina trapped under the liquid aluminium in the cell) are formed, and catastrophic corrosion of the anode may take place.

The dissolution mechanism and its kinetics in sodium cryolite are studied and reported elsewhere [76-79]. Alumina is believed to be dissolved in the commercial electrolyte by one or several of the following mechanisms [80, 81]:



The mechanism should not be changed drastically while replacing the sodium cryolite with the potassium one. However, the kinetics is highly affected by electrolyte composition, temperature and hydrodynamic conditions and is poorly covered in the literature [82].

Suspension electrolytes were proposed to increase corrosion resistance and cathodic metal purity [83-86]. The rheological (sedimentation velocity, maximum packing fraction) and electrochemical behaviour of these suspensions become an important field to study [87-89].

Determining the dissolution rate of alumina in melts has great importance as it influences the total electrolytic process. Extensive research was conducted mostly over the NaF–AlF₃ melts

in studying this process and yet there is a lot of space to fill in understanding it. In the initial stage of alumina addition in the melts, quick dissolution of alumina takes place. Alumina particles dissolve with the formation of activators due to the chemical reaction between the alumina and the melt. Alumina and cryolite crystallization takes place when the cold alumina is added to the hot melt and pores of the alumina particles are penetrated leading to the rapid heat transfer between the melt and particle. Gradually the alumina dissolution stabilizes, and after the saturation point, the equilibrium between the solid and dissolved species is reached [90].

In [99], the influence of the Al_2O_3 concentration added to the NaF- AlF_3 melt and smelter grade alumina (SGA) particle size on the dissolution rate was determined. Findings show that with an increase in the alumina concentration, the dissolution time increases. The larger the particle size, the faster it dissolves; γ -alumina has a higher dissolution rate than α -alumina. It has been stated that α -alumina does not go through phase transformation associated with the release of hydroxyls and low surface area associated with the gas dynamics resulting in the lack of interaction with the melts. Although, the alumina dissolution rate can be improved by preheating it at 600 °C [92]. Different results are obtained with CFD modelling. According to [93], the effective diffusion coefficient of dissolved alumina species increases with the increase in the alumina content in the melt making the dissolution process much easier for small alumina particles. The smaller alumina particle tends to dissolve within 10 s while the larger one takes more time. As mentioned earlier, alumina preheating can speed up the dissolution process. The alumina dissolution rate is independent of alumina content in the melt at alumina concentration $C_A < 3\%$ while the dissolution rate decreases when $C_A > 3\%$ because of the lack of free fluoride solvents in the sodium cryolite melts [80].

It is well known that the bubble generation during the oxidation of carbon eliminates the agglomeration of alumina in the melt [94, 95]. The alumina-feeding rate has importance and plays a key role in avoiding the agglomeration of the alumina particles in the melt when fed [96]. Haverkamp et al. [97] proposed a diffusion model to calculate the dissolution rate of alumina. Dissolution rate R ($\text{g}\cdot\text{s}^{-1}$) mainly depends upon the difference between the alumina saturation concentration (on the surface of the alumina) C_{sat} and current alumina concentration in the media C_A :

$$R = \frac{dc}{dt}V = \frac{D}{\delta}A(C_{A(sat)} - C_A) \quad (13)$$

where D : diffusion coefficient ($\text{m}^2\cdot\text{s}^{-1}$), δ : thickness of the boundary layer (m), t : time (s).

The dissolution rate of alumina in acidic NaF-AlF₃ melts was investigated by Vasyunina et al. [98]. It was determined that with a decrease in the cryolite ratio CR $\left(\frac{\text{Mole \% NaF}}{\text{Mole \% AlF}_3}\right)$ upon 1.8, the dissolution rate of alumina is drastically reduced. It was also found that the minimal dissolution rate ($2 \cdot 10^{-3}$ wt %/s) of alumina required for the possibility of electrolysis in 300 kA cell can be only attained upon CR 1.8. The typical values obtained in the NaF-AlF₃ melts with different CRs were in the range 1-6 g·kg⁻¹·s⁻¹ (20-120 mole·m⁻³·s⁻¹), which are rather high in comparison with the results reported elsewhere [99].

Xiao et al. [100] investigated the solubility of alumina in NaCl-KCl based molten salts. It was found that in the melt with 1:1 wt.% of NaCl-KCl melt, there was no measurable solubility value. With the addition of salts AlF₃ → KF → Na₃AlF₆ → NaF (effect of additive on solubility in order), the solubility was improved to an acceptable limit. The temperature plays a key role in the functioning of the dissolution rate.

Hou et. al [101] conducted a numerical investigation to determine whether mass transfer mechanism or heat transfer mechanism predetermines the alumina dissolution at a given critical diameter of the particle. The studies suggest that particle size under 520 μm is controlled by a mass transfer mechanism while the particle size more than 520 μm is governed by a heat transfer mechanism.

Low-temperature electrolytes were studied in a narrow range of compositions, namely NaF-AlF₃ and KF-AlF₃ with CR=1.22 at 750 and 730 °C by Frazer et al. [82]. It was found that the alumina dissolution rate is higher in KF-based electrolytes. The same was observed by other researchers[107, 108]. It was also stated that alumina dissolution is a mass transfer-controlled process with the diffusion coefficient of dissolved alumina species $D=1.8 - 2.2 \cdot 10^{-6}$ cm²·s⁻¹ at 750 °C, which is about five times lower than the values recorded at 960 °C.

It was reported in [107, 108] that an increase in KF content in the electrolyte from 2 to 7 wt.% leads to a 1.5 times increase in the dissolution rate. The rates recorded at 950 °C were in the range of 0.4 – 0.7 mole·m⁻³·s⁻¹. The dissolution rate depended on alumina concentration in the entire range of concentrations, which is in a contradiction with other results obtained with visual observation in a see-through cell [80]. The appearance of kinetic limitations at low alumina concentrations is a subject of further studies.

An increase in alumina concentration in the electrolyte from 0.5 to 3 wt.% at 950 °C results in a twofold drop in the dissolution rate. Even a small increase in temperature (up to 975 °C)

leads to the threefold increase in the dissolution rate. It was also reported that it rises with CR of the electrolyte [107].

Isaeva et al. [111] studied the effects of alumina properties on the dissolution rate in commercial electrolytes. The reported values were as high as 0.05-0.075 g·kg⁻¹·s⁻¹ (1.0-1.5 mole·m⁻³·s⁻¹).

The potentiometry studies of mechanically activated alumina were performed on the high-temperature commercial electrolyte by Yushkova et al. [105]. It was found that mechanical activation leads to the 1.5 times higher dissolution rates under the same conditions. The initial rates were 0.014 and 0.022 g·kg⁻¹·s⁻¹ (0.28 and 0.44 mole·m⁻³·s⁻¹) at 950 °C for non-activated and activated aluminas respectively, which is nonetheless lower than reported by other researchers [108]. The difference in dissolution rates obtained by different researchers shows that various methods lead to specific changes in the conditions. Visual observations can outline the general dependencies but the accurate measurement of the absolute values can be rather difficult as alumina particles may become transparent before they get dissolved. Despite the visual methods are widely used [80, 116-122] they perform better while used as additional with respect to instrumental electrochemical measurements.

The sedimentation behaviour of smelter grade alumina (SGA) suspension in KF-AlF₃ melts was studied previously [112] at 700 °C and high alumina volume fractions (0.24-0.32). The Reynolds numbers (Re) for alumina sedimentation were in the range of (7.88·10⁻⁷)-(7.56·10⁻³) that indicated the Stokesian regime. The Re values were significantly lower than those calculated in [109] for both agglomerated and non-agglomerated alumina particles settling, which were in the range of 3.4-2545.8 for the size range from 40 µm (non-agglomerated) to 15 mm (agglomerated).

In this chapter, the literature review has highlighted the main outcomes of the previous investigations carried out and are as follows:

- In section **2.1**, the information related to the inert anodes with different types namely ceramics, metals and cermets along with novel type anodes is mentioned.
- In section **2.2**, brief details related to the W electrode in low-temperature melts was discussed.
- In section **2.3**, the characteristics of low-temperature melts and suspension which can be used for the aluminium electrolysis is discussed.
- In section **2.4**, the previous finding related to the solubility of alumina in cryolite melts are described.

In the upcoming chapters, the investigation will be conducted on unknown aspects related to the above-mentioned sections will be conducted and discussed thoroughly.

3. Electrode process in KF-AlF₃-Al₂O₃ melts

In this chapter, the anodic behaviour of Cu-Al based electrode in low temperature melts at different conditions like alumina volume fraction, CR value, the temperature was investigated along with the cathode process on W electrode in low temperature melts using cyclic voltammetry and chronopotentiometry techniques.

3.1. Experimental

Material preparation

The anode alloys with three compositions of Cu-9Al-5Fe (A1), Cu-10Al (A2), and Cu-10Al-1.7Be (A3) (in wt. %) were prepared in a vacuum melting furnace at 1050 °C. The materials used for the preparation had a purity of Cu (99.95 %), Al (99.999%), Fe (99.99%) and Be (99.95%) and the anodes have minute impurities of about 0.05%. The specimens were cut in a cylindrical shape with dimension ϕ 15mm \times 50 mm. The specimens were treated with degreasing agents (acetone and ethanol) and then dried in the air before the usage. A hole with ϕ 2.5mm was drilled and threading was made to assemble current lead (steel rod) with the anode. The unused anodic part and the steel current lead were protected with a BN tube insulator. The W electrode used to examine the cathode process is supplied by P.O. Wolfram. The composition of the electrode is W > 99.95, Al < 0.002, Fe < 0.005, Si \approx 0.003, Mo \approx 0.03, Ca \approx 0.005.

Electrolytes with CR between 1.2 and 1.5 were synthesized. Firstly, a crystalline KF was heated in the vertical furnace to remove the water present in the salt at 400 °C for 4 hours. While synthesizing the electrolyte, the AlF₃ salt was placed at the bottom of the crucible and the KF salt was set at the top as AlF₃ tends to sublime quickly at 800 °C and higher. The synthesis process was carried out for 3 hours. The melt was mixed well and a portion of alumina was added corresponding to its saturation point in the melt (5 wt.%) with continuous

stirring. The temperature during the preparation of melt was monitored throughout the process with the help of a k-thermocouple protected with BN sleeve, which was immersed into the electrolyte. The melt was transferred to a container where it was left to solidification. The solidified melt was then crushed and used accordingly. All the chemicals used were analytical grade and alumina used has an average particle size less than $5\mu\text{m}$ as shown in figure 10.

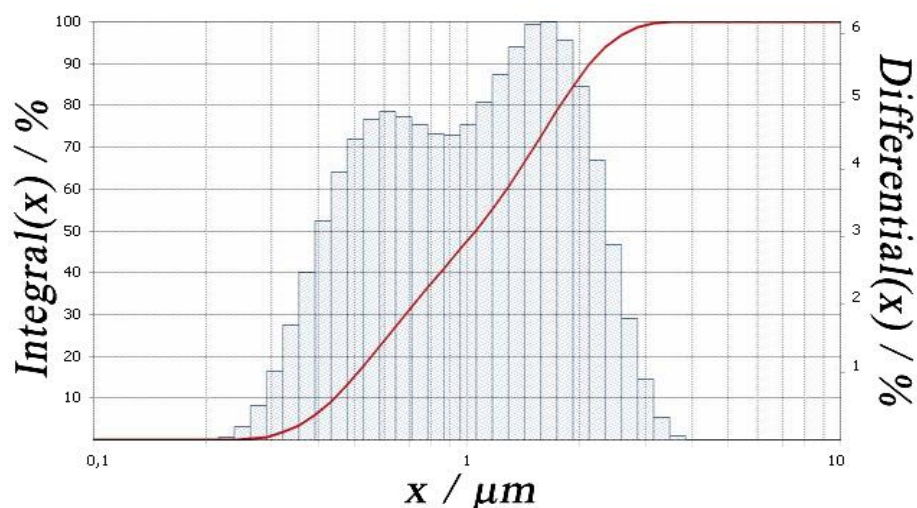


Figure 10. The particle size distribution of Al₂O₃

Experimental method

The three-electrode cell as shown in figure 11 was used to perform the experiments. High purity graphite crucible was used to contain KF-AlF₃-Al₂O₃ (5wt. %) melt. The crucible also acted as a counter electrode. The Al/AlF₃ reference electrode was used which was connected to the measuring device using a tungsten rod. The reference electrode had a porous BN tube containing the liquid aluminium and KF-AlF₃ melt.

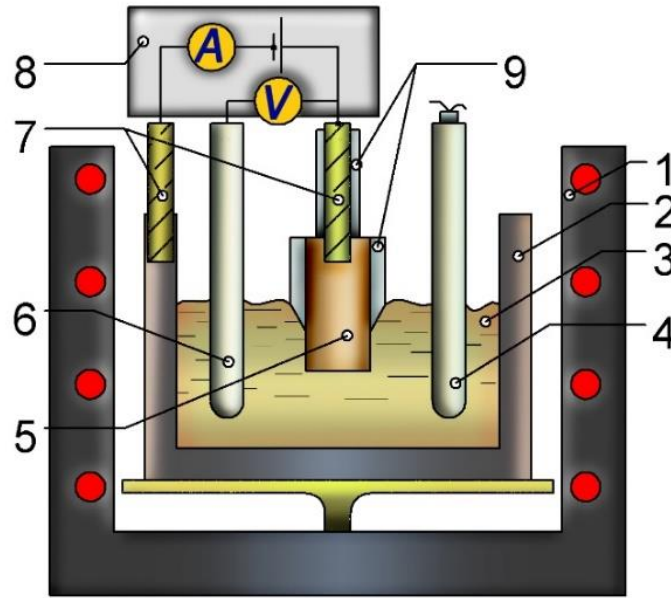


Figure 11. Experimental setup: 1 - Furnace; 2 - graphite crucible $h = 110$ mm, $d_{\text{int}} = 76$ mm, $d_{\text{ext}} = 92$ mm; 3 – electrolyte/suspension $\text{KF-AlF}_3\text{-Al}_2\text{O}_3$; 4 - thermocouple; 5 - anode sampled = 15 mm, $h = 10$ mm; 6 - reference electrode (Al/AlF_3); 7 - steel current leads, 8 – potentiostat, 9 – BN shields

Autolab PGSTAT302n potentiostat equipped with a 20A booster and controlled by NOVA 2.1.2 software was used to carry out the electrolysis. Electrolysis was conducted using Chrono potentiometric method according to which the stable potential was obtained and a stable oxide layer was formed on the anodic surface. Stationary polarization was performed for 0.005 to 1.5 A/cm^2 current densities where the recording was made with $30 \mu\text{s}$ of current interruption time after a 120s current passage to determine the ohmic voltage drop (IR). Cyclic voltammetry was performed at 0.05 V/s scan rate to examine the possible anodic reactions. The anodic overvoltage was calculated according to the equation:

$$\eta_a + \eta_c = E_i - E_r - IR \quad (14)$$

where η_a : activation overvoltage, η_c : concentration overvoltage, E_i : the potential difference between the anode under current and the reference electrode, E_r : anodic reversible potential relative to the reference electrode, I : current, R : resistance. The activation and concentration overvoltages were not separated, and the sum was treated as total anodic overvoltage.

Note: The experimental method mentioned in this section is used to examine the anodic process of Cu-Al based alloys and cathode process on the W electrode.

Experimental techniques

Chronopotentiometry

In chronopotentiometry, a constant current is set to the cell for a specific time period. The applied current is stepped instantaneously from zero to a constant value, where the overall cell reaction is fixed and the potential of the working electrode is recorded as a function of time with respect to a reference electrode.

Consider a solution where only O is initially present. The working electrode is initially with current 0A where no reduction of O occurs. At $t=0$, the current is instantaneously changed from zero to a finite value. At transaction time $t= \tau$, the surface concentration of O drops to zero which results in the reduction of O.



The potential of the working electrode is related to the surface concentration of O and R by the Nernst equation:

$$E = E^o + \frac{RT}{nF} \ln \frac{c_O^*}{c_R^*} \quad (16)$$

Where c_O^* and c_R^* are the bulk concentration.

Current interrupt technique can be used and electrode overpotential can be calculated by substrating IR . Following figure 12 illustrated the current interrupt technique

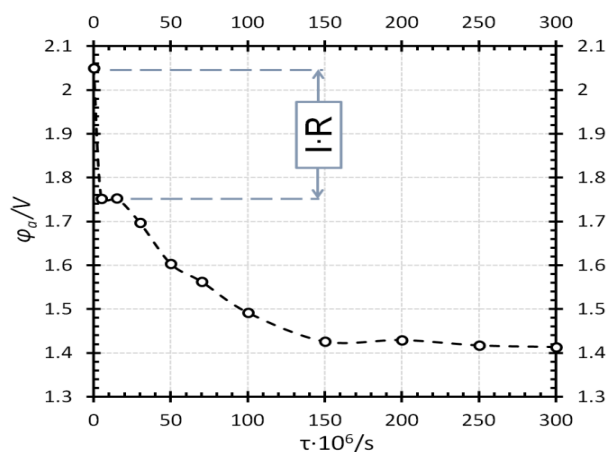


Figure 12. An example of current interrupt averaged measure

Overvoltage - the value of the electrode potential displacement from its equilibrium:

$$\eta = E - E_r \quad (17)$$

where E: the electrode potential under the current, E_r : the reversible electrode potential (without the current).

Cyclic voltammetry

Cyclic voltammetry is a versatile and more common technique used to investigate the anode and cathode process on an electrode in a system. In CV, the potential is reversed and cycled between two set potentials at a constant sweep rate ($V s^{-1}$). The current response occurs at an array of potentials at which the over-potential is increasing, and in the absence of other charge transfer reactions, the current reaches to peak then start to decrease until it flattens out. A typical cyclic voltammogram for a reversible system is shown in figure 13

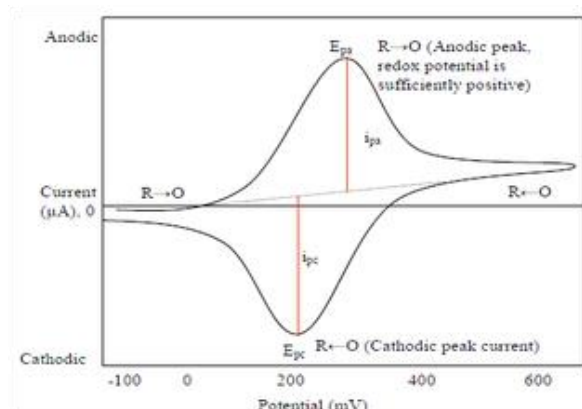


Figure 13. Typical cyclic voltammogram showing the cathode and anode current peaks [113]

The main advantage of CV is that it shows the reduction reaction ($O + ne^- = R$) and reoxidation reaction ($R = O + ne^-$) in one cycle unlike linear sweep voltammetry. With the help of CV, it can be defined if a process is reversible, irreversible or quasi-reversible.

3.2. Anodic behaviour of aluminium bronze electrode

Although metallic anode like Ni-Fe based and Cu-Al based are identified as a promising candidate to be an inert anode, much of the information related to the anode process in low-temperature melts with suspensions has not been mentioned in the open literature. The use of suspension melts have not been found until now and this study aims to give an understanding of the behaviour of Cu-Al based anodes in suspensions with varying volume fractions. It is to hope that the information proved in this chapter can be a valuable source to the future advancements of inert anode technology.

The current chapter showcases the study of anode process on several Cu-Al-based alloys in melts and suspensions by the stationary galvanostatic polarization and cyclic voltammetry. The criteria for selecting the aluminium bronze were:

- the high electrical conductivity of the alloy and the copper aluminates, which are formed during oxidation by oxygen and electrochemically in melts contained oxygen ions;

- the low solubility of copper aluminates in fluoride melts saturated with oxygen ions;
- the high melting point of the alloy (near 1050 °C), allowing significant proper electrolysis overheating (figure 14).

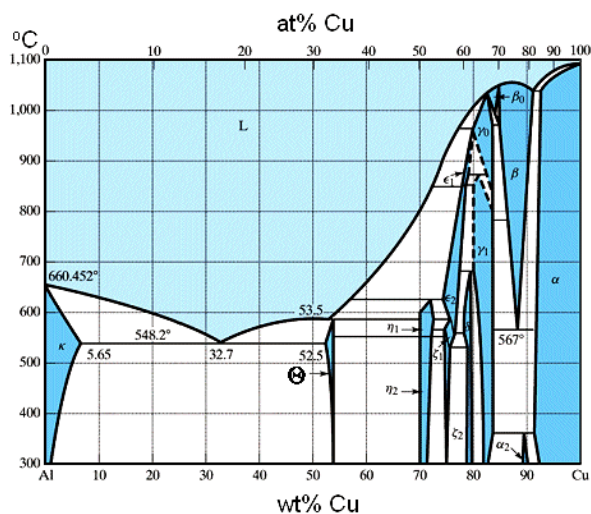


Figure 14. Phase diagram of Cu-Al [114]

3.2.1. Effect of anode composition

The studies were carried out on the anodes of three different compositions: A1, A2, and A3 in melts and suspensions based on $\text{KF-AlF}_3\text{-Al}_2\text{O}_3$ with CR 1.3 at 1023 K (750 °C). Reactions shown in table 5 are expected to appear during the oxidation of these anode alloys (the change in the thermodynamic potentials is given for $T = 1023\text{ K}$, the standard electrode potentials are presented relative to the Al/Al^{3+} reference electrode, the calculations were carried out in the **HSC Chemistry v.9.6.1 software**).

Table 5. Possible reactions, electrode potentials and changes in thermodynamic potentials at 750 °C per 1 mol of Al

Reaction	ΔG_{1023K}^0 , kJ/mol	ΔH_{1023K}^0 , kJ/mol	ΔS_{1023K}^0 , kJ/mol·K	E^0 , V
$\text{Al}_2\text{O}_3(\text{dis}) + 3\text{Cu}_{(s)} \xrightarrow{6F} 2\text{Al}_{(l)} + 3\text{CuO}_{(s)}$	580.21	621.63	40.48	2.00
$\text{Al}_2\text{O}_3(\text{dis}) + 6\text{Cu}_{(s)} \xrightarrow{6F} 2\text{Al}_{(l)} + 3\text{Cu}_2\text{O}_{(s)}$	535.79	595.54	58.40	1.85
$2\text{Al}_2\text{O}_3(\text{dis}) + 1.5\text{Cu}_{(s)} \xrightarrow{3F} 1.5\text{CuAl}_2\text{O}_4(\text{s}) + \text{Al}_{(l)}$	393.77	453.57	58.44	1.36
$2\text{Al}_2\text{O}_3(\text{dis}) + 3\text{Cu}_{(s)} \xrightarrow{3F} 1.5\text{Cu}_2\text{Al}_2\text{O}_4(\text{s}) + \text{Al}_{(l)}$	513.90	58.44	44.19	1.78
$\text{Al}_2\text{O}_3(\text{dis}) + 3\text{Fe}_{(s)} \xrightarrow{6F} 2\text{Al}_{(l)} + 3\text{FeO}_{(s)}$	380.32	449.40	67.52	1.31

$Al_2O_{3(dis)} + 2Fe_{(s)} \xrightarrow{6F} 2Al_{(l)} + Fe_2O_{3(s)}$	399.87	443.17	42.31	1.38
$2Al_2O_{3(dis)} + 4.5Fe_{(s)} \xrightarrow{12F} 4Al_{(l)} + 1.5Fe_3O_{4(s)}$	383.10	439.09	54.73	1.32
$2Al_2O_{3(dis)} + 1.5Fe_{(s)} \xrightarrow{3F} Al_{(l)} + 1.5FeAl_2O_{4(s)}$	309.00	364.41	54.17	1.07
$Al_2O_{3(dis)} + Fe_{(s)} + 3Cu_{(s)} \xrightarrow{6F} 2Al_{(l)} + Cu_2O_{(s)} + CuFeO_{2(s)}$	462.15	507.25	44.08	1.60
$Al_2O_{3(dis)} + 3Be_{(s)} \xrightarrow{6F} 3BeO_{(s)} + 2Al_{(l)}$	-86.55	-65.05	21.02	-0.30
$2Al_2O_{3(dis)} + 6Be_{(s)} \xrightarrow{12F} Be_6O_{6(g)} + 4Al_{(l)}$	100.09	177.44	75.60	0.35
$2Al_2O_{3(dis)} + 1.5Be_{(s)} \xrightarrow{3F} 1.5BeAl_2O_{4(s)} + Al_{(l)}$	-113.84	-89.31	23.98	-0.39
$5Al_2O_{3(dis)} + 1.5Be_{(s)} \xrightarrow{3F} 1.5BeAl_6O_{10(s)} + Al_{(l)}$	-84.55	-47.29	36.42	-0.29

The reactions shown in table 5. represent the sum of the oxidation-reduction electrode half-reactions, and changes in the corresponding Gibbs energies, which are known to be associated with the potential difference (standard EMF) by the ratio:

$$E^0 = -\frac{\Delta G^0}{z \cdot F} \quad (18)$$

where z : number of electrons, $F = 96485$ [C/mol]: Faraday constant. Calculated standard potentials are placed on the scale in figure 15.

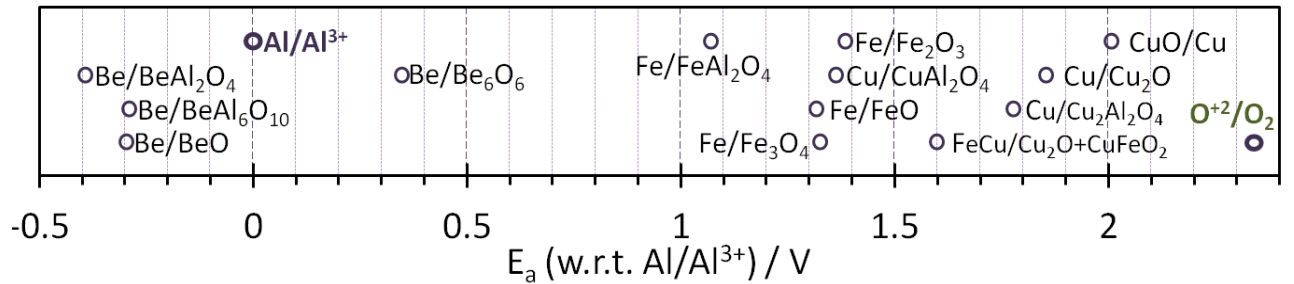


Figure 15. Scale of standard equilibrium electrode potentials for possible anodic reactions on the alloys studied

The standard electrode potential of the oxygen electrode at 750 °C is 2.34 V. Oxidation of the anode metals significantly shifts the anode potential to the region of more negative values (relative to the oxygen electrode). According to the thermodynamic analysis, the most negative potential is expected at the anode A3. The formation of copper aluminates is likely on the surface of all the anodes. At the anode A1 copper ferrite and iron aluminate are expected (with an equilibrium shift towards the formation of $FeAl_2O_4$), because the formation of complex oxides occurs at more negative electrode potentials in comparison with binary

compounds. At the anode A3, the formation of beryllium and copper aluminates and oxides is expected.

In this section, the polarization characteristic of the anodes A1, A2 and A3 are the subject of an electrochemical study by stationary and non-stationary techniques. The effect of alumina volume fraction ϕ on the electrochemical properties (open circuit potential, current-potential curves) is also of primary interest. Cu-Al-based alloys anodic potentials measurements are necessary to clarify the oxidation patterns and current-voltage characteristics. Understanding of the suspension properties influence on anode electrochemical behaviour can ultimately contribute to the development of an energy-efficient environmentally friendly technology for aluminium production.

The electrodes were polarized for 1.5 – 2 hours at a current density $i_a = 0.4 \text{ A/cm}^2$ ($I=3.7 \text{ A}$) before performing chronopotentiometry (for recording the stationary potential-current curves). The change in voltage during the electrolysis in melt and suspension with the volume fraction of solid particles $\phi=0.12$ is presented in figure 16.

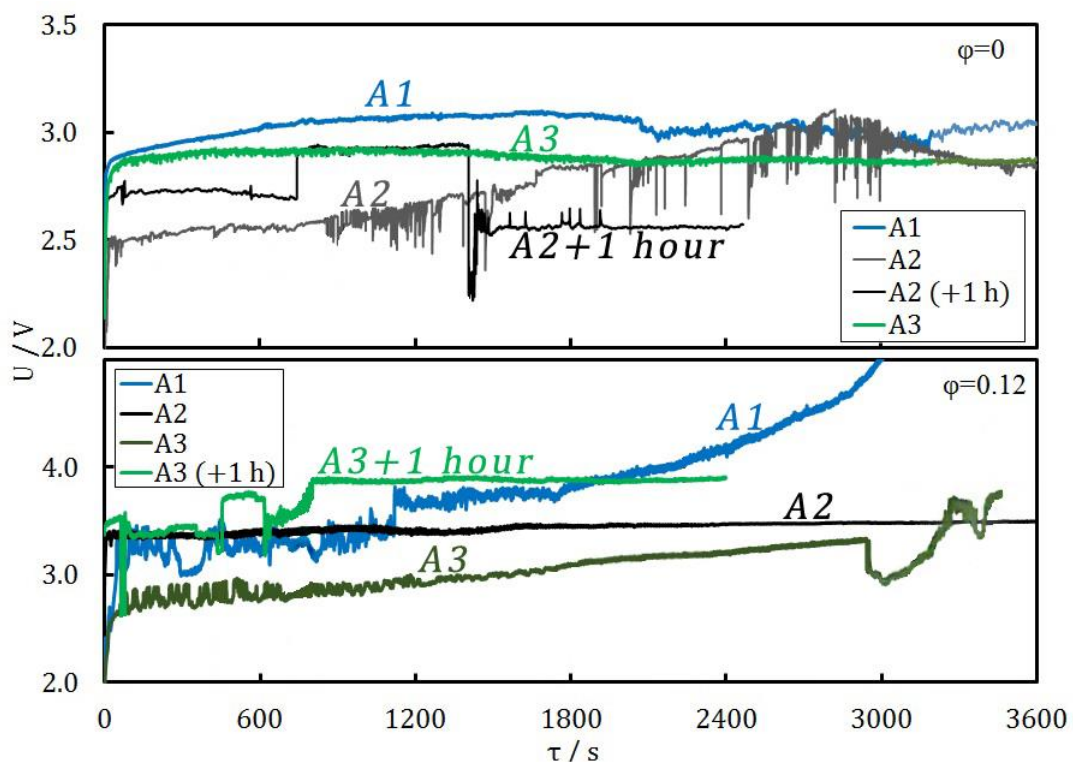


Figure 16. Stationary polarization of the electrodes in melts ($\phi=0$) and suspensions ($\phi=0.12$) in CR 1.3

3.2.1.1. Stationary state polarization

Polarization in melts ($\varphi=0$) occurred with cell voltage U between 2.5 and 3.1 V for all the anode composition. The voltage was changed due to the oxide layer formation and the changes in its structure and composition. In the case of anode A2, the high oscillations were observed. In melts with suspension ($\varphi = 0.12$), the voltage increases for samples A1 and A2 were ranging in 3.4...3.5 V. The initial voltage for A3 sample was 2.6 V and gradually increased to 3.9...4.0 V in 1.5 hours. The passivation of anode A1 was observed after 1800 s.

The stationary galvanostatic polarization curves (figure 17) were recorded in melts ($\varphi=0$) and suspensions with $\varphi=0.12$ and 0.15. The time to reach the quasi-stationary state was about 100 seconds.

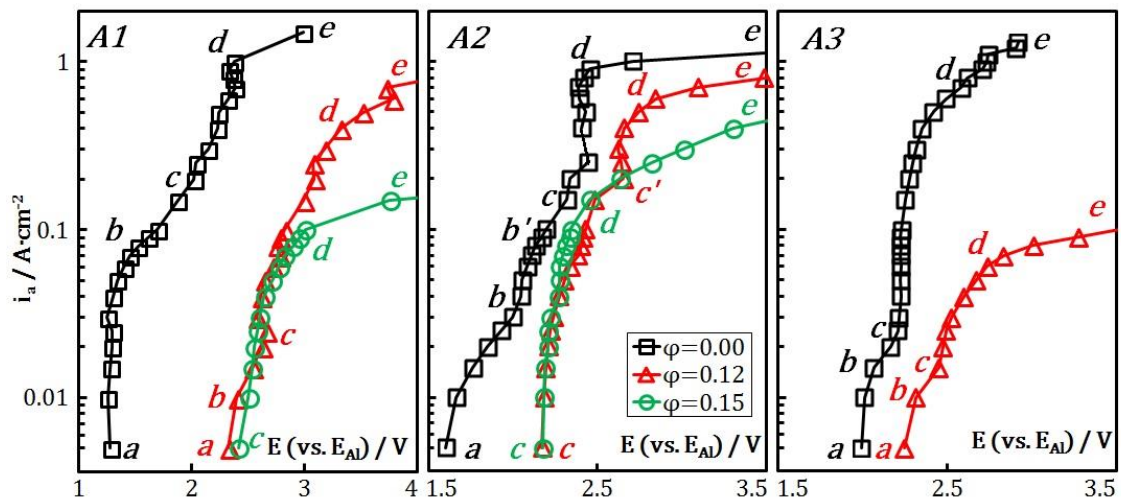


Figure 17. Stationary polarization curves for the anodic process in the melt and suspensions on alloys of three different compositions (CR 1.3)

Several parts on the curve have been observed in the pre-oxygen and oxygen regions (figure 17):

- metal oxidation (**ab**) $xMe + yO^{2-} \rightleftharpoons Me_xO_y + 2ye^-$ or $Me + \rightleftharpoons Me^{z+} + ze^-$;
- apparent metal oxidation limiting current section (**bc**) caused by the low active surface area available for metal oxidation (low Me concentration at the interface);
- oxygen ions oxidation (**cd**) $2O^{2-} \rightleftharpoons O_2 + 4e^-$;
- apparent oxygen ions oxidation limiting current section (**de**) caused by low O^{2-} concentration and screening of the anode surface by bubbles and particles.

The pre-oxygen and oxygen regions are divided by (**c**) at potentials 2.1...2.3 in melts and at potentials 2.3...2.5 in suspensions. Polarization in the melt at low current densities occurred

at potentials 1.3...2.0 V. At anode A1, a potential close to that of the FeAl/FeAl₂O₄, Fe/Fe₃O₄, and CuAl/CuAl₂O₄ electrodes under standard conditions was observed. Moreover, the anode was oxidized without significant diffusion and kinetic difficulties (*ab*) up to a current density of about 0.1 A/cm². With increasing current density, the potential started to shift towards the oxygen electrode potential (\approx 2.3 V). As for the anode A3, polarization at low current densities (*abc*) proceeded at potentials of about 2 V. Such potentials are close to the standard potential of the Cu/CuO electrode. Oxidation of the anode A3 occurred without significant overvoltages up to 0.1 – 0.2 A/cm². The role of beryllium in establishing such potential is not clear.

Alloy A1 has the highest current density at potentials lower than necessary for oxygen evolution, which is associated with high iron content in the alloy, which transforms into readily soluble oxides. High current densities in the region of the pre-oxygen potential indicate significant dissolution rates of anode oxidation products and a high partial current density of the anode oxidation in the oxygen potential region. Anode A2 has the lowest current density of the onset of oxygen evolution (*c*), which indicates a low dissolution rate or the solubility of its oxidation products.

After the introduction of alumina particles into the melt, the potentials shift toward values corresponding to oxygen evolution even at low current densities, which may be related to diffusion difficulties in removing the products of dissolution of the oxide layer into the suspension bulk. At a potential \approx 3 V in a suspension with $\varphi = 0.12$, anodes A1 and A3 have similar current densities (0.1 and 0.07 A·cm⁻² respectively) while much higher value (0.5 A·cm⁻²) is observed on the anode A2. With an increase in φ up to 0.15, a decrease in the apparent limiting current densities (*de*) is observed for anodes A1 and A2. A drastic increase in resistance due to the passivation was observed on the anode A3 at $\varphi=0.15$ and therefore not possible to complete the recording of the polarization curve. The increase in current density was observed on anode A2 (*c'd*) at 2.6 V. In general, from the stationary curves (figure 17), we can conclude that the A2 anode is more promising compared to A1 and A3. The following facts favour this conclusion:

- a low current density of the anode oxidation in the pre-oxygen region (*abc*) of the potentials in the melt;
- a low partial current density of the anode oxidation in the oxygen region (*cde*) of the potentials in the melt;
- high apparent limiting current density (*de*) in suspension.

3.2.1.2. Cyclic voltammetry

In the non-stationary study at a low sweep rate of 0.05 V/s (figure 18), the anode A1 has the highest current density, which was unexpected as the alloy of this composition is more prone to passivation due to the formation of dielectric oxides. The presence of significant transport difficulties that may be created by the presence of a concentrated suspension. The plateau (figure 18a – 1) is observed at potentials 1.9 – 2.1 V and a current density of 0.10 – 0.15 A·cm⁻², which is associated with the diffusion-controlled metal oxidation. The high current density confirms the possibility of the anode oxidation products dissolution. The oxygen evolution current (figure 18a – 2) was recorded after the plateau. The open-circuit potential during the sweep is close to the potential corresponding to the Cu/Cu₂O and CuAl/Cu₂Al₂O₄ electrode potentials (1.85 V and 1.78 V, respectively). The same is true for the anode A2 (figure 18b), however, no peaks and limiting oxidation currents are observed on the voltammograms. The open-circuit potential during the sweep for anode A3 is close to the standard equilibrium potential of the Cu/CuO electrode, and a peak corresponding to the oxidation of the anode is observed on the curve. The oscillations (figure 18c – 3) are associated with bubble phenomena.

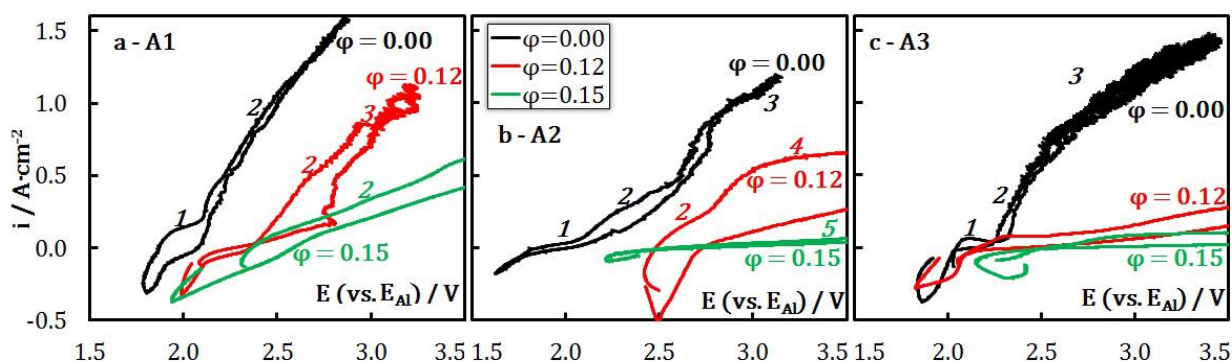


Figure 18. Cyclic voltammograms for anodic polarization in melts and in suspensions with $\phi = 0.12$ and $\phi = 0.15$ on alloys A1 (a), A2 (b) and A3 (c) at $v = 0.05$ V/s (CR 1.3)

In suspensions with $\phi = 0.12$, a gradual increase in resistance (4) on the A2 anode (figure 18) was observed at i_a near 0.5 - 0.6 A/cm² and E of about 2.9 - 3.1 V. Anode A3 is partially passivated at lower i_a and E_a .

With an increase in ϕ from 0.12 to 0.15, passivation (5) of the anodes A2 and A3 is observed, while the anode A1 continues to pass current with a high density (about 1 A/cm²) even with a strong potential bias towards positive values. A comparison of non-stationary and stationary polarization curve patterns allows us to conclude that the increase in the resistance on the A1 anode occurs under stationary conditions with long-term polarization, and the reason is due to

the accumulation of non-conductive anode oxidation products in the anode layer saturated with these products.

The resistance increase on the anodes A2 and A3 is probably caused by an increase in the oxide layer thickness and the bubbles accumulation in the anode space due to the high hydrodynamic resistance to their movement, related to high apparent viscosity. Under the same conditions, the A1 anode has a larger partial oxidation current, which makes the specific gas evolution rate lower, and the active surface area is larger than on the A2 and A3 anodes.

The results of non-stationary polarization indicate that φ should be no more than 0.12, which is confirmed for particles size less than 5 μm . With an increase in φ , diffusion difficulties in the anode layer increase, which would lead to a drastic increase in the resistance.

From both stationary and non-stationary studies it can be observed that with an increase in φ the anodic potential (and oxygen evolution potential) shifts towards more positive values despite that electrochemical pre-oxidation were performed on all the samples for 1 – 1.5 hours. This observation deserves further investigation and will be discussed in a separate publication.

3.2.1.3.XRD studies

After the polarization of three anodes in melts ($\varphi=0$) and suspension ($\varphi=0.15$), the oxide layer formed on the anode samples were studied by XRD technique. The initial XRD graphs are presented in figure **19**. The oxide layers phase compositions are shown in table **6**. The products of crystallization of the electrolyte crystallization are not displayed.

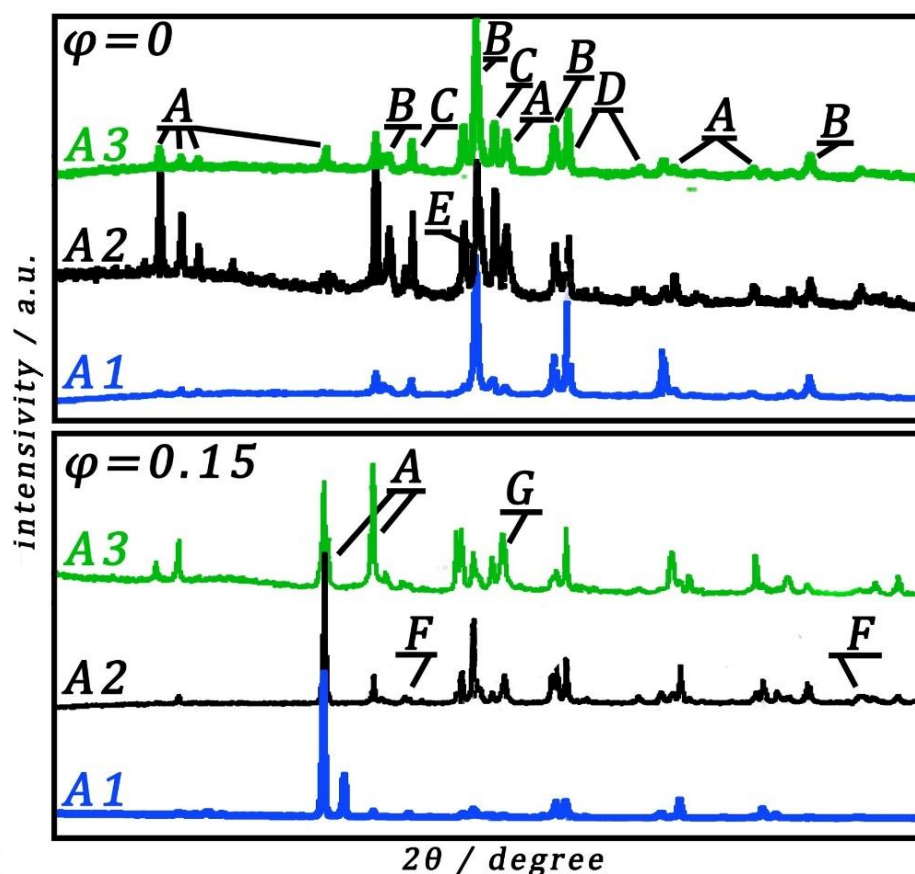


Figure 19. X-ray powder pattern: A) electrolyte phases, B) Cu_2O , C) CuAlO_2 , D) Cu, E) CuAl_2O_4 , F) CuO , G) Al_2O_3

Table 6. The phase composition (wt. %) of the samples of the oxide layer on the anodes after polarization in melt and the suspension $1.3\text{KF-AlF}_3\text{-Al}_2\text{O}_3$ at $750\text{ }^\circ\text{C}$

Anode	φ	CuO	Cu_2O	CuAlO_2	CuAl_2O_4
A1	0.00	0	54.91	45.09	0
	0.15	0	83.08	16.92	0
A2	0.00	0	30.34	53.63	16.03
	0.15	31.16	42.84	11.77	14.22
A3	0.00	0	57.38	42.62	0
	0.15	0	62.57	37.43	0

The oxide layers of the anodes with different compositions vary greatly. In all samples, significant amounts of CuAlO_2 and Cu_2O compounds are present. Radiographs have shown no peaks corresponding to many expected compounds: copper ferrites, aluminates and iron oxides at anode A1, aluminates and beryllium oxides at anode A3. It is assumed that the contents of these compounds are below the detection limit or their volume distribution is uneven. The thermodynamic stability at $750\text{ }^\circ\text{C}$ decreases in the order $\text{CuAl}_2\text{O}_4 - \text{CuAlO}_2 -$

$\text{Cu}_2\text{O} - \text{CuO}$. The most stable compound CuAl_2O_4 was found only in samples of the A2 anode. Peaks of the relatively stable compound $\text{Cu}_2\text{Al}_2\text{O}_4$ were not detected in X-ray diffraction patterns.

It is observed, that the transition from saturated melt to suspension naturally leads to a decrease in the fraction of copper aluminates and an increase in the fraction of monovalent copper in the oxide layer. CuO and CuAl_2O_4 compounds were found only in the oxide layers of A2 anode. The current-voltage characteristics in suspension (high open-circuit potentials and low current densities in the pre-oxygen potential region) indicate a non-electrochemical mechanism of the CuAl_2O_4 formation by reactions:



After polarization during 4–5 hours, the samples were coated with a dense oxide layer (≈ 0.5 -1 mm). Visible cracks and traces of deep corrosion were not observed (figure 20)



Figure 20. Anodes after 5 hours electrolysis in melts and suspensions.

The electrode process of A2 anode with composition Cu-10Al will be further studied in different electrolytes, suspension compositions, temperatures and to study in more detail the dependence of the limiting currents, overvoltage, and structure of the formed oxide layer on the volume fraction of the dispersed phase in the suspension. A2 was further considered for

the study as the anode possesses higher limiting currents in melts and suspensions compared to A1 and A3

Also, the advantage of the anode A2 is confirmed by the phase composition of the oxide layer:

- a high fraction of relatively stable copper aluminate CuAl_2O_4 in the oxide layer structure;
- the appearance of copper monoxide in the oxide layer structure during the transition from melts to suspensions.

3.2.2. Effect of temperature and CR

To characterize the effect of temperature and CR on the anodic behaviour of Cu – 10Al alloy both stationary and non-stationary polarization techniques were applied.

3.2.2.1. Cyclic voltammetry

Cyclic voltammetry was performed on anodes at 700 and 800 °C in melts saturated with alumina at CR = 1.2 – 1.5. Voltammograms were recorded to observe the response of anode with the change in potential at 0.05 V/s scan rate are illustrated in figure 21.

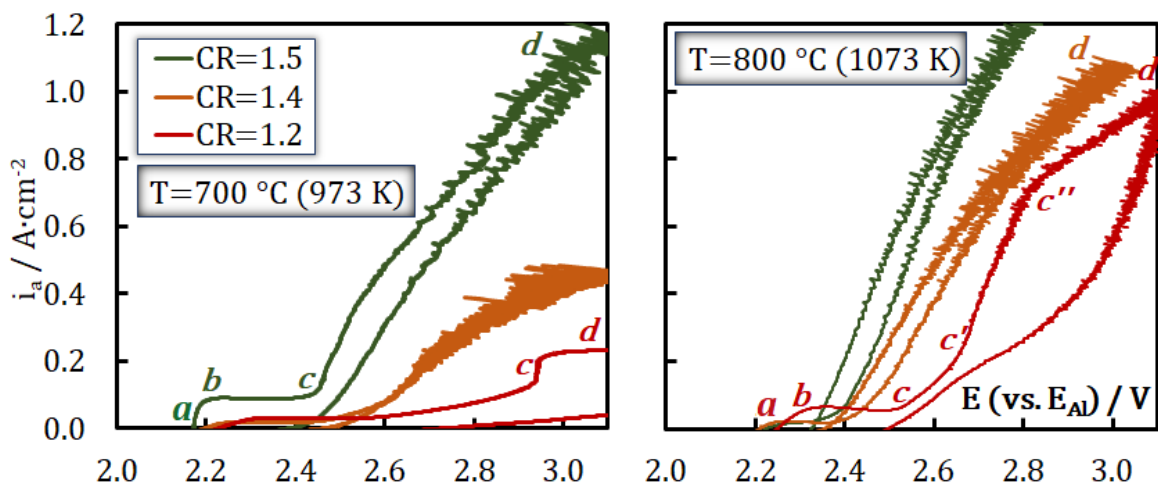


Figure 21. Cyclic voltammograms for the anode in melts with different CR (1.2-1.5) at 700 and 800 °C

Several regions can be distinguished on the curves. The *ab* region between 2.1 and 2.3 V is where the metal oxidation takes place. After that, a region *bc* with a plateau or a slight decrease in current with the potential shift toward more positive values can be observed. The trans-passivation process of the anode takes place in the region *cd* where the oxygen starts to

evolve. The current density fluctuation at potentials after 2.5 V is due to the evolution of the bubble on the anode surface leading to the continuous change in the active anode surface and the inter-polar resistance. No passivation of the anode was observed at 800 °C for CR = 1.4 and CR = 1.5. With the decrease in the CR, reduction of anodic current density at the particular anodic potentials (in oxygen region *cd*) can be seen.

For melts with CR 1.2 at 700 °C, current density remains low, indicating the passivation of the anode from the beginning of the process. After an increase in the temperature to 800 °C the shape of the curve in the oxygen region had changed. The region *c'c''* appeared where the $\partial i/\partial E$ value was higher than that of *cc'* and *c''d* regions. The reason might be associated with the change in resistance during the sweep due to passivation and trans-passivation phenomena. High current densities were achieved while using melts with CR =1.5. This can be related to higher alumina solubility in the melt at higher CR.

The reversible potentials and the stationary potentials at $i=0.4 \text{ A cm}^{-2}$ obtained through the galvanostatic process for $1.2 \leq \text{CR} \leq 1.5$ are illustrated in Fig. 22. An increase in the CR results in the more negative of the anodic potential and evolution of oxygen at low current densities. The reason is that an increase in AlF_3 concentration in the melts leads to the formation of oxyfluoroaluminates like AlOF_x^{1-x} , $\text{Al}_2\text{OF}_x^{4-x}$, $\text{Al}_2\text{O}_2\text{F}_x^{2-x}$, Al_4OF_8 , $\text{Al}_4\text{OF}_{10}$ at higher rates leading to the difficulties in the ions transport between the anode and the cathode.

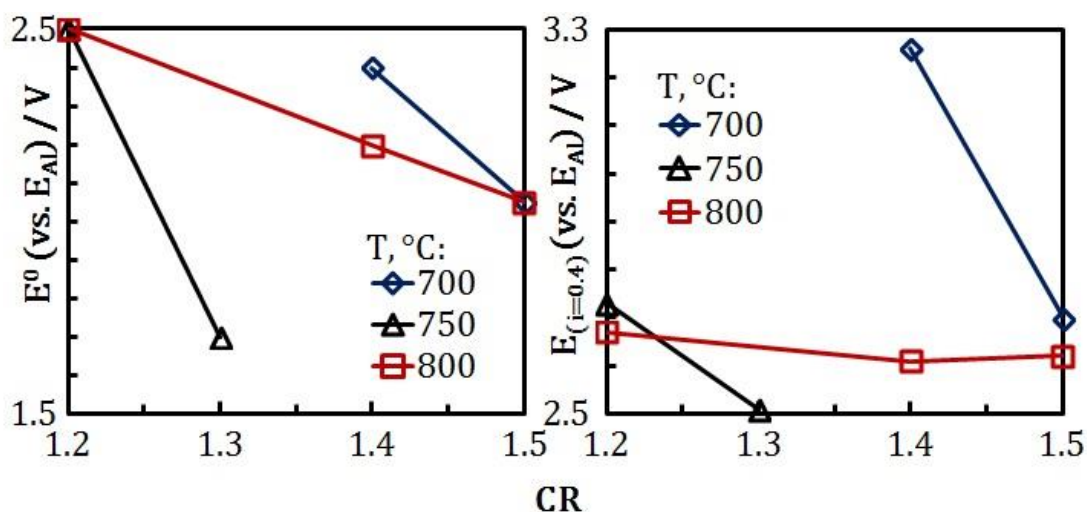


Figure 22. Dependence between reversible potential (left) and stationary potential at 0.4 A/cm² (right) in melts at 700, 750 and 800 °C vs. CR

In the case of melts with CR = 1.5, the effect of temperature on the anodic potential was not observed until the oxygen evolution potential (2.34V). The limiting current densities were observed at high potentials (3.2-4.2 V) for CR = 1.2 at all the temperatures. In the case of

CR= 1.4, limiting currents were in the region from the potential 2.9V. At CR = 1.5, the limiting current region is between the potentials (3.4 -4.2V) in melts at 700 °C and no limiting currents were observed at 800 °C. In the melts with CR= 1.4, drastic variation in current density w.r.t anodic potential was seen with the change in temperature.

In terms of the cathodic process, the lower CR is preferable due to higher limiting currents of aluminium reduction, so the optimal CR value can be between 1.3 and 1.4.

3.2.2.2. Stationary polarisation curves

Stationary galvanostatic polarization of Cu-Al anode was performed over several melts with different cryolite ratios from 1.2 to 1.5 at 700, 750 and 800 °C to study the kinetic parameters of oxygen evolution. The understanding of the current-potential dependences is required for an advance in the search for the corrosion-resistant anode that can be used as an oxygen-evolving electrode in fluoride melts. The anodic current density i_a and the anodic potential E_a (vs. Al reference electrode) were recorded during the experiment. The obtained polarization curves are presented in figure 23.

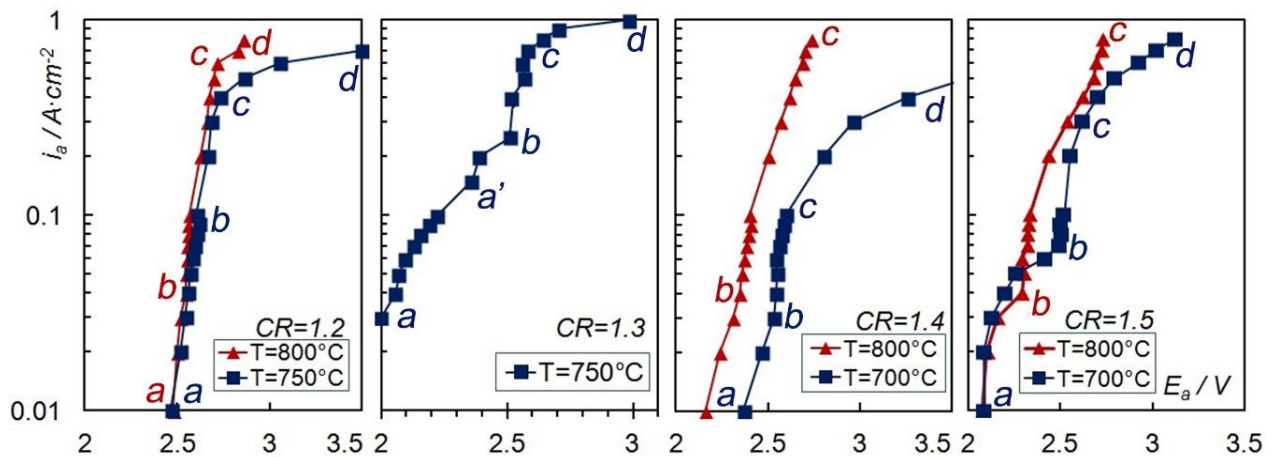


Figure. 23. Stationary polarization curves obtained on Cu-Al anode in KF-AlF₃-Al₂O₃ melt at 700, 750 and 800 °C

Different processes can be identified at inflexion points at the polarization curves where $\partial^2 i_a / \partial E_a^2 > 0$ A cm⁻² V⁻². The corresponding potential can evident in what process take place according to the thermodynamic estimation. The curves display several oxidation processes occurred in the range of potentials between 1.8 and 3.5 V. The entire range can be divided into pre-oxygen and oxygen region. Several sections were observed in both regions:

- metal oxidation (**ab**) $xMe + yO^{2-} \xrightarrow{2y \cdot F} Me_xO_y + 2ye^-$ or $Me \xrightarrow{z \cdot F} Me^{z+} + ze^-$;
- oxygen ions oxidation (**bc**) $2O^{2-} \xrightarrow{4F} O_2 + 4e^-$;

- apparent oxygen ions oxidation limiting current section (**cd**) caused by low O^{2-} concentration.

The oxygen region starts at the potentials 2.3...2.6 V. The oxygen evolution onset potential as a function of both CR and T . At high CR and T values this potential was more negative. The oxygen evolution limiting current occurred in cases of low T and low CR . Before that, the anode was oxidized without significant diffusion and kinetic difficulties (**ab**).

High current densities in the region of the pre-oxygen potential indicate significant dissolution rates of anode oxidation products and a high partial current density of the anode oxidation in the oxygen potential region.

The total anode overpotential η_a was found from the polarization curves according to the equation:

$$\eta_a = E_i - E_0 \quad (21)$$

where E_i and E_0 are the anodic potentials at i A cm^{-2} and the reversible potential respectively.

The **ab** and **bcd** sections were treated separately. E_0 for **ab** process was taken equal to the open circuit potential. E_0 for **bcd** process was taken equal to the potential in **b** point. The obtained polarization curves show the mixed kinetics of oxygen evolution. At low current densities, the rate-determining step is a heterogeneous chemical reaction, thus the Tafel equation should be applicable to describe the dependence between activation overpotential η_{act} and current density:

$$\eta_{act} = \frac{RT}{pzF} \ln i_0 - \frac{RT}{pzF} \ln i \quad (22)$$

where R: gas constant, T: temperature, p: reaction order and i_0 : exchange current density respectively.

After an increase of current density up to a certain value (0.3 A cm^{-2} and higher) diffusion limitations occur, and the concentration overpotential η_{conc} can be expressed by the following equation:

$$\eta_{conc} = \frac{RT}{zF} \ln \left(1 - \frac{i}{i_l} \right) \quad (23)$$

where i_l : the limiting current density.

For the purpose to find the total overvoltage, decomposition to the activation and concentration components it was plotted vs. lni , and the linear section on the graph was considered as activation component of the overvoltage. It was extrapolated to higher values of i . The rest part was considered as the concentration component. The obtained results for $CR=1.2$ and $T=750$ and 800 °C are presented in figure 24. The experimental values of the concentration overvoltage $\eta_{conc}(exp.)$ were estimated by the equation

$$\eta_{conc}(exp.) = \eta_a - \eta_{act} \quad (24)$$

and were compared with the values calculated according to the equation (23), from which the limiting current density was also found.

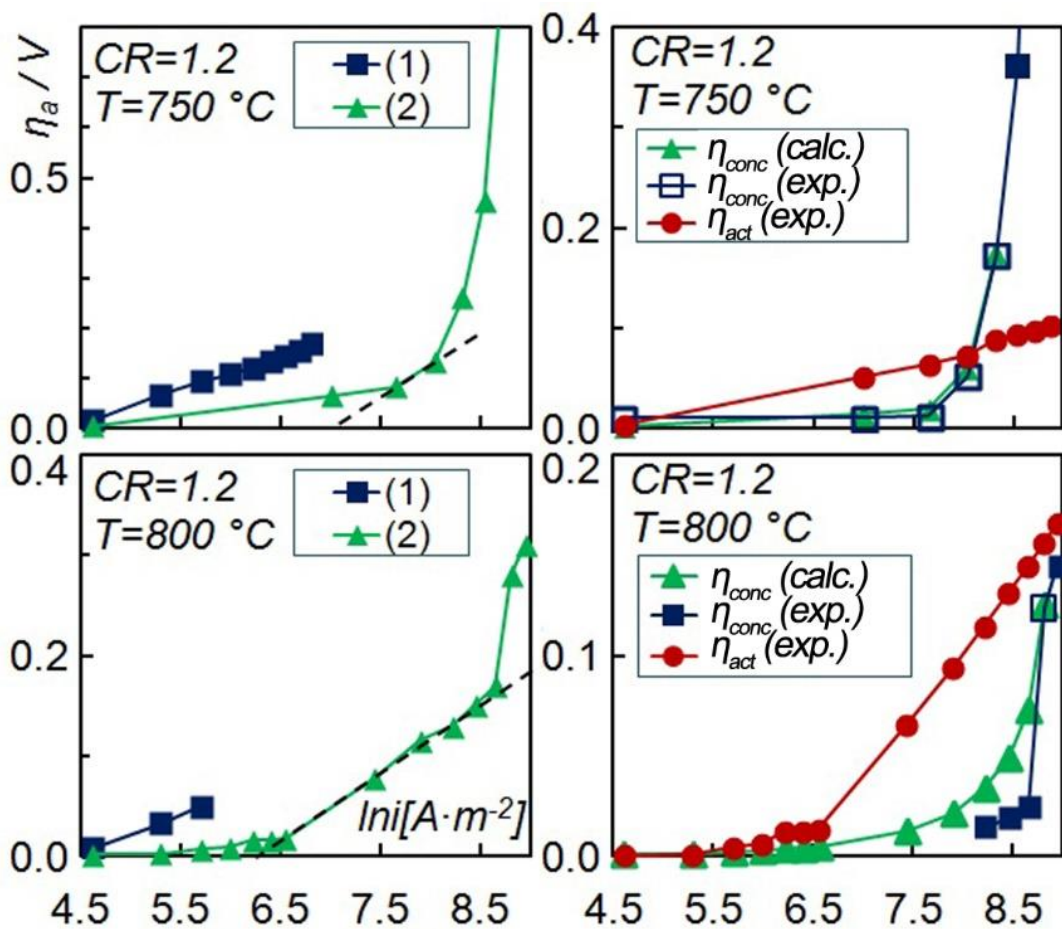


Figure 24. Dependence of overvoltage vs. partial current density of anode oxidation (1) and oxygen evolution (2); and different kinds of overvoltage (concentration and activation) for oxygen evolution in the $1.2KF-AlF_3-Al_2O_3$ melt at 750 and 800 °C

The curves (1) and (2) represent the oxidation of metal in the pre-oxygen region of potentials and oxygen evolution respectively. At both temperatures, the signs of kinetic and diffusion limitations appear on the oxygen evolution polarization curve. The exchange current density i_0 was found from the extrapolation of the curve linear section to the current density at zero

overvoltage. The temperature increase from 750°C to 800°C leads to the raise in i_0 from 40 to 74 mA cm⁻².

The experimental values of η_{conc} were in a good agreement with the calculated ones for the limiting current density $i_l = 0.42$ A cm⁻² at T=750 °C. An increase in T to 800 °C naturally leads to an increase in i_l up to 0.72 A cm⁻², however, there was an appreciable deviation between the experimental and calculated values in a certain range of current densities.

The reaction order p for the heterogeneous chemical reaction was also calculated from the equation (22). The values for T=750 and 800 °C were as high as 1.20 and 0.65 respectively that shows a considerable change in the reaction mechanism. The same calculations were performed at CR=1.3, 1.4 and 1.5. The results are presented in figures 25,26 and 27.

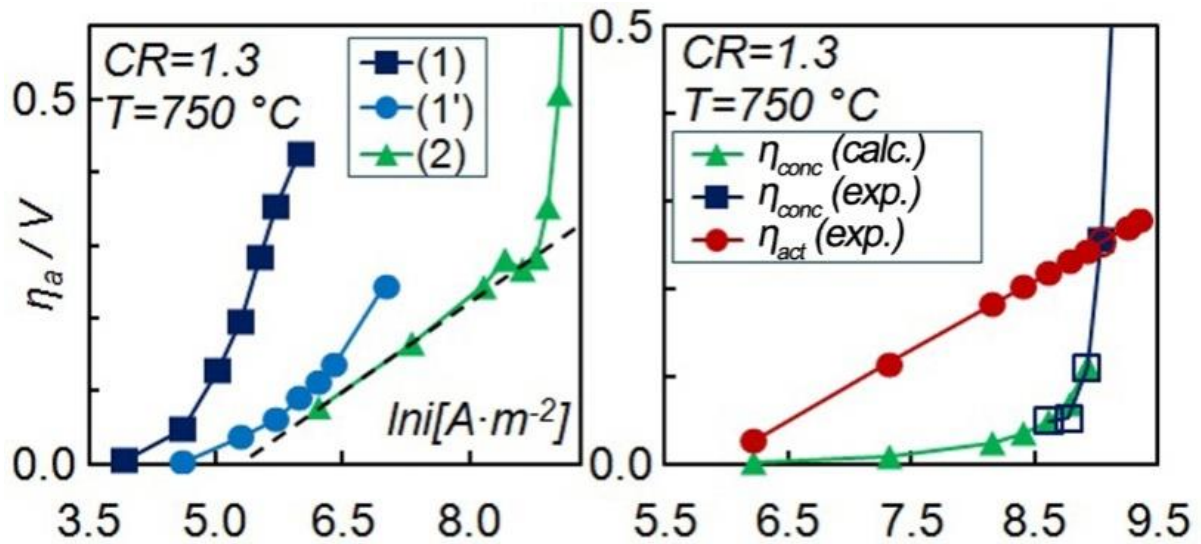


Figure. 25. Dependence of overpotential vs. partial current density of anode oxidation (1) and (1') and oxygen evolution (2); and different kinds of overpotential (concentration and activation) for oxygen evolution in 1.3KF-AlF₃-Al₂O₃ melt at 750 °C

There are two different processes observed in the pre-oxygen region of potentials [(1) and (1')] at CR=1.3 and T=750 °C. The first reaction started from onset potential below 2 V, and the second one started between 2.3 and 2.4 V. Both processes occurred with a significant overpotential and the rates were determined by the heterogeneous chemical reactions with low reaction orders according to the curve shapes. Oxygen evolution proceeded with mixed kinetics with i_0 , p and i_l equal to 36 mA cm⁻², 0.55 and 0.82 A cm⁻² respectively.

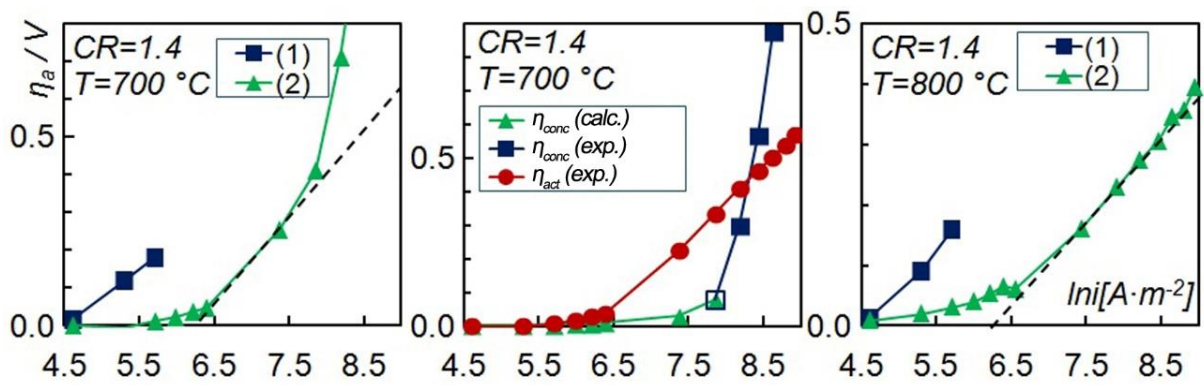


Figure. 26. Dependence of overpotential vs. partial current density of anode oxidation reaction (1) and oxygen evolution (2); and different kinds of overpotential (concentration and activation) for oxygen evolution in 1.4KF-AlF₃-Al₂O₃ melt at 700 and 800 °C

Increase in CR to 1.4 led to the appreciable increase in the limiting current density for the reaction at 800 °C, therefore, it was not observed in the studied range of current densities. A decrease in T down to 700 °C resulted in a significant increase in diffusion limitations of the process rate according to the obtained i_l value equal to 0.31 A cm⁻². Both T and CR . also affected the kinetic parameters of the chemical reaction. The values of i_0 and p were 52 mA cm⁻² and 0.20 at 700 °C. The same parameters were 49 mA cm⁻² and 0.33 at 800 °C.

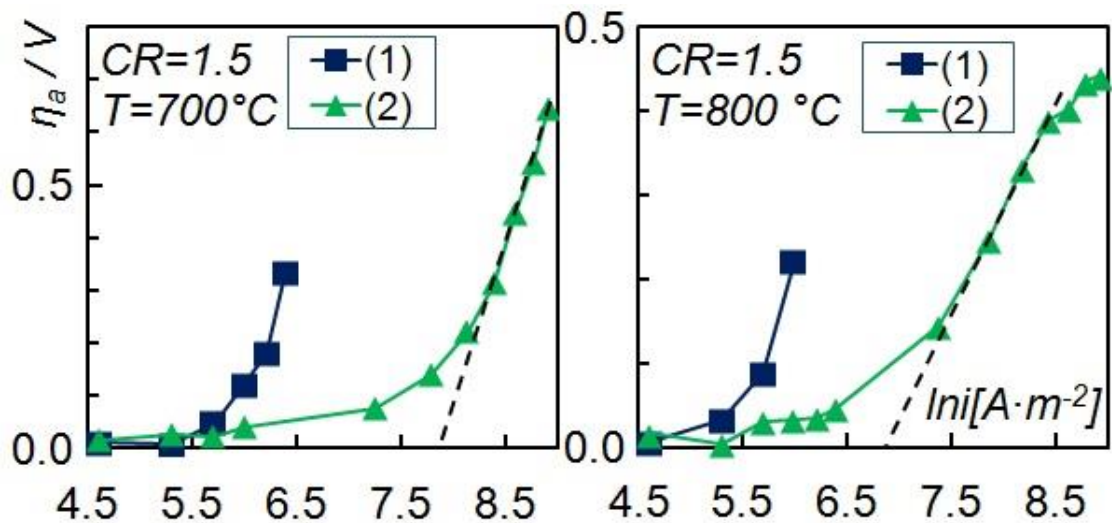


Figure. 27. Dependence of overpotential vs. partial current density of anode oxidation (1) and oxygen evolution (2); in the 1.5KF-AlF₃-Al₂O₃ melt at 700 and 800 °C

A further increase in CR led to an appreciable increase in i_l . It was not detected even at $T=700$ °C in the studied range of current densities. A certain deviation from linearity of the curve occurred at $i > 0.4$ A cm⁻², which can be connected with the process involving the fluorine ions discharge with the formation of copper fluorides.

Mass transfer coefficient k_s was calculated with the obtained data according to the equation:

$$k_s = \frac{i_l}{zFC} \quad (25)$$

where C: concentration of O^{2-} ions calculated from the alumina solubility, All the obtained information is presented in table 7.

Table. 7. Kinetic parameters of oxygen evolution

CR	T, °C	$c \cdot 10^2$, mole cm^{-3}	i_l , A cm^{-2}	i_0 , mA cm^{-2}	$k_s \cdot 10^4$, $cm s^{-1}$	p
1.2	750	2.61	0.42	40	0.833	1.20
1.3	750	2.703	0.82	36	1.57	0.55
1.4	700	2.754	0.31	52	0.583	0.20
1.5	700	2.721	n/a	237	n/a	0.08
1.2	800	2.757	0.72	74	1.35	0.65
1.4	800	2.859	n/a	49	n/a	0.33
1.5	800	2.94	n/a	102	n/a	0.20

Note: concentration of O^{2-} ions was estimated according to the alumina solubility

It is shown that i_l naturally increases with an increase in temperature and CR. The effect of CR is associated with the alumina solubility. The mass transfer coefficients for oxygen ions are in the range of $0.5-1.6 \cdot 10^{-4} cm s^{-1}$. The kinetic parameters of a heterogeneous chemical reaction are also affected by CR and T. The reaction order is higher at lower CR. In most cases, the reaction order is increased with temperature. The exception was observed at CR=1.2 where the value for T=750 °C was rather high, which may be due to the experimental error.

The obtained data for anodic kinetic parameters show that a decrease in the temperature, which is desired to increase the resistivity of anode towards corrosion, leads to the significant drop in mass transfer coefficient for the transport of complex oxygen ions to the anode. The solubility of alumina also highly affects the total anode overvoltage. The beneficial temperature for the industrial process should not be less than 800 °C.

According to the obtained results, the anode performed better at 800 °C. A further increase in temperature is undesirable due to a probable decrease in corrosion resistance. The CR should be maintained at $CR \approx 1.4$. The reasons for the chosen parameters are:

- the onset potentials of oxygen evolution are more negative at higher temperatures and higher CR;
- higher overvoltages are known to exist at temperatures below 800 °C;

- the stationary anodic potentials at current density 0.4 A cm^{-2} were similar in melts with CR=1.4 and CR=1.5;

3.2.3. Effect of particles volume fraction

Now the studies were conducted to investigate the effect of particle volume fraction on the anode process of Cu -10Al at $800 \text{ }^\circ\text{C}$ in melts with CR 1.4 due to above-mentioned conduction in the previous section being favourable for the anode material.

3.2.3.1. Stationary state polarization

Stationary galvanostatic polarization curves were recorded for melts ($\varphi=0$) and suspension ($\varphi=0.03\dots 0.15$) under chosen conditions ($T=800 \text{ }^\circ\text{C}$, CR=1.4) to estimate the limiting current density and the effect of particle volume fraction on the polarization curve. The data was compared to the previously obtained results for initially chosen conditions ($T=750 \text{ }^\circ\text{C}$, CR=1.3) (see section 3.2.1.1.) The plots are shown in figure 28.

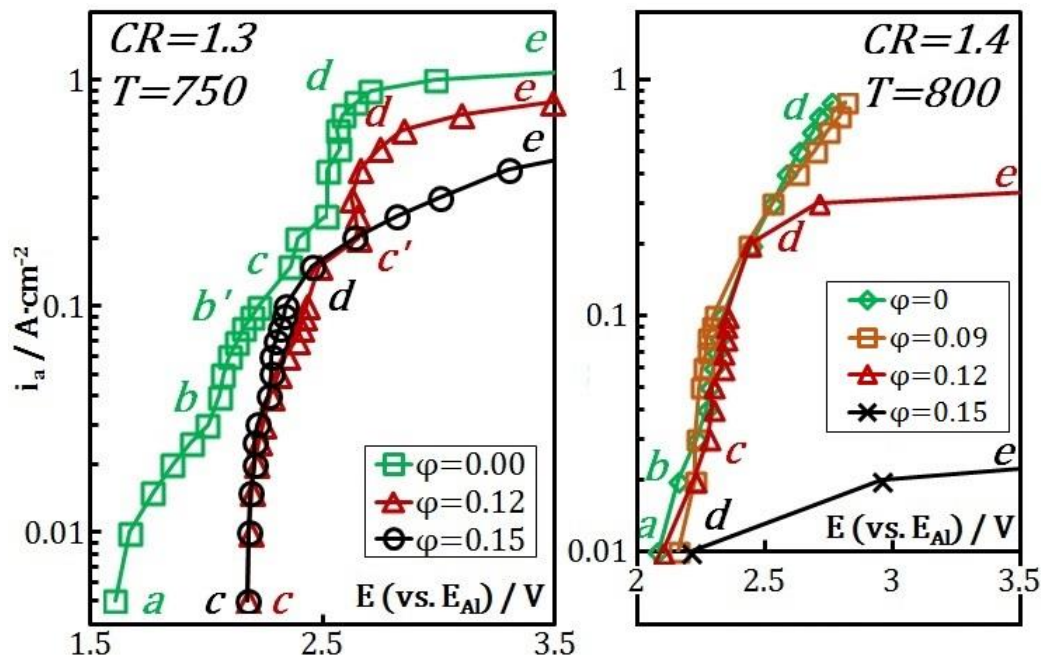


Figure 28. Stationary galvanostatic polarization curves of the anodic process in melts and suspensions ($\varphi=0-0.15$) with CR 1.3 and 1.4 at $750 \text{ }^\circ\text{C}$ and $800 \text{ }^\circ\text{C}$

The metal oxidation takes place in the region *ab*. The potentials in the melt ($\varphi=0$) with CR=1.3 indicate the formation of copper aluminates rather than oxides. At point *b*, the potential was equal to that of the Cu/CuO electrode, which shows the formation of CuO layer on the electrode in the region *bc*. Point *c* is where the oxygen evolution starts and it can be seen that the oxygen evolution occurs at high *i* in the melts ($\varphi=0$) and starts at low *i* while using suspensions. A sharp increase in the current density indicating the oxygen evolution

onset can be seen in the regions *cd* and *c'd* in suspension. The electrode in suspensions at $\phi=0.15$ had no metal oxidation region *ab*.

The limiting current densities observed in the *de* region are connected to the O^{2-} diffusion. It was noticed that the electrode used in melts ($\phi=0$) possess high limiting current density while an increase in ϕ drops the limiting currents, which might be due to the decrease in mass transfer coefficient K_s of the oxyfluoride ions. This states that with increasing suspension volume fraction in melts, limiting current decreases.

The comparison of the described results with those obtained in suspensions with CR 1.4 at 800 °C allows us to conclude that the limiting currents can be observed at 2.5-3 V in the suspension with $\phi=0.12-0.15$. In the case of suspensions with lower ϕ (0.09) and melts, limiting current densities were not achieved up to 1 A cm⁻². With an increase in the volume fraction ϕ from 0.12 to 0.15, the passivation of the anode was observed. From the galvanostatic curves, it can be concluded that the volume fraction with no more than 0.09 can be used. Further increase in the ϕ leads to a drastic increase in the overvoltage.

3.2.3.2. Cyclic voltammograms

The cyclic voltammetry recordings were made at a scan rate of 0.05 V/s in suspensions ($\phi=0.03-0.15$) at 800 °C and compared to the previously obtained result presented in **section 3.2.1.2.** as shown in figure 29.

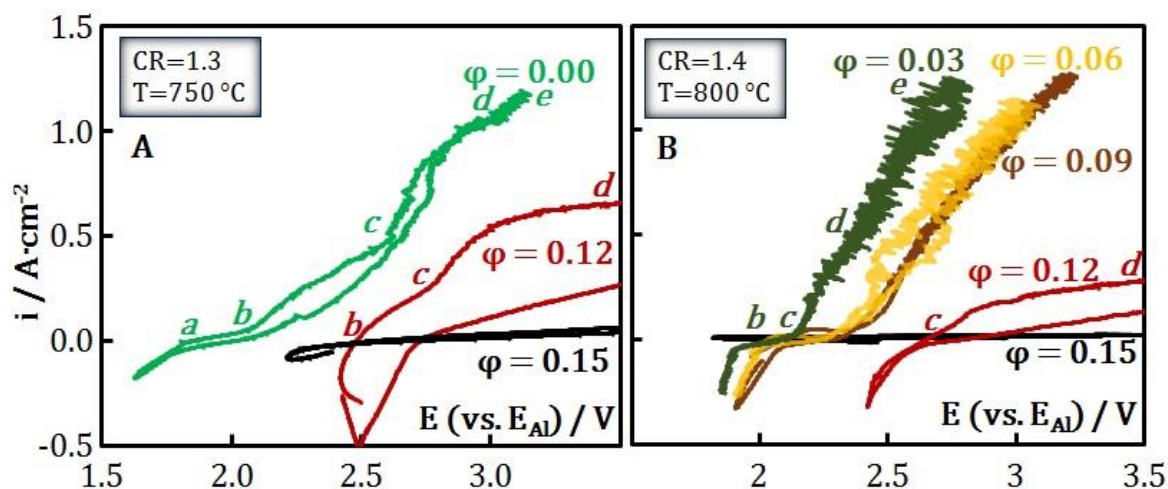


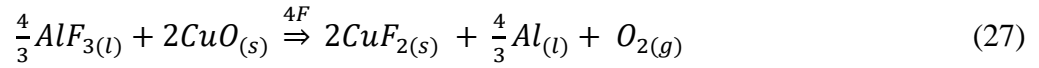
Figure 29. Cyclic voltammograms recorded in melts suspension with CR 1.3 and 1.4 at 750 °C and 800 °C

In case of pure melts, low current densities were observed, reflecting metal oxidation stage in the regions *ab* and *bc*. The potential at point *b* was 2.07 V, which is closer to the potential corresponding to Cu/CuO electrode (2.00 V). CuO might have been a dominating oxide layer

on the surface of the electrode in the *bc* region before the formation of copper aluminates or Cu₂O. Oxygen evolution happens from point *c* where the potential of the anode was above 2.5 V in the melt with CR=1.3. It has shifted toward more negative value after an increase in CR. Point *c* separates the pre-oxygen and oxygen evolution regions. At the region *de*, an increase in the current density can be seen and reason might be due to the reaction (26). In suspensions with high ϕ (0.12 and 0.15) at point *c*, the potential is more than 2.6V, which is close to the EMF of the reaction (27). The active CuO layer oxidation may take place leading to the formation of CuF₂ and O₂ evolution and it states the catastrophic corrosion of an oxide layer.

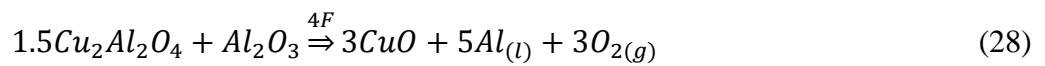


with $E^0 = 2.31 \text{ V}$



with $E^0 = 2.65 \text{ V}$

In suspensions with $\phi = 0.12$, oxygen evolution takes place from the beginning at 2.45V and reaction (28) is expected which occurs at potential 2.29 V, readily formed Cu₂Al₂O₄ oxide on the anodic surface at the beginning of the voltammetry process is transformed to CuO and oxygen evolution takes place at the same time. In the regions *cd* and *de*, the dissolution of the CuO oxide layer takes place with continuous O₂ evolution at potentials close to those required for the reaction (28) where CuO layer reacts with the AlF₃ present in the electrolyte and CuF is expected to be the product along with Al_(l) and evolution of O₂.



with $E^0 = 2.29 \text{ V}$

From the above equation, the activity of Al₂O₃ in the suspensions can be estimated using the Nernst equation (29):

$$E^0 = \frac{RT}{zF} \ln \frac{(P_{O_2})^3}{a_{Al_2O_3}} \quad (29)$$

In the *cd* region, passivation of the anode may take place where the reason might be the formation of the specific oxyfluoroaluminates [115]. In suspensions with $\phi = 0.15$, since the beginning of the sweep, high resistance was observed and no reactions occurred with considerable rate. The anode surface was completely passivated.

The dependence between the stationary current density at 2.7 V and the ϕ for suspension with CR=1.4 at 800 °C is shown in figure 30.

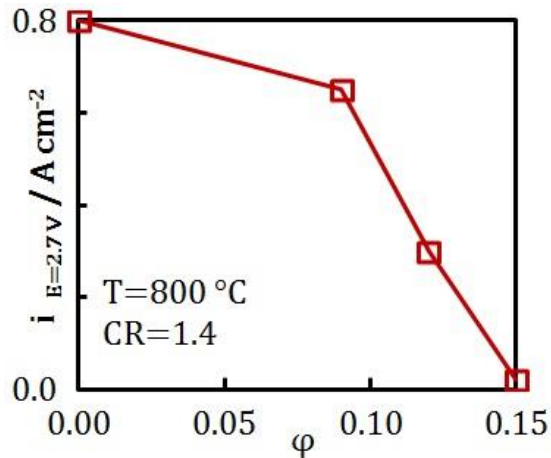


Figure 30. Dependence between stationary current density i at anodic potential $E=2.7$ V (relative to Al reference electrode) and alumina particles volume fraction in suspension with CR=1.4 at 800 °C

It can be observed that the stationary current slightly decreases in the range of ϕ between 0 and 0.09. After the addition of next alumina particles portion, the limiting current of oxygen evolution decreased. As a result, the observed stationary current decreases rapidly with increase in ϕ . Equation (30) represents the mass transfer coefficient correlated with the limiting current and solubility of alumina:

$$k_s = \frac{i_l}{zFC} \quad (30)$$

where k_s : mass transfer coefficient [cm/s], C: solubility [mol/cc]. The mass transfer coefficients are calculated for the set of conditions and presented in table 8.

Table 8. Mass transfer coefficients for diffusion of electroactive particles to the anode

T/ °C	CR	ϕ	$i_l / A \cdot \text{cm}^{-2}$	C/ mol·cc ⁻¹	$k_s \cdot 10^4 / \text{cm} \cdot \text{s}^{-1}$
750	1.3	0	0.90	0.00901	5.175
750	1.3	0.12	0.60	0.00901	3.450
750	1.3	0.15	0.15	0.00901	0.862
800	1.4	0.03	1.10	0.00738	7.722
800	1.4	0.12	0.20	0.00738	1.404
800	1.4	0.15	0.02	0.00738	0.140

Clearly, k_s value decreases with the increasing volume fraction in both cases; although the k_s values decrease with the increase in CR. The limiting currents for CR 1.4 at low ϕ were not

observed resulting in the difficulties to estimate k_s . It is worth noting that k_s slightly decreases with an increase in ϕ if $\phi \leq 0.12$. However, any further increase in ϕ leads to a drastic drop in k_s . The obtained k_s values are relatively less compared to the values obtained for gas evolving electrodes [118,119]. The low k_s values are due to the smaller bubbles formed on the Cu-Al electrode compared to the ones on carbon anode [120].

The industrial process of aluminium reduction in alumina suspensions seems to be operable with $\phi \approx 0.09$ if the highly dispersed alumina is supposed to be used.

3.3. Cathode process in the KF-AlF₃-Al₂O₃ system

In the present chapter, the findings related to the kinetic of cathode process on the tungsten (W) electrode with crucible acting as a counter electrode in KF-AlF₃ melt are discussed. The experiments were performed at 800°C in melts with CR (1.2 – 1.5). The electrochemical behaviour is investigated using cyclic voltammetry and chronopotentiometry.

3.3.1. Cyclic voltammetry

Typical cyclic voltammograms (CV) obtained on W in KF – AlF₃ melts at 800°C are shown in figure 31. The processes were tested in the melts with CR values of 1.3, 1.4 and 1.5 and the potential sweep rates (v) was between 0.01 and 0.2 V.s⁻¹. The cathode peaks associated with the aluminium reduction (**Al**) depending on the potential sweep rate and CR values were observed between -0.125 and -0.240 V (vs. Al) for all the CR values. The wave following the cathode peaks is associated with the potassium (**K**) reduction.

The oxidation of the cathode products happens at the anodic peaks (**Al'**). The anodic peaks occur in the range of -0.14 to -0.07 V. Hugely varying anode peaks indicate the oxidation of different forms of reduced aluminium in cathode process. Most certainly parallel reactions take place while the aluminium deposition on the cathode surface.

Reactions (31-33) occur indefinitely as the melts used are with 0 wt.% alumina content. These reactions influence the kinetics of the cathode process to an extent. Cathode peak related to the aluminium deposition was not observed on voltammogram with a sweep rate of 0.2 V/s for 1.4 CR. The reason might be the mixed kinetics involving the reduction of potassium.





With the decrease in the CR, the cathode peak current (i_{cp}) increases, stating a significant role of the melt composition on the kinetics of the cathode process. This effect might be due to the increase in the CR near the cathode layer and consumption of aluminium ions during the electrolysis process. Due to these phenomena, the liquidus temperature of the catalyte near the cathode and melt viscosity increases resulting in the diffusion difficulty.

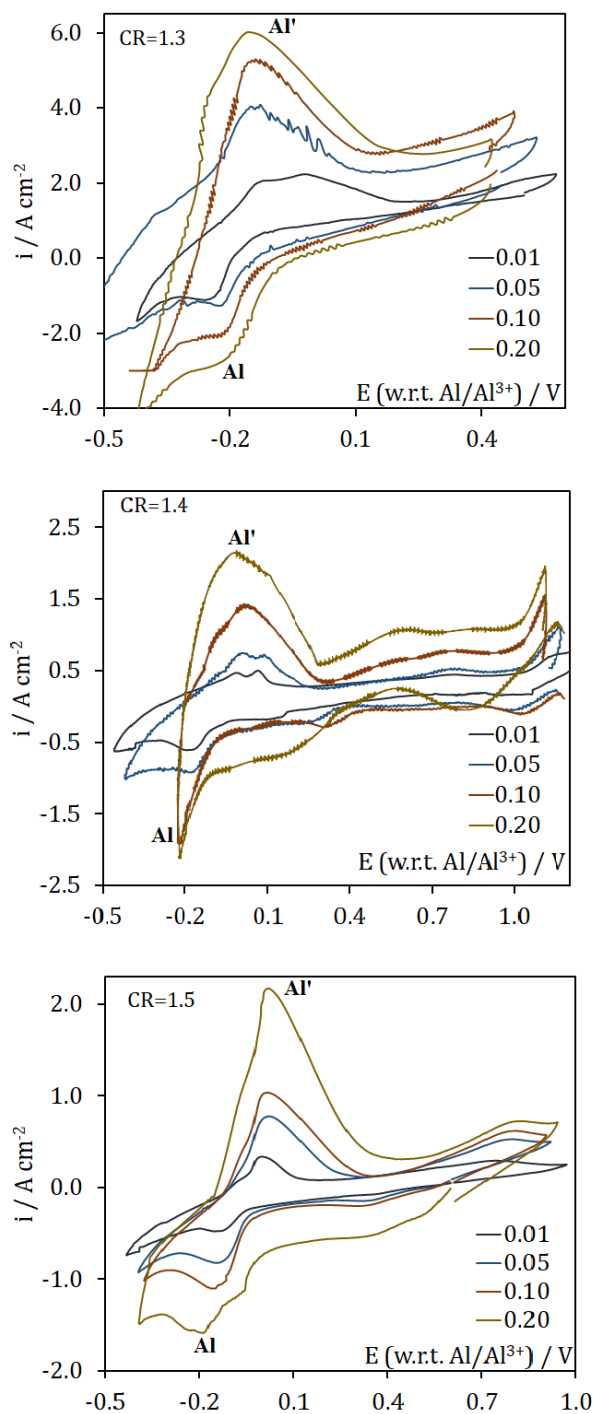


Figure 31. CVs obtained on W electrode at 800°C for KF-AlF₃ melts (CR = 1.3 to 1.5), Potential sweep rates (v) 0.01-0.20 V s⁻¹

Further tests were carried in the melts with CR 1.4 as the process was reversible. The effect of dissolved alumina wt.% on the aluminium reduction peaks in KF-AlF₃ melts with CR 1.4 is shown in figure 32. With an increase in the Al₂O₃ content in the melt, the cathode and anode peak currents tend to increase. The clear peaks on anode and cathode region can be seen, where C₁ is tungsten reduction at 0.7V (vs. Al). C₂ wave may be described to the beginning of the aluminium reduction process, which starts at -0.1V. C₃ corresponding to the aluminium

reduction is between -0.2 and -0.25 V depending on the alumina content in the melt. A₄ is related to the dissolution of aluminium from the intermetallic compound Al₄W at -0.1V. The aluminium oxidation peak A₅ at 0.1V can be seen, while the tungsten oxidation A₆ occurs at 0.75V.

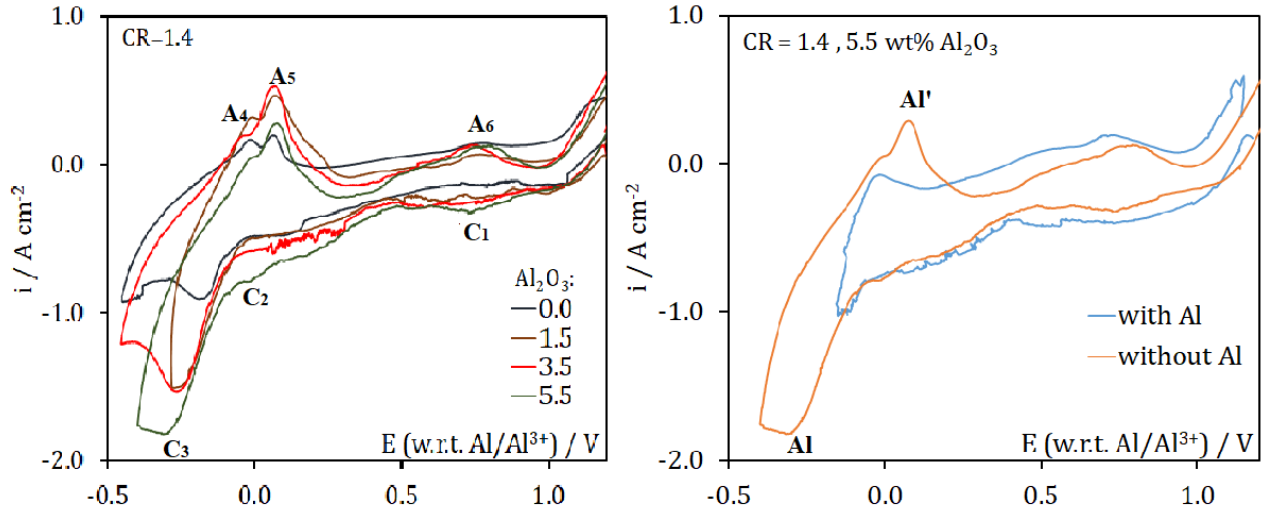


Figure. 32 Voltammograms obtained at the tungsten in the KF-AlF₃ melt (CR = 1.4) with varying Al₂O₃ wt% at 800°C dissolved aluminium in the melt with Al₂O₃ of 5.5 wt.% and potential sweep rate of 0.01 V s⁻¹

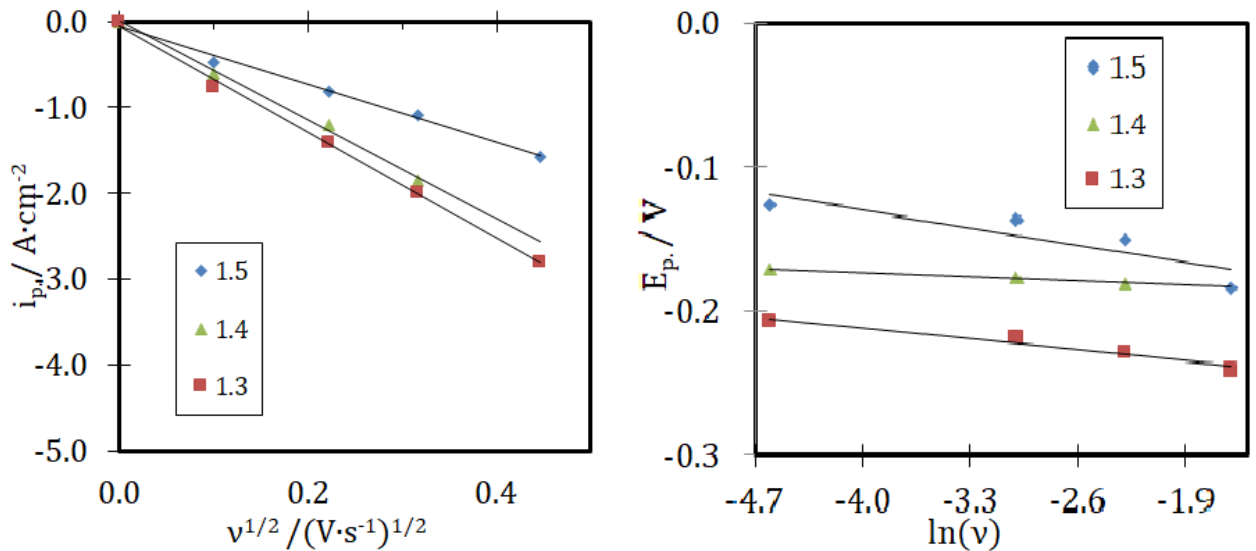


Figure 33. Dependences of $i_{cp}(v^{1/2})$ and $E_{cp}(\ln(v))$ of the aluminium deposition on tungsten electrode in the KF-AlF₃ melt (CR = 1.3 – 1.5) at 800°C

Table. 9. Kinetic parameters of aluminium deposition on tungsten in the KF-AlF₃ melts (CR = 1.3-1.5 mol mol⁻¹) at 800°C.

$v/V \cdot s^{-1}$	$v^{1/2}/$
--------------------	------------

$\left[\frac{KF}{AlF_3}\right]$ ratio		$(V \cdot s^{-1})^{1/2}$	$\ln(v)$	$i_{cp}/A \cdot cm^{-2}$	E_{cp}/V
1.3	0.01	0.1	-4.605	-0.771	-0.207
	0.05	0.223	-2.995	-1.31	-0.219
	0.10	0.316	-2.302	-2.001	-0.229
	0.20	0.447	-1.609	-2.81	-0.24
1.4	0.01	0.1	-4.605	-0.6	-0.17
	0.05	0.223	-2.995	-1.21	-0.176
	0.10	0.316	-2.302	-1.85	-0.180
	0.20	0.447	-1.609	-	-
1.5	0.01	0.1	-4.605	-0.475	-0.127
	0.05	0.223	-2.995	-0.81	-0.136
	0.10	0.316	-2.302	-1.09	-0.149
	0.20	0.447	-1.609	-1.57	-0.184

The values of cathode peak current densities (i_{cp}) and the potentials (E_{cp}) corresponding to i_{cp} for CR (1.3-1.5) and different sweep rates at 800°C are presented in table 9. The i_{cp} vs. $v^{1/2}$ show linearity for all the cases as shown in figure 33. stating that the process is diffusion controlled. The E_{cp} vs. $\ln(v)$ shows that there is a slight shift in the E_{cp} for CR 1.3 and 1.5, meaning that the process is a quasi-reversible diffusion-controlled. Although, in melts, with CR 1.4 the E_{cp} swift was not seen stating it to be a reversible process. Randles-Sevcik equation (34) can be used to calculate the diffusion coefficient of the electroactive ions to the tungsten cathode as all the processes are diffusion controlled [121].

$$i_{cp} = -0.4463(zF)^{3/2}C \left(\frac{vD}{RT}\right)^{1/2} \quad (34)$$

where i_{cp} :cathode peak current density [$A \cdot cm^{-2}$], C : concentration of the electroactive ions [mole/cc], D : diffusion coefficient of the electroactive ions [$cm^2 \cdot s^{-1}$], v : potential sweep rate [$V \cdot s^{-1}$]

Table. 10. Diffusion coefficients ($D \times 10^5 / cm^2 \cdot s^{-1}$) of electroactive ions in KF-AlF₃ melts at 800°C

$\left[\frac{KF}{AlF_3}\right]$ ratio	$C_{Al(III)}/mole \cdot cm^{-3}$	Al ₂ O ₃ wt. %	$D \cdot 10^5/cm^2 \cdot s^{-1}$
1.2	0.00919	0	2.724
1.3	0.009006	0	0.078 – 0.13
1.4	0.00892	0	0.079–0.0835
1.5	0.0088	0	0.028–0.053

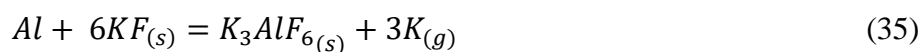
1.4	0.00918	1.5	0.488
1.4	0.009537	3.5	0.474
1.4	0.00989	5.5	0.624

The diffusion coefficient values of the melts with CR's (1.2 to 1.5) lies from 0.028 to 2.724×10^{-5} . It can be observed from table **10**. that with an increase in the CR, the D decreases which is in good agreement with Nikolaev et al.[52]. Besides, the D increases with the increase of Al₂O₃ wt. %.

3.3.2. Stationary-state polarization:

Galvanostatic polarization curves were obtained to examine the kinetics of the cathode process on the tungsten electrode in KF-AlF₃ melts to determine the aluminium electrolysis parameters. Typical stationary polarization curves were acquired for CR (1.4 and 1.5) and Al₂O₃ content in melts with CR 1.4 at 800 °C and are shown in figure **34**. The aluminium reduction takes place at the potential ≈ -0.2 V. The cathode limiting current density (i_l) are ranging between 0.45 and 0.5 A.cm⁻² depending on the CR and Al₂O₃ wt.%. The potential at high i_c (between -0.7 and -1.1 V) did not vary, which is associated to the potassium reduction on the cathode certainly the mixture of K₃AlF₆ and KAlF₄ salts with high electric conductivity [52].

Limiting currents of 0.45-0.50 A.cm⁻¹ were observed in melts with CR's 1.4 and 1.5. The cathode limiting current increases with the CR decrease [53]. This is due to the increase in the diffusion layer thickness associated with a higher content of AlF₃. This shows that [KF/AlF₃] ratio plays a key role in the kinetics of the cathode process. The i_l varies between 0.45 and 0.50 A.cm⁻² with increasing Al₂O₃ content from 0 to 5.5 %. The absence of a proportional rise of i_l with Al₂O₃ content increase in the melts implies that the process was under the mixed kinetics. The same phenomena were observed using the W cathode in melts (CR 1.3) with increasing Al₂O₃ content [53]. Reaction **(35)** is possible to occur over -0.6 V along with the parallel reaction **(36)**. Segments of electrically conductive KAlF₄ and K₃AlF₆ are subject to form on the surface of the cathode, leading to the passivation.



$$\Delta G_f^o (800^\circ C) = 7.251 \text{ kJ/mole of Al}$$



$$\Delta G_f^o (800^\circ C) = -180.876 \text{ kJ/mole of Al}$$

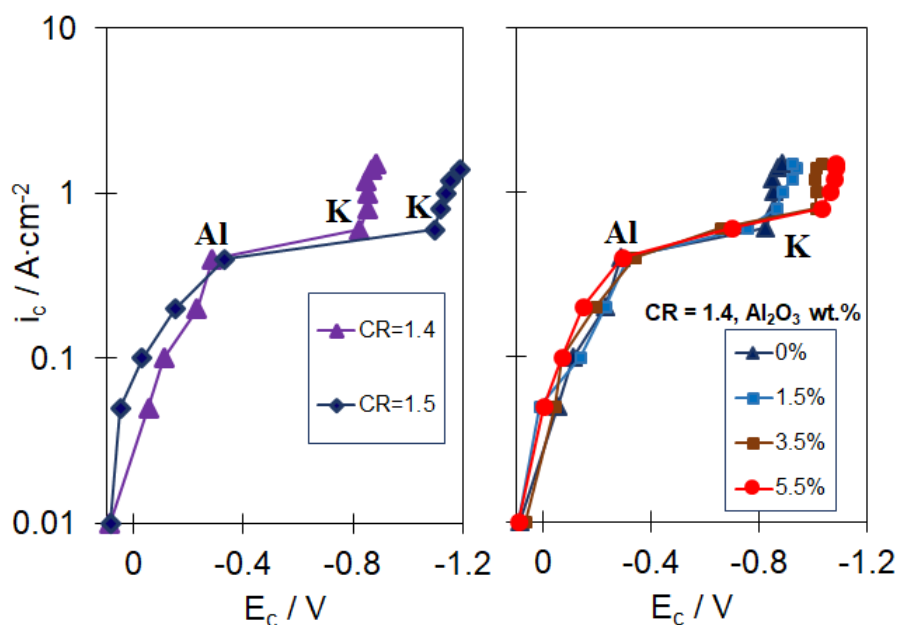


Figure 34. Stationary polarisation curves measured on W electrode at 800°C for CR 1.2-1.5 and varying Al₂O₃ wt.% in melts with CR 1.4

Equation (30) is used to calculate the mass transfer coefficients for the set of conditions and is presented in table 11.

Table. 11. Mass transfer coefficients for the diffusion of electroactive particles to the cathode at 800 °C.

$\left[\frac{KF}{AlF_3}\right]$ ratio	Al ₂ O ₃ wt. %	limit current i_l / A.cm ⁻²	Mass transfer coefficient $k_s \cdot 10^4 / \text{cm}^2 \cdot \text{s}^{-1}$	Diffusion layer thickness δ / cm
1.4	0	0.4500	1.74901	0.00442
1.5	0	0.4500	1.7664	0.00202
1.4	1.5	0.4700	1.76854	0.0276
1.4	3.5	0.4800	1.77478	0.0273
1.4	5.5	0.5000	1.74636	0.0358

Note: C is the concentration of Al(III) ions in the melt.

The mass transfer coefficient increases with increasing CR and alumina content in the melt. While the diffusion layer thickness decreases with an increase in the CR and increases with the increasing alumina content in the melt, which was expected.

4. Alumina behaviour in KF-AlF₃-Al₂O₃ melts and suspension

While evaluating the performance of a given electrolyte, physicochemical properties like electrical conductivity, liquidus temperature, the solubility of alumina, vapour pressure and density, among which alumina solubility places a crucial role for industrial processing. The dissolution of alumina is the critical process in both commercial NaF-AlF₃ and low-temperature KF-AlF₃ melts. Much attention is to be given to the KF-AlF₃ melts in recent times. As this melt has low liquidus temperature compared to the sodium ones, which allows the usage of metallic, cermets or ceramic anodes instead of consumable carbon blocks.

The decrease in the electrolyte temperature improves the corrosion resistance of the oxygen-evolving electrodes, at the same time reduces the solubility and dissolution rate of the alumina leading to the formation of sludges (trapping of undissolved alumina under the liquid aluminium in the cell) and catastrophic corrosion of the anode. Thus, determining the behaviour of alumina in the KF-AlF₃ melts gains importance. The purpose of this chapter is to provide a complete understanding of the dissolution rate and sedimentation of alumina in KF-AlF₃ melts and suspensions. The effects of the temperature, particle size and phase composition of the dispersed material and its volume fraction in the suspension on the dissolution kinetics and the sedimentation velocity are studied. The experiments are carried out over the melts with cryolite ratios 1.3 and 1.5 in the range of 750 - 850 °C. Three different types of aluminium oxide were used.

4.1. Experimental

Materials preparation

Electrolytes were synthesized at 900 °C from the dried individual chemically pure (p.a.) salts KF and AlF₃. Drying lasted for 4 hours at 400 °C. The prepared melt was purified from oxygen ions during 2 h electrolysis with a graphite anode under the potential of 1.5 V relative to the aluminium potential. For dissolution and sedimentation studies 3 types of materials were chosen: smelter grade alumina (SGA) of Achinsk refinery, commercial α -Al₂O₃ (corundum) and mechanically activated (MA) alumina. The properties of these materials are presented in table 12.

Table 12. Materials properties

Material	Typical particle size, μm	BET-surface, $\text{m}^2\cdot\text{g}^{-1}$	Content of α -modification	True density, $\text{kg}\cdot\text{m}^{-3}$	Reported dissolution rates
----------	--------------------------------------	---	-----------------------------------	---	----------------------------

SGA	40-80	94	12	3630	Medium
MA alumina	1-10	60	12	3630	High
α -Al ₂ O ₃	1-5	60	98	3950	Slow

Experimental method

The electrochemical measurements were often carried out in a two-electrode graphite cell heated by electrical furnace under air atmosphere in the temperature range of 750–850 °C. Two different experimental cells were used. The first one (figure 35a) was used with two electrochemical methods: electrochemical impedance spectroscopy (EIS) performed with frequency response analysis (FRA) at the galvanostatic mode in the range of 100-10000 Hz at the current amplitude of 10 mA; and open circuit potentiometry (OCP) with the concentration cell EMF measurement. The measurements were supported with visual observations. The second cell (figure 35b) was used for the critical current measurements at the linear sweep of the working electrode potential. The photo of the cell is shown in figure 36. The sweep was performed in the range of 1-10 V at the rate of 100 V·s⁻¹. Electrolyte temperature was measured by the k-type thermocouple in a BN case connected to the controller and maintained constant ($\pm 2^\circ\text{C}$). The current and the potential were supplied or measured using Potentiostat AutoLab PGSTAT 302n and NOVA 2.1 Software (The Metrohm, Netherlands). Both cells were placed inside the steel crucible compacted with graphite powder (not shown in the figure).

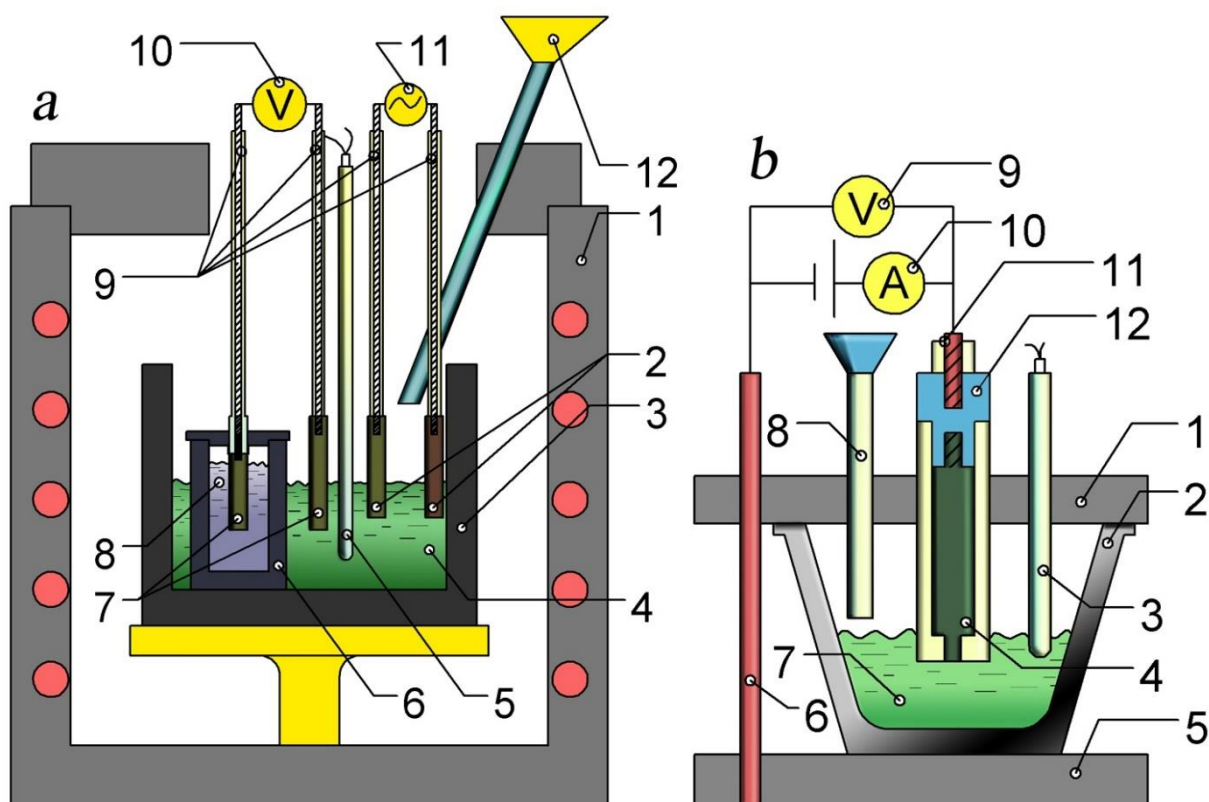


Figure 35. Schematic representation of experimental cells: a – a set up for coupled EIS and potentiometry methods (1 electrical furnace, 2 electrodes for AC polarization, 3 graphite vessel, 4 studied electrolyte (suspension), 5 thermocouple, 6 porous graphite crucible, 7 graphite electrodes for OCP, 8 electrolyte with the constant O^{2-} concentration, 9 current leads, 10 voltmeter, 11 potentiostat, 12 feeder); b – an electrochemical cell for linear sweep potentiometry (1 graphite cover, 2 glassy carbon vessel, 3 thermocouple, 4 graphite sensor, 5 graphite bottom, 6 cathodic current lead, 7 studied electrolyte, 8 feeder, 9,10 potentiostat, 11 anodic current lead, 12 steel connector)

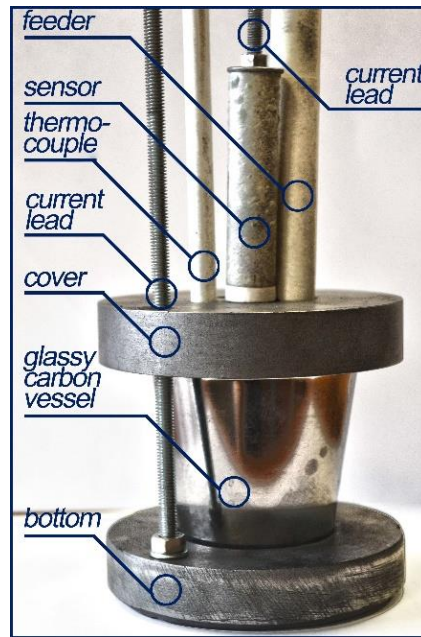


Figure36. Photo of the cell for the linear sweep voltammetry

For the sedimentation study, the second half-cell was removed from the crucible. The suspension was mixed for one minute with a manual stirrer and after that EIS technique was continuously performed to record the resistance change in the upper part of the cell caused by the change in the solid particles local volume fraction.

4.2. The dissolution rate of alumina in KF-AlF_3 melts

4.2.1. Characterising the dissolution rate

The electrical conductivity κ_l of the molten cryolite is known to decrease with an increase in the dissolved alumina concentration C_A . Addition of 1 wt.% of alumina will cause an appreciable change in cell resistance of 2.5-5 %. The alumina dissolution rate can be estimated using the resistance-time dependence phenomena. An appropriate technique to determine the resistance is electrochemical impedance spectroscopy (EIS). The resistance R of the electrochemical system is calculated out of impedance Z , given by the expression [121]:

$$\mathbf{Z} = \mathbf{R} - j \cdot \frac{1}{\omega \cdot C} = \mathbf{Z}' - j\mathbf{Z}'' \quad (37)$$

where $j = \sqrt{-1}$, $Z' = R$ is the real part of the impedance, $Z'' = \frac{1}{\omega \cdot C}$: imaginary part of impedance, ω : frequency of the AC polarization, C : capacitance of the electrochemical system. The phase angle φ , is given by the equation:

$$tg\varphi = \frac{z''}{z'} = \frac{1}{R \cdot \omega \cdot C} \quad (38)$$

The EMF of the galvanic cell is given by the Nernst equation [104]:

$$E^{rev} = E^0 - \frac{RT}{nF} \ln \frac{a_O^{\nu_O}}{a_R^{\nu_R}} \quad (39)$$

where E^0 : standard EMF, a is the activity, ν : stoichiometric coefficient, subindexes O and R denote oxidation and reduction forms.

If the activities of the species are unknown the EMF can be expressed as a function of dissolved alumina (for cryolite-alumina melts) concentration by the semi-empirical formula [94]:

$$E^{rev} = -\frac{\Delta G^0}{6F} + \frac{RT}{6F} \ln \left(\frac{C_{A(sat)}}{C_A} \right)^{2.77} \quad (40)$$

where ΔG^0 is the change of Gibbs energy in the corresponding reaction.

For the concentration cell



the EMF can be expressed by the equation:

$$E^{rev} = \frac{RT}{6F} \ln \left(\frac{C_{A(II)}}{C_{A(I)}} \right)^{2.77} \quad (42)$$

where $C_{A(I)}$ and $C_{A(II)}$ are alumina concentration in the half-cells *I* and *II*.

The noted relations can be used for dissolution rate measurements if we measure EMF of the concentration cell as a function of time after addition of alumina into one of the half-cells.

4.2.2. Alumina dissolution rate

Smelter grade alumina

The concentration cell EMF recorded for 15 minutes after adding 2 g (1 wt.%) of SGA to the 1.3KF-AlF₃-Al₂O₃ melt at 750°C was normalized concerning the steady-state or quasi-steady-state value and is shown in figure 37. The feeding time of alumina into the melt was less than 1 s. The normalization was made for easy comparison between the curves which possessed different stationary EMF due to the different alumina activities and simultaneously eliminate the effects of the constant errors related to the imperfections of the experimental procedure. The stationary potential difference E_{ss} was in the range of 10-35 mV depending on the concentration difference between the two half-cells.

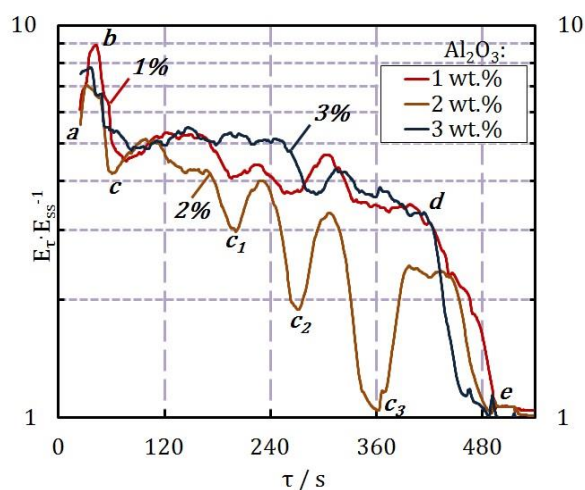


Figure 37. Dependence of normalized EMF of concentration cell (*in ln scale*) vs. time for addition of 2 g of SGA to 200 g of 1.3KF-AlF₃ melt with 1-3 wt.% of dissolved alumina at 750 °C

The highest concentration EMF value of 340 mV was recorded and the potential difference after the saturation of the studied melt was ranging between 10 and 30 mV. The potential difference was higher than zero due to the slight difference in the ionic composition of the electrolytes in the two half-cells and the diffusion potential at the porous membrane (asymmetry potential). The EMF decreases drastically for the first minute after the addition of alumina (*ab* region). The peak *abc* is associated with heat effect caused by the addition of cold sample, the crystallization and melting of the electrolyte, the dissolution of the added sample and the evaporation of the moisture. These effects are independent of the concentration of O²⁻ ion in the studied electrolyte. The decrease in the EMF (region *cd*) is associated with an increase in the concentration of oxygen ions. The significant oscillations $E_{\tau} \cdot E_{ss}^{-1}$ were observed at the experiment with 2 wt.% of dissolved alumina (*c-c₁-c₂-c₃-d*). The nature of these oscillations is unclear.

It was observed that in the melts with 1 and 3 wt.% alumina, there is a drastic drop of EMF between the 420 and 500s time period followed with a horizontal straight line reflecting the equilibrium. The duration of the dissolution was 320, 360 and 220 s for 1, 2 and 3 wt.% of alumina respectively. These values give the dissolution rates as high as 0.031, 0.028 and 0.045 g·kg⁻¹·s⁻¹ (0.54, 0.48, and 0.78 mole·m⁻³·s⁻¹) that is 2-4 times higher than normally reported for electrolytes based on sodium cryolite [99] The similar results were reported previously for NaF-KF-AlF₃ melts at 950°C [107,108].

The typical Nyquist and Bode plots obtained with the EIS technique are presented in figure 38

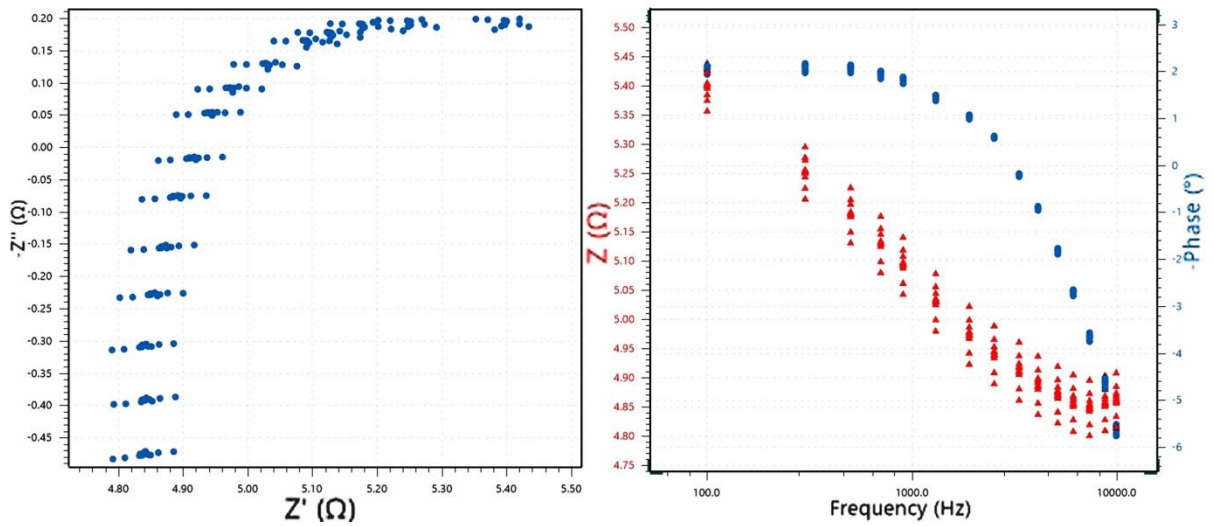


Figure 38. Nyquist plot $-Z''$ vs. Z' (left) and Bode plot for a set of measurements over the quasi-equilibrium molten 1.3KF-AlF₃ system at 750 °C

The effect of temperature on the dissolution kinetics at different concentration of O²⁻ ions are presented in figure 39. The relation between the normalized resistance and time was demonstrated by adding 2 g (1 wt.%) of SGA in 1.3 KF-AlF₃ melt with different amount of dissolved alumina (0 to 5 wt.%).

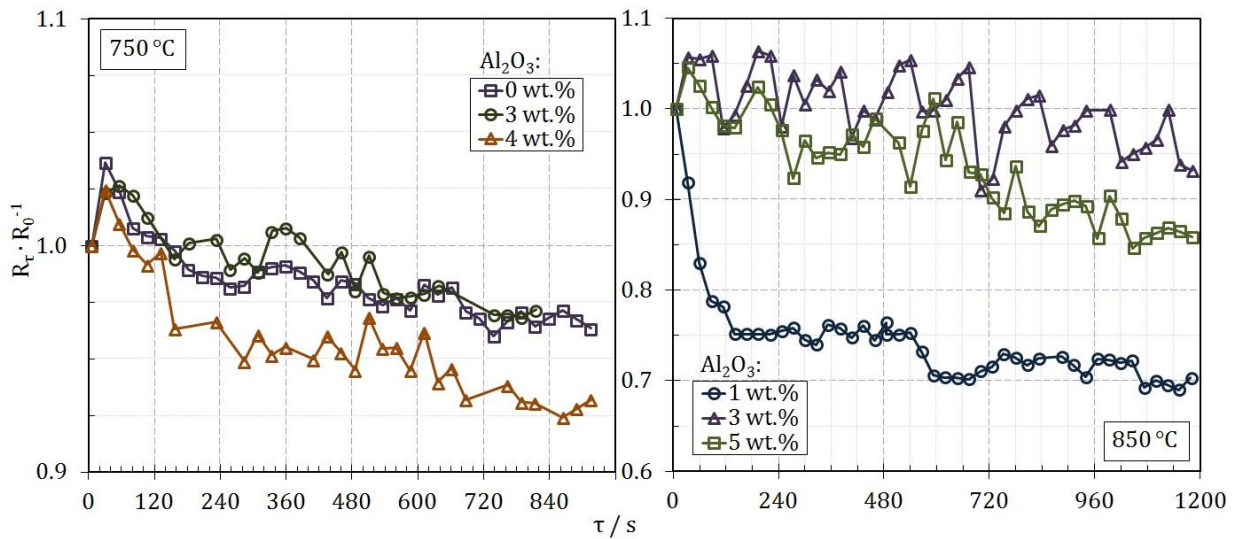


Figure 39. Dependence of normalized resistance vs. time for addition of 2 g (1 wt.%) of SGA to 200 g of 1.3KF-AlF₃ melt with 0-5 wt.% of dissolved alumina at 750 and 850 °C

It can be seen that the recorded resistance decreased with time after addition of SGA into the melt that contradicts the data from the known literature. The complex oxygen ions are known to decrease the electrical conductivity as well as a decrease in temperature due to the addition of the cold sample and its dissolution. The measured resistance was as high as 5.05Ω at the beginning of the set of experiments and reduced to 1.95Ω with the saturation of the melt. The

drop in the resistance was observed in 90% of experiments. The extremely high resistance could be caused by the interfacial passivation layers on the electrodes that were destroyed with an increase in dissolved alumina concentration.

In most cases, the short increase in resistance is observed during the first 30-50 s after the alumina charge. This phenomenon could be associated with the decrease in the temperature and solidification of the electrolyte with the increase of the solid phase volume fraction. After the peak of the curve is reached, it starts to decrease and the initial slope is different for various alumina concentrations. The highest slope is observed for the low dissolved alumina concentrations at both temperatures. The end of the dissolution process is difficult to determine on the curves. However, with the data obtained with OCP, it can be assumed that equilibrium is set between 360 and 500 s for different concentrations at 750 °C when the resistance is not decreased for an appreciable period of time (60 s or more). While the alumina dissolution at 850 °C lasts for less time. For example, at $C_A=1\text{wt.}\%$ this process is completed in 125 s after the addition. Growth of the concentration to 5 wt.% leads to an increase of dissolution time to 300 s.

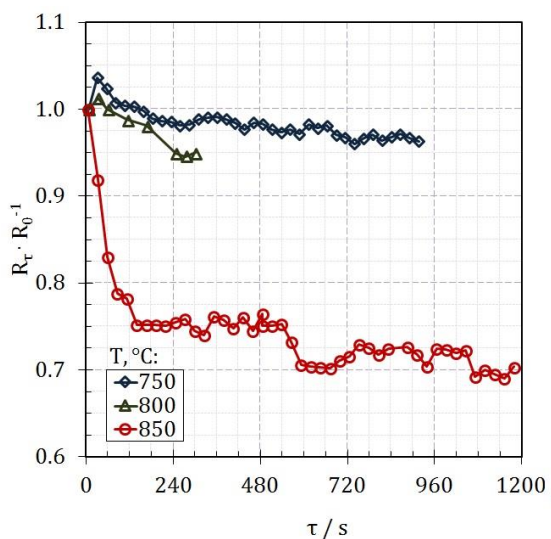


Figure 40. Dependence of normalized resistance vs. time for addition of 2 g of SGA to 200 g of 1.3KF-AlF₃ melt at 750, 800, 850 °C

The initial increase in the resistance, further decreases in the rate and the time before reaching the equilibrium (or quasi-equilibrium) depend on the temperature, which can be witnessed in figure 40. The dissolution rates (if it can be associated with the mentioned decrease) were as high as 0.023, 0.040 and 0.080 g·kg⁻¹·s⁻¹ at 750, 800 and 850 °C respectively. It means that an increase in temperature up to 50 °C doubles the dissolution rate. This is in agreement with previously obtained results reported in [107] for the NaF-KF-ALF₃ melt at 950-975 °C.

Linear sweep voltammetry (LSV) method is used to determine the dissolution rate of alumina. Typical linear sweep voltammograms for dissolution of 2 g alumina portion in 200 g of electrolyte is displayed in figure 41. The peaks on the voltammograms are critical currents I_p connected with the concentration C_0 of O^{2-} ions by the expression [109]:

$$I_p = 0.28 \cdot z \cdot F \cdot A \cdot C_0 \cdot \sqrt{\pi \cdot D \cdot b} \quad (43)$$

Where

$$b = \frac{\alpha \cdot n \cdot F \cdot V}{R \cdot T} \quad (44)$$

α : transfer coefficient, V : potential sweep rate, T : temperature (in Kelvin), A : surface area of the electrode, D : diffusion coefficient.

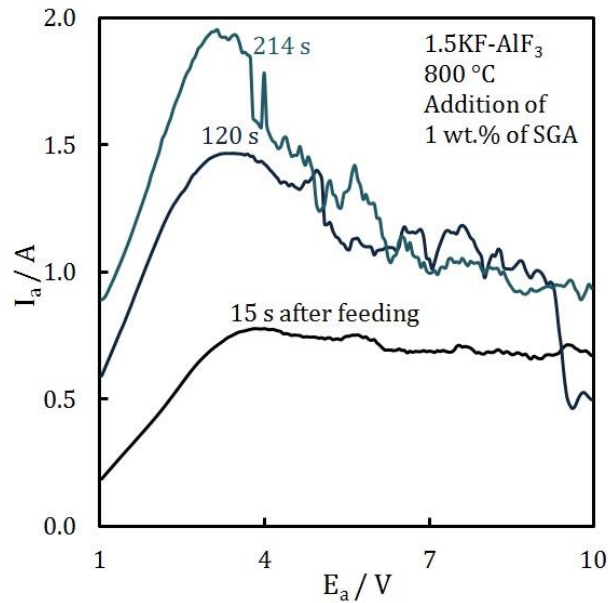


Figure 41. Dependence of peak current on linear sweep voltammograms recorded with 100 V s^{-1} at different times after addition of 2 g of SGA to 200 g of 1.5KF-AlF_3 melt with 0-2 wt.% of dissolved alumina at $800 \text{ }^\circ\text{C}$

The equation (43) cannot be implemented for direct determination of the concentration due to the complicated hydrodynamic and diffusion conditions; although, the experimental data can be calibrated for the certain electrochemical system. The dependence between critical current vs. time can also be used to determine the dissolution rate. The results of critical current measurement at potential sweep with the rate of $10 \text{ V} \cdot \text{s}^{-1}$ for anodic process on graphite in the 1.5KF-AlF_3 melt with different alumina concentrations for dissolution of SGA at $800 \text{ }^\circ\text{C}$ are shown in figure 42.

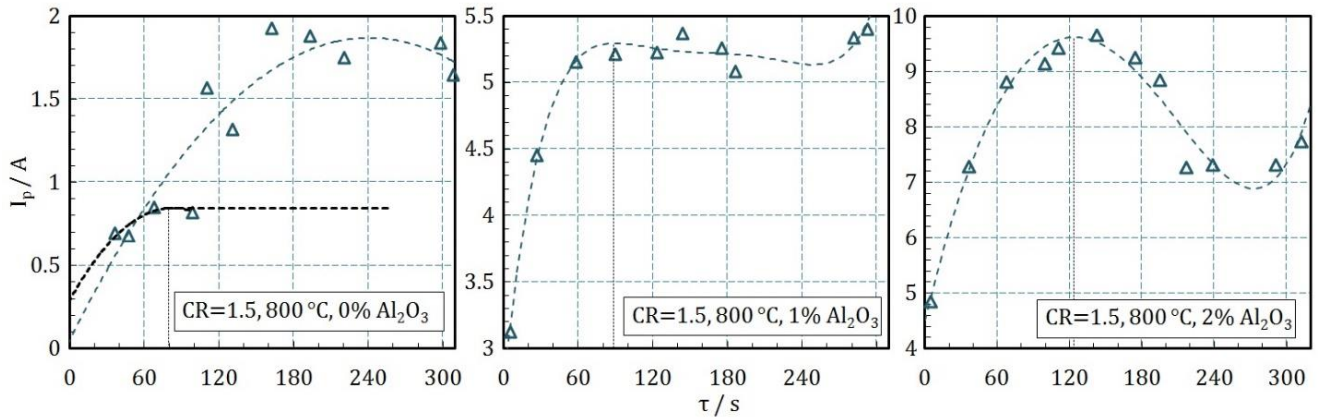


Figure 42. Dependence of peak current on linear sweep voltammograms vs. time for addition of 2 g of SGA to 200 g of 1.5KF-AlF₃ melt with 0-2 wt.% of dissolved alumina at 800 °C

The peak currents were increased with the time after the addition of alumina to 1.5KF-AlF₃ melt. The first plateau is reached after 79 s in the pure melt. The second significant increase followed after the plateau and probably was due to change in the active surface area of the anode. Increase of the alumina concentration to 1% led to an increase in the time before the plateau up to 90 s. In melts with 2 wt.% of dissolved alumina, the dissolution time was 122 s, followed with an appreciable drop. The calculated dissolution rates were 0.127, 0.111 and 0.082 g·kg⁻¹·s⁻¹ for 0, 1, and 2 wt.% of dissolved alumina respectively.

Mechanically activated alumina

The second tested material was MA alumina, which is believed to increase the dissolution rate at low concentrations up to 2-4 times in comparison with SGA [110]. The normalized resistance and EMF of the concentration cell are placed on the same plots for dissolution of SGA and MA alumina in 1.3KF-AlF₃ (pure and 2 wt.% of alumina) at 800 °C which is shown in figure 43.

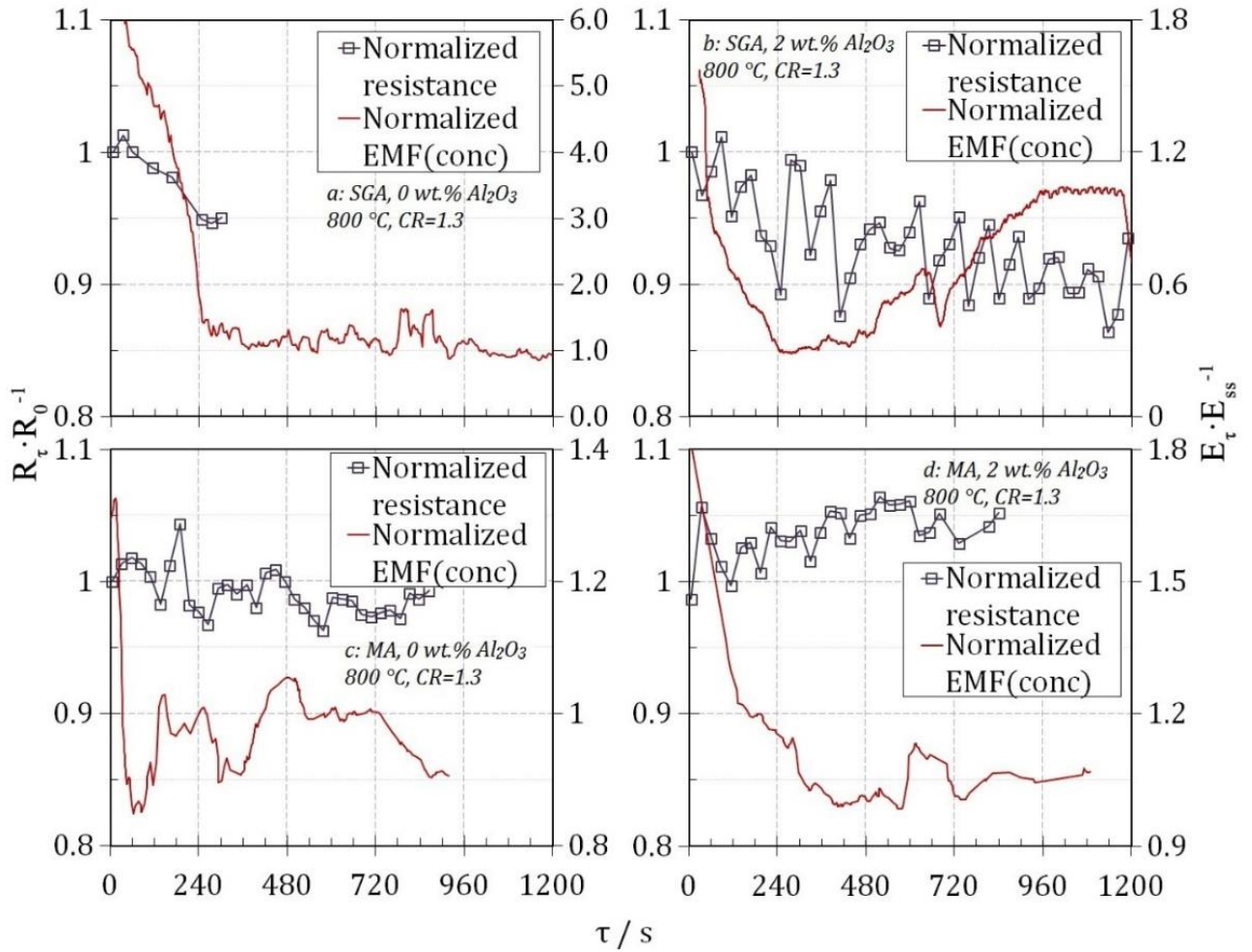


Figure 43. Dependence of normalized resistance and normalized EMF of concentration cell vs. time for addition of 2 g of SGA (a and b) or MA alumina (c and d) to 200 g of 1.3KF-AlF₃ melt with 0-2 wt.% of dissolved alumina at 800 °C

Addition of 2 g of SGA into KF-AlF₃ pure melt (0 wt.% Al₂O₃) led to the decrease in both EMF and resistance during 240 s. Increase of the dissolved alumina concentration to 2 wt.% did not change this duration (according to the OCP). The resistance was oscillating that made the indication of the equilibrium difficult. After 2 minutes of the constant EMF between 240 and 360 s it started rising again with an increasing rate. The reason for this might be the slow transfer of the electrolyte from one half-cell to another and change of the ionic composition.

The introduction of MA alumina into pure melt led to the fast dissolution during 60-70 s (which gives the dissolution rate 0.143-0.167 g·kg⁻¹·s⁻¹) according to the OCP technique results. The resistance of the cell was slightly increased during this time, after which the oscillation began to be observed. The increase in the alumina concentration to 2 wt.% led to the significant increase in the dissolution time up to 390 s. The reason for that can be the chemical reaction-controlled dissolution at low concentrations of dissolved alumina.

α -Alumina

The change in concentration cell EMF after addition of α -Al₂O₃ with the particle size from 1 to 5 μ m in 1.3KF-AlF₃ with different content of aluminium oxide at 800 °C is presented in figure 44.

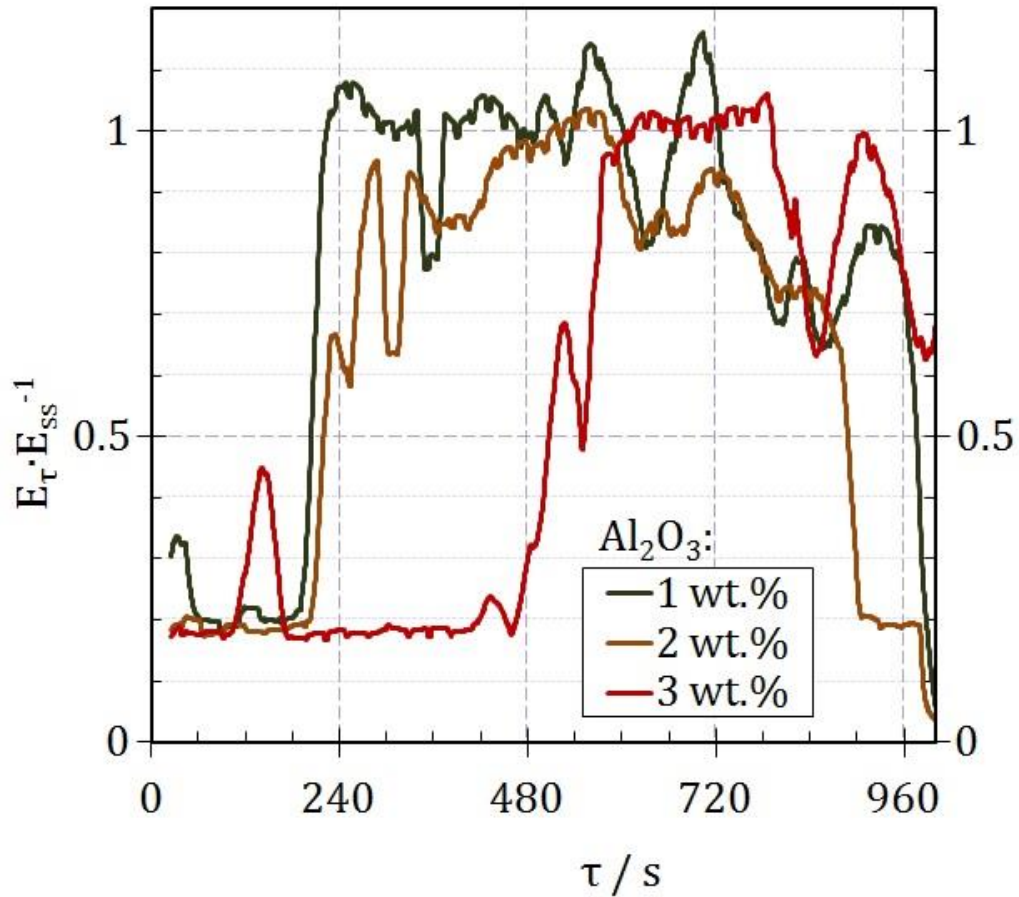


Figure 44. Dependence of normalized EMF of concentration cell vs. time for addition of 2 g of α -Al₂O₃ (1-5 μ m) to 200 g of 1.3KF-AlF₃ melt with 1-3 wt.% of dissolved alumina at 800 °C

The introduction of α -Al₂O₃ had an effect different from ones of the previously studied materials. The curves were not changed significantly during the first 200-500 s. After this period (that depends on the oxide concentration) the drastic increase in EMF was followed. The resistance was oscillating. The α -Al₂O₃ might have had a long latency before the start of dissolution due to the surface inhabitation by the substance with low solubility. If the time of the EMF positive shift can be associated with dissolution time then dissolution rate can be calculated to be 0.167, 0.111 and 0.077 g·kg⁻¹·s⁻¹ at 1, 2 and 3 wt.% of dissolved oxide respectively. All collected data presented in table 13.

Table 13. Dissolution rates of different materials in KF-AlF₃ melt

No	Material	CR	T, °C	C _A , wt.%	W, g/kg · s	method
1	SGA	1.3	850	0	0.080	EIS
2	SGA	1.3	800	0	0.040	EIS
3	SGA	1.3	750	0	0.023	EIS
4	SGA	1.3	750	1	0.031	OCP
5	SGA	1.3	750	2	0.028	OCP
6	SGA	1.3	750	3	0.045	OCP
7	MA	1.3	800	0	0.143	OCP+EIS
8	α -Al ₂ O ₃	1.3	800	1	0.167	OCP
9	α -Al ₂ O ₃	1.3	800	2	0.111	OCP
10	α -Al ₂ O ₃	1.3	800	3	0.077	OCP
11	SGA	1.5	800	1	0.127	LSP*
12	SGA	1.5	800	2	0.111	LSP
13	SGA	1.5	800	3	0.082	LSP

* LSP – linear sweep potentiometry

Dissolution rate depends on the ionic structure of the medium, so the increase in CR leads to the rise of the dissolution rate. This is in a good agreement with previous results for both low-melting and commercial electrolytes [78,107].

Dissolution rate depends on the dissolved alumina concentration in the melt at higher CR and temperature even at low concentrations (0-2 wt.%). Although, at T=750 °C and CR=1.3, the dependence was unclear. It is chance that CR and T highly influence the character of rate-controlling stage. Smaller size particles (both α - and γ -alumina) dissolve much faster than the larger ones. It was previously reported [99, 111] that high content of fine particles (smaller than 45 μ m) reduces the dissolution rate due to the agglomeration mechanism. In current work, alumina with size less than 5 μ m was used. It means that dissolution rate might have a minimum value at certain alumina concentration. All three used methods give comparable results at similar conditions.

The findings state that in terms of dissolution rate the increase in temperature is preferable as well as using alumina with small particles and electrolytes with higher cryolite ratios. Mechanical activation can be considered for further investigations.

4.3. Sedimentation of alumina in KF-AlF₃ melts and suspension

4.3.1. Characterisation of alumina sedimentation

The sedimentation velocity and the suspension stability are considered as highly important parameters of novel electrolytes (suspension melts). The velocity U_{sp} of the single-particle in the liquid is described by the Stokes equation:

$$U_{sp} = \frac{2}{9} \cdot \frac{a_p^2 \cdot g \cdot (\rho_s - \rho_l)}{\eta} \quad (45)$$

where a_p : particle radius, g : gravity acceleration, ρ : density (subindexes s and l denote solid and liquid), η is the dynamic viscosity coefficient.

The collective (or batch) sedimentation velocity U_c is complicated by the $k(\varphi)$ function, which depends on the characteristics of the particles, medium properties and the suspension composition:

$$U_c = \frac{1-\varphi}{k(\varphi)} \quad (46)$$

The Reynolds number (Re) is an important hydrodynamic parameter that indicates Stokesian or non-Stokesian nature of sedimentation. It can be calculated according to the equation:

$$Re = \frac{\rho_l \cdot U_c \cdot d_p}{\eta} = \frac{\rho_l \cdot Q \cdot d_p}{\eta \cdot S} \quad (47)$$

where d_p : particle diameter, Q : volumetric flow rate, S : channel surface area.

4.3.2. Sedimentation behaviour of alumina in KF-AlF₃ melts and suspension

As the density and viscosity of the liquid being the functions of the temperature influence the sedimentation velocity of the alumina particles, it is appropriate to use the EIS technique for the studies. The influence of the temperature on the sedimentation kinetics (indicated by the normalized resistance) of the suspension based on 1.3KF-AlF₃ melt with volume fractions $\varphi=0.1$ is represented in figure 45.

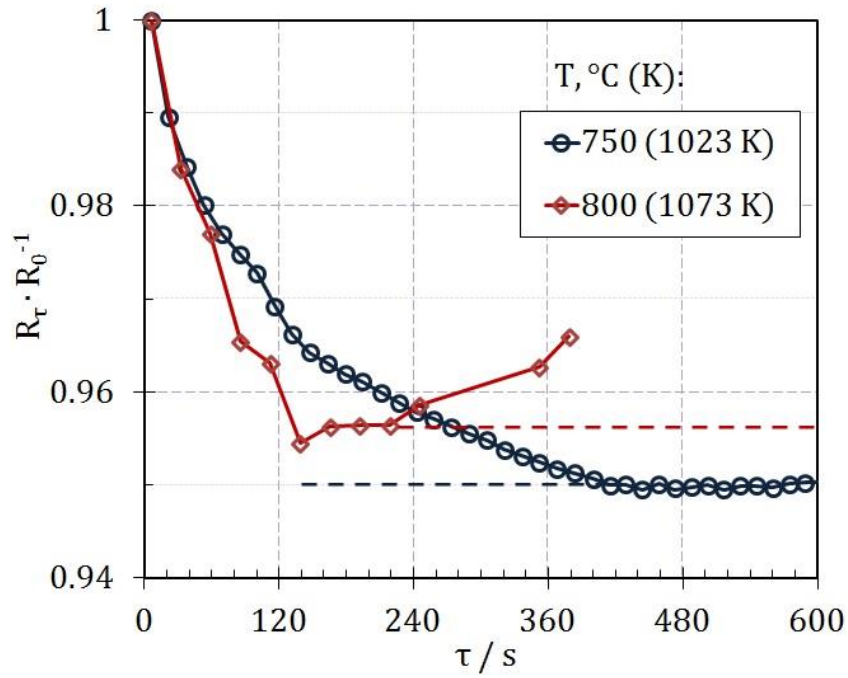


Figure 45. Dependence of normalized resistance vs. time for sedimentation in the 1.3KF-
AlF₃-Al₂O₃(sat) suspension with $\phi = 0.1$ of solid alumina at 750 and 800 °C

It was observed that the resistance of the upper part of slurry in the cell started to decrease immediately after the mixing that evidences the sedimentation of solid particles down the bottom part of the cell. The derivative $\partial R/\partial \tau$ can be associated with the sedimentation velocity [121]:

$$\frac{R_l}{R_s} = (1 - \phi)^{3/2} \quad (48)$$

The initial value of $\partial R/\partial \tau$ remained the same irrespective of the temperatures for the first 60s; however, the further changes in the resistance show the differences in the sedimentation velocities. At both temperatures the sedimentation has two regimes changed after 90 s at 800 °C and 120 s at 750 °C. The quasi-steady-state resistance (and the solid particles local volume fraction in the upper part) was higher at high temperature due to the thermal convection and lower viscosity making the spontaneous mixing of the electrolyte easier.

After reaching the quasi-steady-state the resistance started to increase again in 90-100s which can be due to the uncontrollable fluctuations in the temperature, surface and composition properties of the electrodes and was not considered further in this work. The volumetric flow rates for the first and the second regime were (3.47) and (0.64)·10⁻⁵ m³/s at 800 °C and (1.92) and (0.36)·10⁻⁵ m³/s at 750 °C. The corresponding Reynolds numbers were in the range of 0.006-0.022 that indicates the Stokesian regime of sedimentation.

The dependence between normalized resistance vs. time for the suspension with different aluminium oxides and different ϕ from 0.05 to 0.30 at 800 °C is presented in figure 46 and 47.

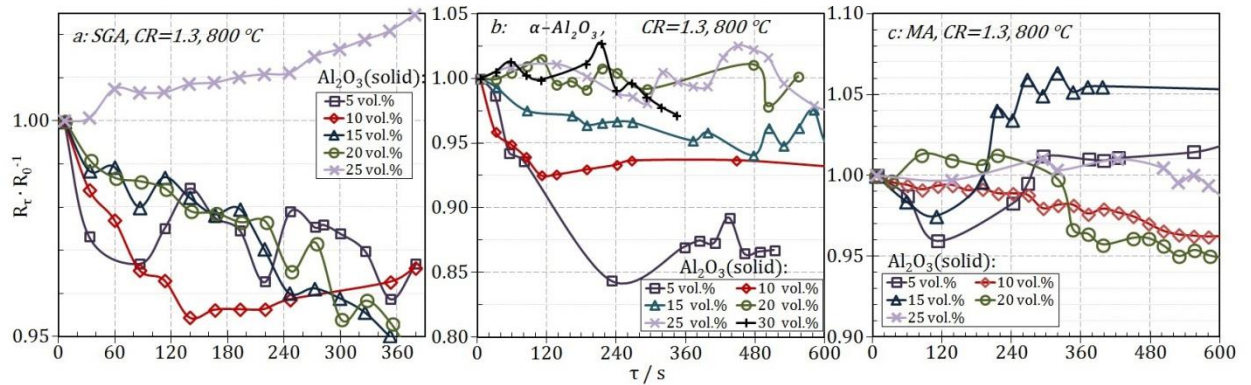


Figure 46. Dependence of normalized resistance vs. time for sedimentation of 1.3KF-AlF₃-Al₂O₃(sat) suspension with SGA (a), alpha aluminium oxide (b) and MA alumina (c) at 800 °C

The initial $\partial R/\partial \tau$ was the function of ϕ . For the materials under study, sedimentation was rapid for low ϕ . Suspensions were stable even before maximum packing fraction ϕ_m , which was previously found to be around 0.32 [112]. Suspensions were stable or quasi-stable at ϕ values of 0.25, 0.20 and 0.10 with SGA, α -Al₂O₃ and MA alumina respectively. The critical effect on the stability is influenced by the particle size and the density of the particles.

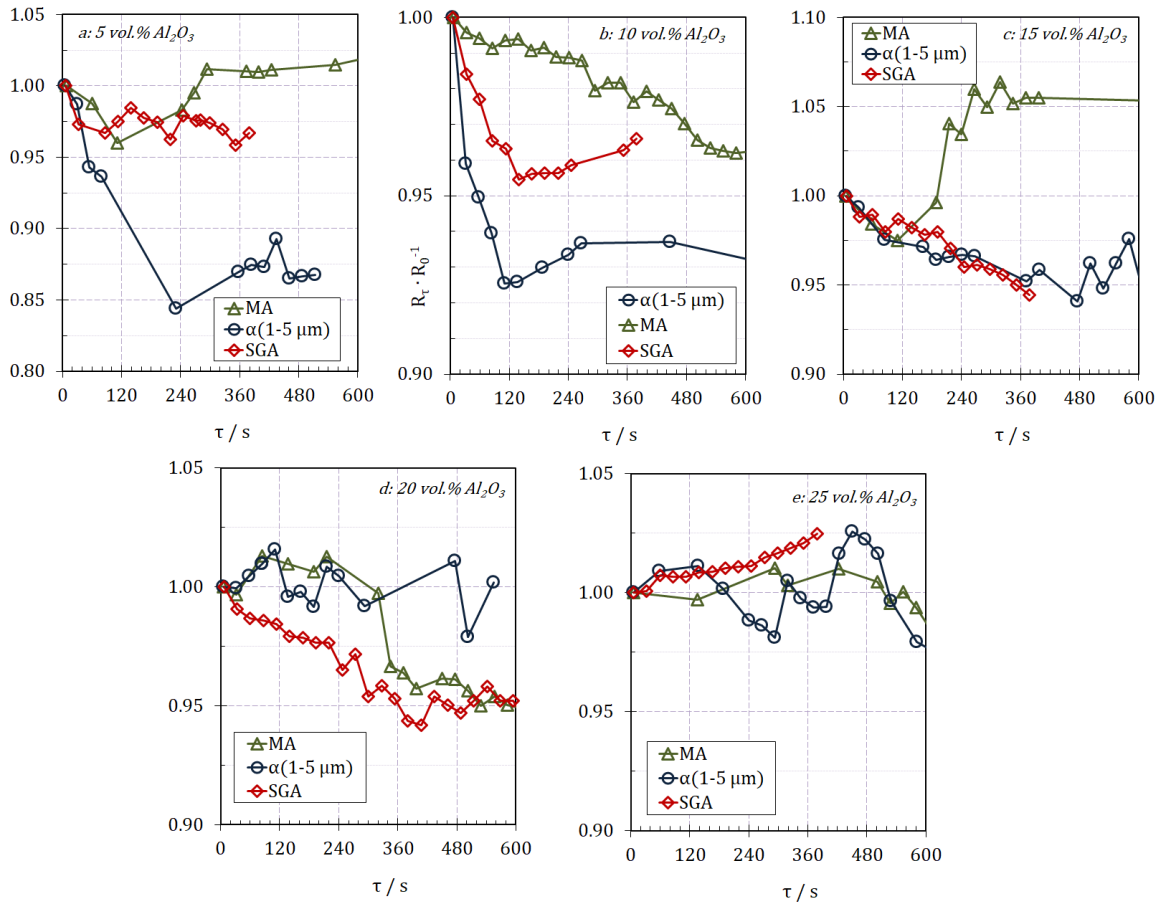


Figure 47. Dependence of normalized resistance vs. time for sedimentation of 1.3KF-AlF₃-Al₂O₃(sat) suspension with a-5, b-10, c-15, d-20 and e-25 vol.% of solid SGAl, α -Al₂O₃ and MA alumina at 800 °C

At low φ the highest sedimentation velocity was observed for α -Al₂O₃ type. The sedimentation velocities were equal for all the studied materials at $\varphi=0.15$. The sedimentation velocities were higher for SGAl due to the larger particle size at $\varphi>0.15$. MA alumina had the best performance in terms of the suspension stability due to the low true density compared to α -Al₂O₃, low particle sizes compared to SGAl and probably surface modification due to the activation. All the data related to the sedimentation behaviour for 3 different types of alumina are presented in table 14.

Table 14. Sedimentation behaviour of different materials

No	$T, ^\circ\text{C}$	Mat.	φ	τ^*, s	R_{ss}/R_0	φ_{up}	$Q \cdot 10^5, \text{m}^3 \cdot \text{s}^{-1}$	$U_c \cdot 10^2, \text{m} \cdot \text{s}^{-1}$	$Re \cdot 10^3$
1	750	SGAl	0.10	1: 130	0.964	0.078	1.92	0.47	3.17
				2: 280	0.950	0.069	0.36	0.09	0.60
2	800	SGAl	0.10	1: 70	0.965	0.078	3.47	0.85	5.96
				2: 90	0.957	0.073	0.64	0.16	1.10
3	800	SGAl	0.05	1: 32	0.973	0.033	6.14	1.51	10.54

				2: 54	0.965	0.027	1.11	0.27	1.91
4	800	SGA	0.15	1: 32	0.988	0.143	2.41	0.59	4.14
				2: 187	0.963	0.128	0.89	0.22	1.52
5	800	SGA	0.20	1: 60	0.983	0.191	1.72	0.42	2.95
				2: 107	0.979	0.189	0.23	0.06	0.40
6	800	SGA	0.25	no	no	no	no	no	no
7	800	α -Al ₂ O ₃	0.05	1: 29	0.943	0.012	14.69	3.61	1.37
				2: 202	0.844	0.000	0.67	0.17	0.06
8	800	α -Al ₂ O ₃	0.10	1: 31	0.959	0.075	9.23	2.27	0.86
				2: 79	0.925	0.052	3.21	0.79	0.30
9	800	α -Al ₂ O ₃	0.15	1: 84	0.975	0.136	1.94	0.48	0.18
				2: 105	0.964	0.129	0.70	0.17	0.07
10	800	α -Al ₂ O ₃	0.20	1: 32	0.999	0.199	0.19	0.05	0.02
11	800	MA	0.05	1: 59	0.987	0.042	1.59	0.39	0.27
12	800	MA	0.10	1: 59	0.994	0.096	0.69	0.17	0.12
13	800	MA	0.15	no	no	no	no	no	no

* duration of the sedimentation stage

The Reynolds number was in the range $(0.02-10.54) \cdot 10^{-3}$ indicating the Stokesian nature of sedimentation for all tested conditions. The sedimentation velocities were in the range $(0.06-3.61) \cdot 10^{-3} \text{ m} \cdot \text{s}^{-1}$ that is several times higher than the values obtained previously [91] for lower temperature (700 °C) and higher particles volume fraction (0.24-0.32) by the pycnometric technique.

The sedimentation velocity and the Reynolds number, highly rely on the temperature, alumina volume fraction and properties. Both U_c and Re increase with T for both regimes of sedimentation due to the decrease in medium viscosity. The sedimentation is always 3-6 times faster during the first regime. The exception was in the case of sedimentation of α -Al₂O₃ suspension with $\varphi=0.05$ where the first regime was 20 times faster compared to the second one.

The highest Reynolds numbers and velocities at $\varphi=0.10$ were demonstrated by the suspension with SGA for both regimes, while the lowest values were found for MA alumina. Moreover, a single regime could be distinguished for the sedimentation of MA alumina at any φ . The sedimentation stability in the case of MA alumina can be reached for the lowest φ between 0.10 and 0.15. This allows us to conclude that in terms of sedimentation stability MA alumina is preferred material for industrial suspension-electrolyte. Lower temperatures are more beneficial for the reduction of sedimentation velocity, however, other limitations related to dissolution rate and electrode processes kinetics appear.

5. Current efficiency test

In this study, the electrolysis was performed using A2 anode and tungsten cathode in a vertical electrode cell. This experiment was performed to determine the current efficiency, purity of the aluminium produced, anodic wear rate and to examine in the structure of the outer layer of the anode after the electrolysis. The obtained results can justify the possibility of the usage of the vertical electrode cell with inert anodes.

5.1. Experimental

Electrolysis test was performed in laboratory two-electrode cell with an amperage of 10 A with 1230 g of 1.4KF-AlF₃-Al₂O_{3(sat)} melt. The cell contains graphite crucible with vertically arranged electrodes. The tungsten plate cathode and 90 Cu-Al wt.% anode were used. 212 g of aluminium was placed at the bottom of the crucible, which would collect the aluminium reduced at the cathode. The operating temperature was 800°C. Al₂O₃ was charged every 30 min for 18 hours and the voltage between cathode and anode was recorded. The SEM-EDX and XRD analysis were conducted to find the content of the elements on the outer layer of the anode and the anode- melt cross-section. Foundry-Master Pro2 (HITACHI) model optical emission spectrometer was used to find the purity of the cathodic aluminium.

5.2. Parameters and conditions

The parameters for the electrolysis were determined based on the stationary parameters and previously obtained results for Cu-Al anode and W cathode working conditions (discussed in chapter 3 and 4):

- The limiting current densities for oxygen evolution increased with an increase in CR and T, anode can perform at the high current density and a rather low overvoltage at CR=1.4 and T=800 °C
- KF-AlF₃-Al₂O_{3(sat)} with CR 1.4 was chosen as the cathode limiting current was almost 0.5 A.cm⁻². Using CR lower than 1.4 would lead to the K reduction on the cathode and passivation of the cathode with KAlF₄ and K₃AlF₆
- High alumina solubility and dissolution rate at CR 1.4 at 800°C

Electrolysis of 1.4KF-AlF₃-Al₂O_{3(sat)} with the 90Cu-Al anode and wetted tungsten cathode was performed under the following parameters:

- current – 10A
- anode current density – 0.25 A.cm⁻²

- cathode current density – 0.25 A.cm⁻²
- anode-cathode distance – 3 cm
- voltage – 3.8–5.8V
- temperature – 800°C
- duration – 18 hours

The photographs related to the cell along with the cathode and anode used for the electrolysis are shown in figure 48. The gas evolution on the anode was observed during electrolysis, believed that the main anode product to be O₂ gas. The anode did not lose its geometric shape after 18-hour electrolysis, although an oxide layer was formed on the active surface of the anode (figure 48 a). The aluminium was deposited as droplets ranging from 0.1 cm to 4 cm (figure 48c). The tungsten cathode was well wetted by aluminium in the process and no anode catastrophic corrosion was observed (figure 48d).

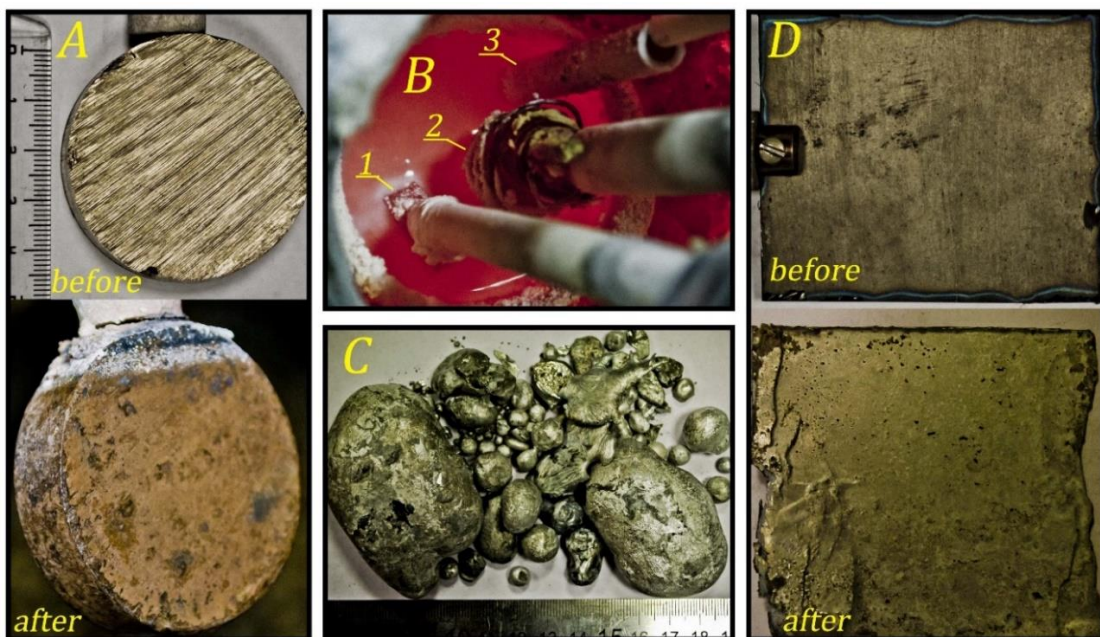


Figure 48. Photos: A. 90Cu- Al anode (before and after the experiment) B. Cell with 1-anode, 2-cathode, 3-thermocouple, C. aluminium produced, D. tungsten cathode (before and after the experiment).

The current efficiency of 84.41 % was obtained. The specific energy consumption for the 4 hours was around 14.5 kWh/ kg Al and 19.8 kWh/ kg Al for the last 6 hours. The linearly increasing voltage between the anode and cathode with the time was observed as shown in figure 49. The anodic overvoltage is related to the formation of an interface (metal fluoride) between the oxide layer and the Cu-Al alloy. The sudden drop of the potential can be seen

(points 2 and 4) which is associated with the depletion of the interface. Oxidation of current leads results in an increase in the resistance. In addition, it was observed that the electrical joints were corroded at the end of the electrolysis test. Better protection of current leads and electrical joints can help to reduce the voltage between the anode and cathode.

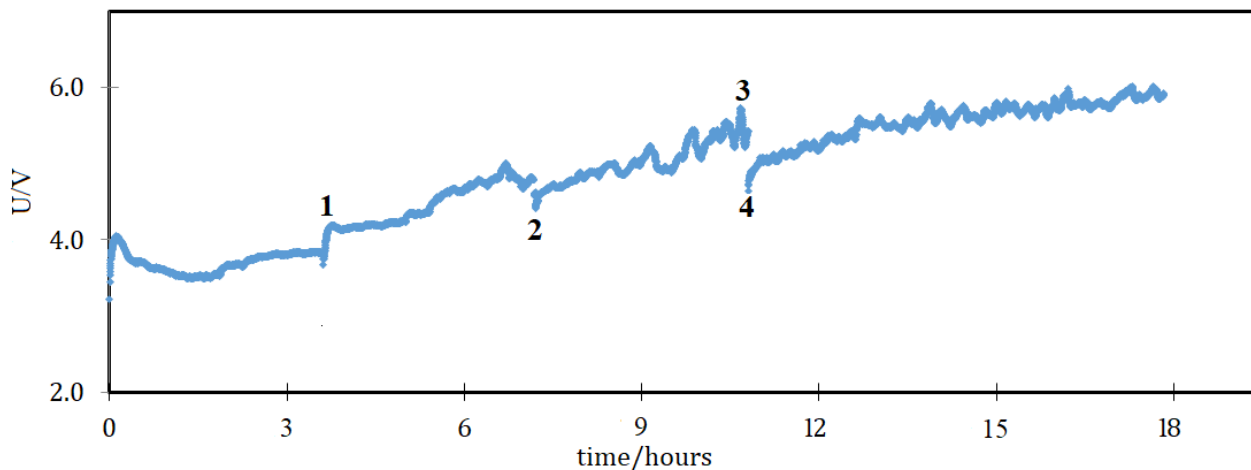


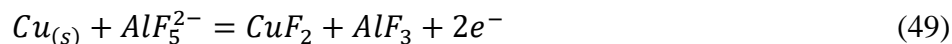
Figure 49. Anode-cathode voltage during the electrolysis for 18 hours with 1.4 KF-AlF₃-Al₂O₃ (sat) melt

5.3. Oxide layer characterization

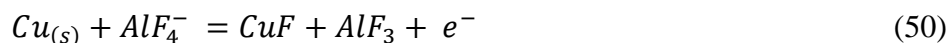
To have a better understanding of the corrosion mechanism of the anode after an interaction with the melt during the electrolysis, the SEM imaging was performed on the anode at the places where the frozen melt was still present. Figure 50 shows the cross-section of the A2 anode after 18-hour electrolysis. With the help of an element-mapping image, it can be seen that Cu, Al and O elements are evenly distributed in the matrix, while the F element is confined to a single area, which is between the oxide scale and the alloy. The thickness of the entire oxide layer is around 140 μm. The outer layer (≈ 20 μm) is CuO-rich (see zone 2) and surrounded by the electrolyte (see zone 1). The inner layer is about 100 μm, resulted from the inward O diffusion.

The oxide layer was composed of CuO, Cu₂O and CuAlO₂ according to the atomic ratio obtained from the single point analysis (see zones 3 and 5). This layer also includes phases, which has high concentrations of Cu and O element (see zone 4). A thin layer (≈ 20 μm) comprised of CuF + AlF₃ and CuF₂ + AlF₃ was observed at the surface between the oxide layer and the Cu-rich alloy (see zone 7). Similar metal fluorides were formed between the oxide layer and the alloy by Jucken et al. [124]. A significant amount of Al metal drops were also present in this particular region; both

EDX element mapping and single-point analysis data can validate this statement. The reactions (49) and (50) may occur in this region:



$$\Delta G_f^o (800\text{ }^\circ\text{C}) = -367.037 \text{ kJ/mole of Al}$$



$$\Delta G_f^o (800\text{ }^\circ\text{C}) = -513.279 \text{ kJ/mole of Al}$$

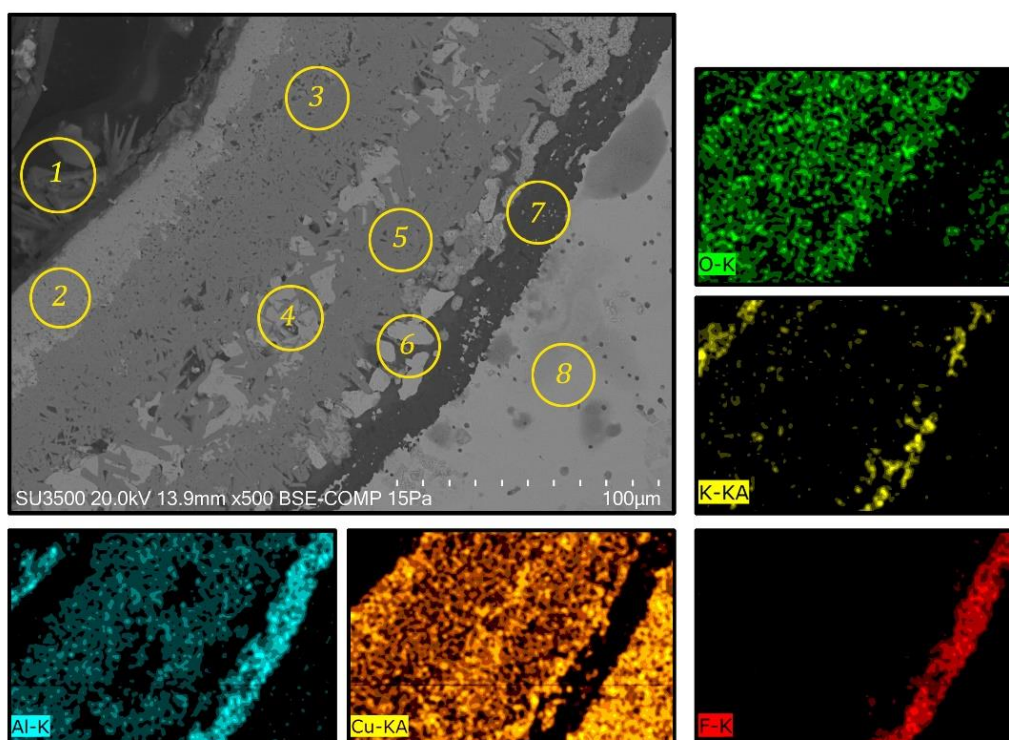


Figure 50. A SEM-EDX image of the cross-section of the 90Cu-Al anode in melt after 18-hour electrolysis.

The SEM imaging on the outer layer of the anode is shown in figure 51. The element-mapping image demonstrates that Cu element is evenly distributed on the outer layer, which establishes that the anode can be electrically conductive even after 18-hour electrolysis. Zone 1 is significantly concentrated with Cu and O elements with 63.28 and 17.10 at.% respectively associated with the presence of Cu element and Cu_2O according to the atomic ratio (see figure 52). It is evident that the Cu present in this area is reduced from the $\text{CuF} + \text{AlF}_3 / \text{CuF}_2 + \text{AlF}_3$ salts, these melts act as an electrolyte between the oxide layer and the Cu-Al alloy. The oxide layer acts as a bipolar electrode where it is a cathode towards the Cu-Al anode and as an anode towards the

W-Al cathode. While zones 2, 3 and 4 are dominated by F and K elements, meaning the presence of the melt and formation of other complex elements like KAlF_4 and K_3AlF_6 and the same complex elements were observed in XRD examination (see figure Ошибка! Источник ссылки не найден.). In zone 5 and 6, the Cu and O elements concentrations are comparatively high, where the Cu_2O and CuO are formed. Table 15 gives a complete understanding of the concentrations of the elements at different places for the SEM-EDX figures 50 and 51.

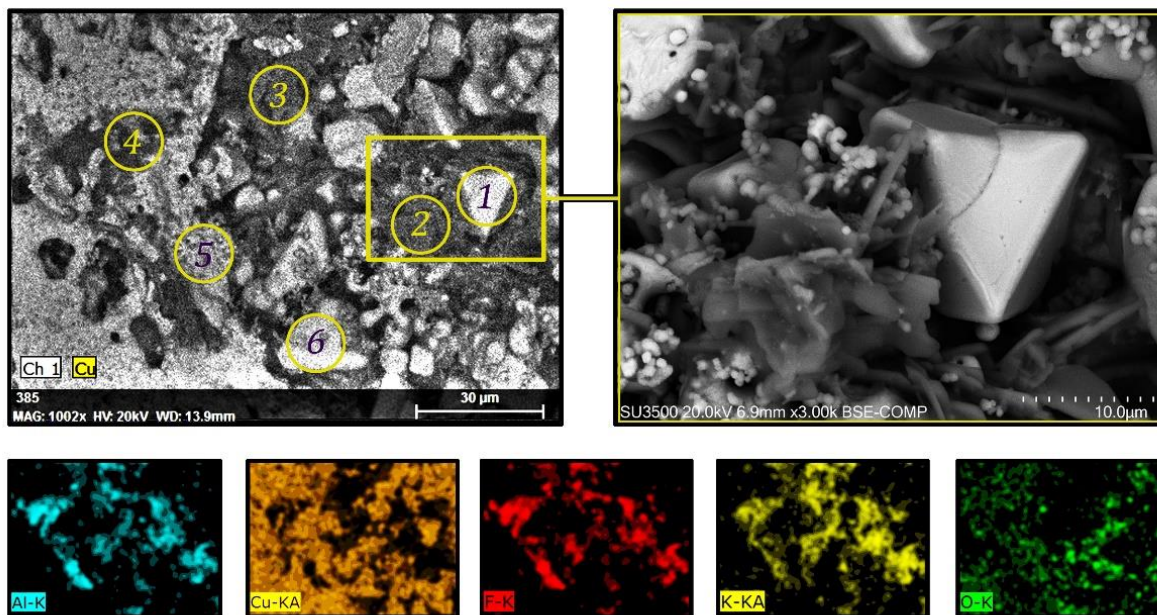


Figure 51. SEM-EDX imaging of the oxide layer on the surface of the 90Cu-Al anode after the electrolysis process

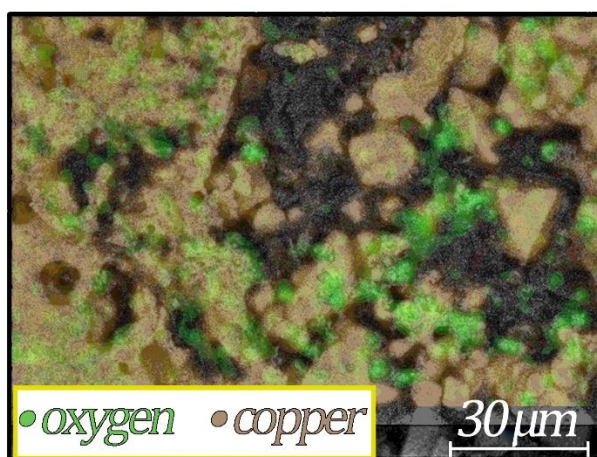


Figure 52. Elemental mapping of oxide layer using SEM-EDX showing the Cu metal dominance.

Table. 15. Content of individual elements (atomic %) in the cross-section of the anode and the melts Figure 50, and the content on the oxide layer on the surface of the anode in Figure 51 using SEM-EDX single point analysis.

Figure 50	Cu	Al	O	F	K	Total
Zone						
1	3.50	14.06	36.27	29.15	27.71	100
2	48.10	4.74	42.98	3.22	0.96	100
3	26.18	21.08	44.47	7.25	1.02	100
4	43.00	19.80	34.92	1.85	0.43	100
5	23.43	25.75	42.76	6.89	1.18	100
6	31.42	21.45	9.17	32.04	5.90	100
7	9.91	19.91	3.74	66.20	0.24	100
8	72.58	13.46	12.30	1.13	0.53	100
Figure 51	Cu	Al	O	F	K	Total
Zone						
1	79.18	4.24	6.75	8.01	1.81	100
2	9.70	17.10	7.93	49.06	16.20	100
3	9.50	18.47	5.81	52.05	14.16	100
4	19.55	19.32	8.30	43.32	9.52	100
5	63.28	5.89	17.10	11.90	1.83	100
6	73.56	5.47	13.10	7.05	0.82	100

The powdered XRD results of the solidified corrosion layer after the 18-hour electrolysis are shown in figure 53. Three oxide phases were detected from the analysis, Cu_2O , CuO and CuAlO_2 . The wt. % of the other phases are: Cu_2O -27.7%, CuO - 30.02%, CuAlO_2 -13.9%, AlF_3 - 3.56%, K_3AlF_6 - 9.51%, KAlF_4 - 12.00% and Cu 4.41%. The CuAl_2O_4 phase which was expected to be present on the anode surface was not detected in the examined sample. The Cu element with 4.41 wt.% observed in the oxide powder is formed electrochemically through the Cu ions discharge in the molten fluoride layer between the oxide scale and the anode itself.

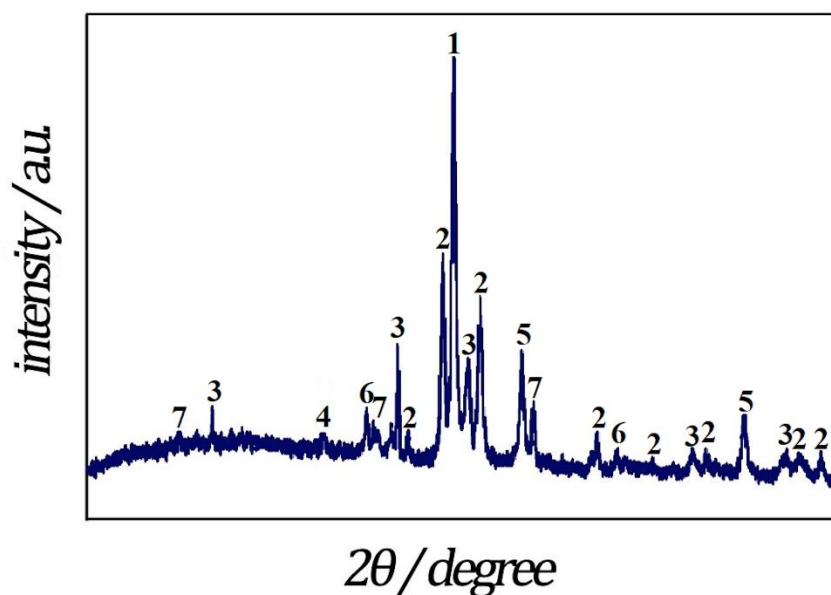


Figure 53. X-ray powder pattern of the reaction layers on the 90Cu-Al anode after 18 hours electrolysis 1-Cu₂O, 2-CuO, 3-CuAlO₂, 4- AlF₃, 5- K₃AlF₆, 6- KAlF₄, 7- Cu

5.4. Aluminium purity

The composition of the aluminium reduced during electrolysis was analysed using optical emission spectrometer to determine the impurity. The results are shown in table 16. The reduced aluminium contains an acceptable level of impurities. Silicon content of about 0.157% in the metal is obtained from the alumina used in the process. This Si impurity from the aluminium can be avoided using smelter grade alumina (SGA) for the reduction process. The Fe content of 0.253% is due to the oxidised current leads and this impurity can be eliminated with proper protection of the current leads and with better anodic geometry. The Cu impurities of 0.0984% in the metal are from the anode. From the obtained electrolysis results, it is clear that the aluminium reduction can be performed using 90Cu-Al anode and wettable cathode with CR 1.4. Higher current efficiencies and metal purity can be attained with minor adjustment using suspension as the electrolyte and can be adapted to industrial scale in the future.

Table. 16. Composition of reduced aluminium in the electrolysis process

Element	Al	Si	Fe	Cu	Mn	Mg	Zn
Average	99.40	0.157	0.253	0.0984	0.0070	0.0109	0.0174
S.D	0.0294	0.0163	0.0167	0.00426	0.00041	0.00193	0.00233
Element	Cr	Ni	Ti	Be	Ca	Li	Pb
Average	0.0040	0.0063	0.0005	< 0.0001	> 0.0050	0.0002	0.0031
S.D	0.000169	0.000262	0	0	0.000282	0	0.0011
Element	Sn	Sr	V	Na	Bi	Zr	B

Average	< 0.0005	0.0001	0.0009	< 0.0001	< 0.0025	0.0125	0.0012
S.D	0	0	0.000124	0	0	0.00054	0.000125
Element	Ga	Cd	Co	Hg	In	P	Sc
Average	0.0141	< 0.0005	< 0.0010	< 0.0010	0.0005	< 0.0030	0.0001
SD	0.000531	0	0	0	0.00047	0	0.00004

Note: optical emission spectrometer was used for the analysis

Annual anode wear rate (WR) can be calculated by using the formula (51)

$$WR = \frac{(m_b \cdot w_b + m_{Al} w_{Al}) \times 365 \times 24}{10^6 \times d_a \times S_a \times t} \quad (51)$$

where m_b : bath mass (g), m_{Al} : produced Al mass (g), w_b : total concentration of Cu contaminants in the bath (ppm), w_{Al} : total concentration of Cu contaminants in the produced Al in (g), d_a : density of the 90Cu-Al alloy (g/cc), S_a : surface area of the anode, t : time in hours.

The WR of the anode is 0.08 cm/year

Summary

In the first stage, the influence of the dispersed phase volume fraction and the anode material on the current-voltage characteristics at stationary and non-stationary polarization, the phase composition of the oxide layer and the features of the formation of the oxide layer on the surface of the material were studied. It was found that an increase in alumina volume fraction leads to an appreciable decrease in apparent limiting current density of the oxygen evolution and the metal oxidation as well. It also leads to the drastic increase in the resistance due to several reasons: accumulation of anode oxidation products and bubbles in the anode layer, growth of oxide layer and structural changes, decrease in the active surface area. The most abundant compounds in all oxide layers are Cu_2O and CuAlO_2 . The 90Cu-10Al anode, the aluminium oxide suspension based on the $\text{KF-AlF}_3\text{-Al}_2\text{O}_3$ system with a volume fraction no more than 0.12 (with $5\ \mu\text{m Al}_2\text{O}_3$) at a temperature of at least $750\ ^\circ\text{C}$ are recommended for further studies.

In the second stage, The influence of dispersed alumina particles content in melts on the current-potential characteristics on Cu-Al anode was studied. The main conclusions:

- The dominant oxide layer on the anode surface in melts ($\varphi=0$) was CuAlO_2 and while using suspension ($\varphi=0.15$) Cu_2O was the dominant one;
- with the increase in the alumina volume fraction, the limiting current densities of metal oxidation and oxygen evolution decrease;
- passivation of the anode at the beginning of the cyclic voltammetry process was seen at $700\ ^\circ\text{C}$ at all CR values (1.2-1.5). The reasons might be the oxide formation or the reduction in the anodic active surface area;
- particle volume fraction (φ) of 0.09 is suggested for further process development;
- anode possesses high oxygen evolution limiting currents at $800\ ^\circ\text{C}$.

In the third stage, the kinetics of the cathode process on W in KF-AlF_3 melts was studied. In the cathode process on W electrode, the aluminium deposition on the cathode surface occurs between -0.125 and $-0.240\ \text{V}$. The peak current densities increases with the decreasing CR's and increasing Al_2O_3 (wt.%). The processes in melts with CR 1.3 and 1.5 are quasi-reversible diffusion-limited and with CR 1.4, it is reversible diffusion-limited.

In the fourth stage, the behaviour of alumina (three types) in KF-AlF_3 melts was studied. The effects of temperature, particle size and phase composition of the dispersed

material and its volume fraction in the suspension on the dissolution kinetics and the sedimentation velocity are studied. It is shown that:

- typical alumina dissolution rates were in the range $0.028\text{-}0.167 \text{ g}\cdot\text{kg}^{-1} \cdot\text{s}^{-1}$, which is close to the values reported previously;
- an increase in the cryolite ratio leads to an increase in the alumina dissolution rate, which is in agreement with previously obtained data;
- the dissolution rate depends on the alumina concentration at higher cryolite ratios and temperatures even at low concentrations in the melt (0-2 wt.%). At $T = 750 \text{ }^\circ\text{C}$ and $\text{CR} = 1.3$, the dependence is not so obvious, which suggests that CR and T can affect the nature of the rate-determining stage;
- mechanically activated particles dissolve faster than SGA, but it is not clear whether this effect is due to the particle size or changes in the crystal lattice;
- all three methods used to study the dissolution rate give comparable results under similar conditions; at the same time, measurements are technically difficult procedures, and the results are difficult to interpret;
- two consecutive sedimentation regimes can be distinguished, namely fast and slow. Sedimentation is usually 3-6 times faster during the first regime;
- the Reynolds number for sedimentation was in the range $(0.02\text{-}10.54)\cdot 10^{-3}$, which indicates the Stokesian nature of sedimentation for all tested conditions and regimes;
- sedimentation velocities were in the range $(0.05\text{-}3.61)\cdot 10^{-2} \text{ m/s}$, which is several times higher than the values obtained previously for $700 \text{ }^\circ\text{C}$ and $\varphi = 0.24\text{-}0.32$;
- the highest velocities and Reynolds numbers at $\varphi=0.10$ were demonstrated by a suspension with SGA for both regimes, while the lowest values were found for MA alumina. Moreover, only one regime (fast) can be distinguished for the sedimentation of MA alumina for any φ . The sedimentation stability of MA alumina can be achieved with the lowest φ between 0.10 and 0.15;

Use of alumina with fine particles and electrolytes with a higher cryolite ratio at $800 \text{ }^\circ\text{C}$, as well as mechanical activation are the preferred solutions for the further development of the suspensions electrolysis technology. Given the limitations imposed by the cathodic process, the preferred cryolite ratio shall be 1.3-1.4. In this case, sedimentation stability can be achieved at $\varphi=0.10\text{...}0.15$.

Finally, based on the obtained results, the electrolysis of $1.4\text{KF}\text{-AlF}_3\text{-Al}_2\text{O}_{3(\text{sat})}$ with Cu-Al anode and W cathode was performed. The purity of the aluminium using optical emission

spectrometer was determined. The XRD, SEM-EDX methods were used to study the phases formed on the anode surface. The main findings are:

- The current efficiency of the electrolysis test was about 84.41%.
- The anode was working without any geometry damage and the wear rate was determined to be 0.08 cm/year.
- The specific energy consumption for the 4 hours was around 14.5 kWh/ kg Al and 19.8 kWh/ kg Al for the last 6 hours
- From the SEM-EDX, it was found that the thickness layer of the oxide scale is about 140 μ m and the metal fluoride layer of 10 μ m was observed in-between the oxide layer and the anode surface. The anode oxide layer acts as a bipolar electrode.
- The cathode aluminium purity was 99.40% and the main impurities are Fe, Si and Cu.

The thesis suggests that the aluminium reduction can be performed using 90Cu-Al anode and wettable tungsten cathode at CR 1.4 and T 800 °C. High purity aluminium can be produced using SGA and properly protected current leads.

References

1. Meyers, R. A., Encyclopedia of Physical Science and Technology: Materials, Chapter: Aluminum, New York: Academic Press, 2004, 495.
2. Primary aluminium production 2018, [accessed on 01/02/2020] available on <http://www.world-aluminium.org/statistics/primary-aluminium-production/#data>
3. Steinfeld, A., Energy, 1997, 22, 311.
4. Balomenos, E., Panias, D., & Paspaliaris, I., Mineral Processing & Extractive Metallurgy Review, 2011, 32(2), 69.
5. C.M. Hall, U.S Patent, US400766, 1889
6. P. Héroult, U.S Patent, US473118, 1892
7. Kvande H. and Haupin W., JOM, 2001, 53, 29.
8. Sadoway D.R., JOM, 2001, 53, 34.
9. Welch B.J., Hyland M.M., and James B.J., JOM, 2001, 53, 13.
10. Welch B.J., Light Metals, TMS, 2009, 971.
11. V. de Nora, “*Inert anodes are knocking at the door of aluminium producers*”, CRU annual meeting, London, 26 June 2001
12. Electrical power used in primary aluminium production. 2020 [accessed on 08/02/2020]; available on: <http://www.world-aluminium.org/statistics>.
13. Keniry J., JOM, 2001, 53, 43.
14. N. Jarrett, Production of aluminium and alumina, A.R. Burkin, Editor. 1987, John Wiley and Sons: New York. p. 188.
15. Du J., Wang B., Liu Y., Yao G., Fang Z., Hu P., Light Metals, 2015, 1193.
16. Augustin C. and Sen U., “*A green anode for aluminium production*”, Incal'98. International Conference on Aluminium, New Delhi, 11-13 Feb. 1998, Vol. 2,173.
17. Hanspeter Alder, U.S Patent, US3960678, 1976
18. Haarberg G.M., “*The interaction between tin oxide and cryolite-alumina melts*”, 9th Int. Symp. on Molten Salts. San Francisco, USA, 22-27 May 1994, Molten salts, Electrochemical Society, Inc (1994), 568.
19. Zaikov Yu.P., “*Ceramic properties of electrodes based on NiO-Li₂O and their solubility in cryolite alumina melts*”, Vill. AI Symposium, 25-27 Sept. 1995, Slovakia, Ziar nad Hronom-Donovaly, 239.
20. Glucina M. and Hyland M., Light Metals, 2005, 523.
21. Nguyen T. and de Nora V., Light Metals, 2006, 385.
22. Simakov D.A., Proc. Non Ferrous Metals, 2012, 363.

23. Helle S., Pedron M., Assouli B., Davis B., Guay D., Roue L., *Corrosion Science*, 2010, 52(10), 3348.
24. Helle S., Tresse M., Guay D., Roue L., *Journal of Electrochemical society*, 2012, 159(4), 62.
25. Divinshi S.V., Herzig C., Hisker F., Filipek R., Danielewski M., *Defects and Diffusion forum*, 2005, 237.
26. Gavrilova E., Goupil G., Davis B., Guay D., Roue L., *Light Metals*, 2015, 1187.
27. Ray S.P. and Rapp R.A., U.S. Patent, US4454015, 1984.
28. Ray S.P. and Rapp R.A., U.S. Patent, US4584172, 1986.
29. Liu J.Y., Li Z.Y., Tao Y.Q., Zhang D., Zhou K.C., *Transaction of Non-ferrous metals in China*, 2011, 21(3), 566.
30. Tian Z.L., Lai Y.Q., Zhang G., Qin Q.W., Wang J.F., Li J., Liu Y., *The Chinese Journal of Nonferrous Metals*, 2003, 06.
31. Feng L., Xie N., Shao W., Zhen L., Ivanov V.V., *Journal of alloys and compounds*, 2014, 610, 214.
32. Antille J., Klinger L., Kaenel R., and de Nora V., *Light Metals* 2006, 391.
33. Rapp R.A., U.S. Patent, US6039862, 2000.
34. Alder H., United States Patent, US3930967, 1976.
35. Haarberg G.M., Kvalheim E., Ratvik A.P., Xiao S.J., Mokkelbost T., *Transaction of Nonferrous Metals Soc. China*, 2010, 20, 2152.
36. Sides P.J. and Prentice G.A., *Electrochim. Acta*, 1988, 33, 1043.
37. Yasinskiy A.S., Vlasov A.A., Polyakov P.V., and Solopov I.V., *Tsvetnye Metally*, 2016(12), 33.
38. Yasinskiy A.S., Polyakov P.V., and Klyuchantsev A.B., *Rus. J. Non-Ferrous Metals*, 2017, 58(2), 109.
39. Sørli M., Hvistendahl J., Øye H.A., *Light metals*, 1993, 921.
40. Sørli M., Øye H.A., *Cathodes in Aluminium Electrolysis*, 3rd edition, Aluminium-Verlag, Dusseldorf, 661 p. (2010).
41. Pawlek R.P., *Light Metals*, 2010, 377.
42. Li Q., Lai Y., Li J., Yang J., Fang J., Chen Z., *Light Metals*, 2005, 789–791.
43. Hengwei Y., Wangxing L., Shilin Q., Ji L., *Light Metals*, 2010, 855.
44. Xue J., Chen X., Gao Y., Zhu J., *Light Metals*, 2010, 383.
45. Lv X., Guan C., Han Z., Chen C., *J. Mol. Liq.*, 2019, <https://doi.org/10.1016/j.molliq.2019.112017> (*In press*).

46. Bao S., Tang K., Kvithyld A., Engh T., Tangstad M., T. Nonferr. Met. Soc. China, 2012, 22(8), 1930.
47. Kontrík M., Šimko F., Galusková D., Nosko M., Bizovská V., Hičák M., Galusek D., Rakhmatullin A., Korenko M., J. Euro. Cer. Soc., 2018, 38(4), 1143.
48. Liao X., Øye H.A., Essent. Read. Light Metals, 2016, 984.
49. Liu D., Yang Zh., Li W., Wang S., and Wang Sh., J. Solid Stat, Electrochem., 2011, 15, 615.
50. Liu D., Yang Zh., and Li W.J., J. Electrochem. Soc., 2010, 157(7), D417.
51. Shtefanyuk Y., Mann V., Pingin V., Vinogradov D., Zaikov Y., Tkacheva O., Nikolaev A., and Suzdaltsev A., Light Metals, 2015, 589.
52. Nikolaev A. Yu., Suzdaltsev A. V., Polyakov P. V., and Zaikova Yu. P., J. Electrochem. Soc., 2017, 164 (8), H5315.
53. Nikolaev A. Yu., Suzdaltsev A. V., and Zaikov Yu. P., J. Electrochem. Soc., 2019, 166 (15), D784.
54. Wei Zh., Peng J., Wang Y., Liu K., Di Yu., and Sun T. (2019) Cathodic process of aluminium deposition in NaF–AlF₃–Al₂O₃ melts with low cryolite ratio, Ionics, 25:1735.
55. Yasinskiy A.S., Padamata S.K., Polyakov P.V., Varyukhin D.Yu., Non–Ferrous Metals, 2019, 2, 15.
56. Kryukovsky V.A., Frolov A.V., Tkacheva O.Yu., Redkin A.A., Zaikov Y.P., Khokhlov V.A., Apisarov A.P., Light Metals, 2006, 409.
57. Xu Q., Ma Y., and Qiu Z., Calphad, 2001, 25(1), 31.
58. Tsirlina G., Antipov E., Glukhov D., Gusev A., Laurinavichute V., Nazmutdinov R., Simakov D., Vassiliev S., Zinkicheva T., Light Metals, 2012, 787.
59. Nazmutdinov R., Zinkicheva T., Vassiliev S., Glukhov D., Tsirlina G., Probst M., Chemical Physics, 2013, 412, 22.
60. Yang J., Li W., Yan H., Liu D., Light Metals, 2013, 689.
61. Apisarov A., Kryukovskii V., Zaikov Y., Red'kin A., Tkacheva O., and Khokhlov V., Russian Journal of Electrochemistry, 2007, 43(8), 870.
62. Vaskova Z., Kontrik M., Mlynarikova J. and Boca M., Metallurgical and Materials Transactions B, 2015, 46B, 485.
63. Beck T.R., “Production of Aluminum with Low Temperature Fluoride Melts”, *Light Metals*, (1994) 89-95.
64. Beck T.R. and Brooks R.J., U.S. Patent, US4592812, 1986.
65. Beck T.R. and Brooks R.J., U.S. Patent, US4865701, 1989.

66. Beck T.R. and Brooks R.J., U.S. Patent, US5006209, 1991.
67. Yasinskiy A.S., Polyakov P.V., Yushkova O.V., Sigov V.A., *Tsvetnye Metally*, 2018, 2, 45 (In Russian).
68. Polyakov P.V., Klyuchantsev A.B., Yasinskiy A.S., and Popov Y.N., *Light metals*, 2016, 283.
69. Thonstad J., Fellner P., Haarberg G.M., Hives J., Kvande H., and Sterten A. (2001) *Aluminium electrolysis. Fundamentals of the Hall–Heroult process*. 3 ed. Dusseldorf, Aluminium–Verlag Marketing & Kommunikation GmbH, 354 p.
70. Danielik V., *Chemical Papers*, 2005, 59(2), 81.
71. Apisarov A., Dedyukhin A., Nikolaeva E., Tinghaev P., Tkacheva O., Redkin A., and Zaikov Y., *TMS Light Metals*, 2010, 395.
72. Robert E., Olsen J.E., Danek V., Tixhon E., Ostvold T., and Gilbert B., *J. Phys. Chem. B*, 1997, 101, 9447.
73. Vaskova Z., Kontrik M., Mlynarikova J., and Boca M., *Met. & Mat. Trans. B*, 2015, 46, 485.
74. Cassayre L., Palau P., Chamelot P., Massot L., *J. Chem. Eng. Data*, 2010, 55,4549.
75. Silny A., Chrenkova M., Danek V., Vasiljev R., Nguyen D.K., and Thonstad J., *J. Chem. Eng. Data*, 2004, 49, 1542.
76. Johnson A.R., *JOM*, 1982, 34(3), 63.
77. Picard G., Seon F., *Electrochimica Acta*, 1982, 27 (3), 401.
78. Sum E., Skyllas-Kazacos M., *Journal Of Applied Electrochemistry*, 1989, 19, 485.
79. Haverkamp R.G., Welch B.J., and Metson J.B., *Electrochemical Society*, 1992, 16, 646.
80. Yang Y., Gao B., Wang Z., Shi Z., Hu X., *JOM*, 2015, 67 (5), 973.
81. Thonstad J., Nordmo F., and Paulsen J. B., *Metallurgical Transactions*, 1972, 3, 403.
82. Frazer E.F., Thonstad J., *Metallurgical And Materials Transactions B*, 2010, 41 (3), 543.
83. Brown C.W., *Light metals*, 2000, 391.
84. Brown C.W., *JOM*, 1998, 50(5), 38.
85. Beck Th.R., *Light Metals*, 1994, 417.
86. Polyakov P.V., Klyuchantsev A.B., Yasinskiy A.S., and Popov Y.N., *Light metals*, 2016, 283.
87. Yasinskiy A.S., Polyakov P.V., and Klyuchantsev A.B., *Rus. J. Non-Ferrous Metals*, 2017, 58(2), 109.
88. Yasinskiy A.S., Vlasov A.A., Polyakov P.V., and Solopov I.V., *Tsvetnye Metally*, 2016(12), 33.

89. Yasinskiy A.S., Padamata S.K., Polyakov P.V., Vinogradov O.O., Tsvetnye Metally, 2019, 9, 42-49 (In Russian).
90. Kan H., Zhang N., Wang X., Journal of Central South University, 2012, 19, 897.
91. Issaeva L.A., Poliakov P.V., B'linov V.A., Mikhalev Iou.G., Buzunov V.I., Light Metals, 1998, 508.
92. Lavoie P., Taylor M.P., and Metson J.B., Metallurgical and Materials Transactions B, 2016, 47(4), 2690.
93. Zhan S., Li M., Zhou J., Yang J., Zhou Y., Applied Thermal Engineering, 2014, 73, 803.
94. Sum E., Skyllas-Kazacos M., Journal Of Applied Electrochemistry, 1989, 19, 485.
95. Yang Y., Gao B., Wang Z., Shi Z., and Hu X., Metallurgical And Materials Transactions B, 2013, 44(5), 1296.
96. Tessier J., Cantin K., and Magnusson D.T., Light Metals, 2018, 515.
97. Haverkamp R.G., and Welsh B.J., 1997, 37, 177.
98. Vasyunina N.V., Vasyunina I.P., Mikhalev Yu.G., and Vinogradov A.M., Russian Journal of Non-Ferrous Metals, 2009, 50 (4), 338.
99. Issaeva L.A., Poliakov P.V., B'linov V.A., Mikhalev Iou.G., Buzunov V.I., Light Metals, 1998, 508.
100. Xiao Y., Tang K., Molten, 2009, 1393.
101. Hou W., Li H., Li M., Zhang B., Wang Y., Gao Y., Applied Mathematical Modelling, 2019, 67, 588.
102. Apisarov A., Influence of the cation composition on the physical and chemical properties of melts for electrolytic production of aluminium. CSc thesis, Institute of High-Temperature Electrochemistry UB RAS, Yekaterinburg [In Russ], 2007, 108.
103. Frolov A., Gusev A., Zaikov Yu., Khramov A., Shurov N., Tkacheva O., Apisarov A., Kovrov V., Light metals, 2007, 571.
104. Isaeva L.A., Braslavskii A.B., Polyakov P.V., Russian journal of non-ferrous metals, 2009, 50, 600.
105. Yushkova O.V. Isaeva L.A., Polyakov P.V., Avvakumov E.G., Tsvetye metally, 2018, 8, 63.
106. Grjotheim K., Kvande H. (1993) Introduction to Aluminium Electrolysis. Understanding the Hall-Heroult Process. 2nd edition. Aluminium-Verlag, Dusseldorf, 212.
107. Apisarov A. (2007) Influence of the cation composition on the physical and chemical properties of melts for electrolytic production of aluminium. Candidate of science thesis, Institute of High-Temperature Electrochemistry UB RAS, Yekaterinburg [In Russ], 108.

108. Frolov A., Gusev A., Zaikov Yu., Khramov A., Shurov N., Tkacheva O., Apisarov A., Kovrov V., *Light metals*, 2007, 571.
109. Zhan S., Li M., Zhou J., Yang J., Zhou Y., *Transactions of nonferrous metals society of China*, 2015, 25, 1648.
110. Yushkova O.V. Isaeva L.A., Polyakov P.V., Avvakumov E.G., *Tsvetye metally*, 2018, 8, 63.
111. Isaeva L.A., Braslavskii A.B., Polyakov P.V., *Russian journal of non-ferrous metals*, 2009, 50, 600.
112. Yasinskiy A.S., Polyakov P.V., Voyshel Y.V., Gilmanshina T.R., Padamata S.K., *Journal of Dispersion Science & Technology*, 2018, 39, 1492.
113. <https://www.zimmerpeacocktech.com/knowledge-base/faq/cyclic-voltammetry/> [accessed on 10/03/2020]
114. https://www.tf.uni-kiel.de/matwis/amat/iss/kap_8/illustr/i8_2_1.html [accessed on 10/03/2020]
115. Padamata S.K., Yasinskiy A.S., Polyakov P.V., *Metallurgical Research and Technology*, 2019, 116(4), 410
116. Yang Z., Gao B., Xu N., Qiu Z., Liu Y., *Journal of Northeastern University (Natural Science)*, 1999, 20(4), 398.
117. Xu J., Shi Z., Gao B., Qiu Z. Dissolution of Alumina in Molten Cryolite. *Journal of Northeastern University (Natural Science)*, 2003, 24(9), 832.
118. Weyand J. D., DeYoung D. H., Ray S. P., Tarcy G. P. and Baker F. W., “Inert anodes for aluminium smelting”, Contract DE-FC07-80CS40158, Final Report, DOE/CS/40158-20, 1986.
119. Strachan D. M., Koski O. H., Morgan L. G., Westerman R. E., Peterson R. D., Richards N. E. and Tabereaux A. T., *Light Metals*, 1990, 395.
120. BURNAKIN V. Fluid dynamics in electrometallurgy of aluminium and magnesium [Gazo-gidrodinamika v electrometallurgii aluminiya i magniya] Doctoral thesis (Engineering), Krasnoyarsk, 1990: 330 (In Russian)
121. Bard A.J., Faulkner L.R. (2001) *Electrochemical methods. Fundamentals and Applications*. Second edition, John Wiley & sons, inc., 833.
122. Fan L., Qiu Z., Grjotheim K., *Journal of Northeastern University*, 1986, 46(1), 97.
123. Zhan S., Li M., Zhou J., Yang J., Zhou Y., *Transactions of nonferrous metals society of China*, 2015, 25, 1648.
124. S. Jucken, B. Tougas, B. Davis, D. Guay, L. Roue, *Metall. Mater. Trans. B.*, 2019, 50(6), 3103.